CORA Cork Open Research Archive
Cartlann Taighde Oscailte Chorcaí

Title	Resonant power conversion topologies for inductive charging of electrical vehicle batteries
Authors	Hayes, John G.
Publication date	1998
Original Citation	Hayes, J. G. 1998. Resonant power conversion topologies for inductive charging of electrical vehicle batteries. PhD Thesis, University College Cork.
Type of publication	Doctoral thesis
Link to publisher's version	http://library.ucc.ie/record=b1284389
Rights	© 1998, John G.Hayes - http://creativecommons.org/licenses/by-nc-nd/3.0/
Download date	2026-10-26 03:36:22
Item downloaded from	https://hdl.handle.net/10468/1542

UCC
University College Cork, Ireland
Coláiste na hOllscoile Corcaigh

RESONANT POWER CONVERSION TOPOLOGIES FOR INDUCTIVE CHARGING OF ELECTRIC VEHICLE BATTERIES

John Gerard Hayes, B.E., M.S.E.E., M.B.A.

A Thesis Presented to the National University of Ireland

for the Degree of

Doctor of Philosophy

July, 1998

Department of Electrical Engineering and Microelectronics

University College Cork,

Ireland.

ABSTRACT

This thesis is concerned with inductive charging of electric vehicle batteries. Rectified power from the 50/60 Hz utility feeds a dc-ac converter which delivers high-frequency ac power to the electric vehicle inductive coupling inlet. The inlet configuration has been defined by the Society of Automotive Engineers in Recommended Practice J-1773.

This thesis studies converter topologies related to the series resonant converter. When coupled to the vehicle inlet, the frequency-controlled series-resonant converter results in a capacitively-filtered series-parallel LCLC (SP-LCLC) resonant converter topology with zero voltage switching and many other desirable features. A novel time-domain transformation analysis, termed Modal Analysis, is developed, using a state variable transformation, to analyze and characterize this multi-resonant fourth-order converter.

Next, Fundamental Mode Approximation (FMA) Analysis, based on a voltage-source model of the load, and its novel extension, Rectifier-Compensated FMA (RCFMA) Analysis, are developed and applied to the SP-LCLC converter. The RCFMA Analysis is a simpler and more intuitive analysis than the Modal Analysis, and provides a relatively accurate closed-form solution for the converter behavior.

Phase control of the SP-LCLC converter is investigated as a control option. FMA and RCFMA Analyses are used for detailed characterization. The analyses identify areas of operation, which are also validated experimentally, where it is advantageous to phase control the converter. A novel hybrid control scheme is proposed which integrates frequency and phase control and achieves reduced operating frequency range and improved partial-load efficiency.

The phase-controlled SP-LCLC converter can also be configured with a parallel load, and is an excellent option for the application. The resulting topology implements soft-switching over the entire load range and has high full-load and partial-load efficiencies. RCFMA Analysis is used to analyze and characterize the new converter topology, and good correlation is shown with experimental results.

Finally, a novel single-stage power-factor-corrected ac-dc converter is introduced, which uses the current-source characteristic of the SP-LCLC topology to provide power factor correction over a wide output power range from zero to full load. This converter exhibits all the advantageous characteristics of its dc-dc counterpart, with a reduced parts count and cost. Simulation and experimental results verify the operation of the new converter.

In memory of my father,

Chas Hayes.

ACKNOWLEDGMENTS

Pursuing a doctorate across two continents was an improbable concept. I wish to express my heartfelt thanks to the many individuals in California and Ireland who helped make this concept a reality.

Firstly, I want to thank my academic advisors at University College, Cork, for their support, advice, guidance, and friendship. The creativity, enthusiasm, expertise, patience, and invaluable suggestions of Dr. Mick Egan and Prof. John Murphy contributed considerably to our work. A special thanks to the students and staff of Power Electronics Technologies and U.C.C. for the camaraderie, and to Prof. Peter Evans for examining my thesis.

The technical and financial support of General Motors Advanced Technology Vehicle is greatly appreciated. I wish to thank John Hall and Dick Bowman for their invaluable support and enthusiasm for our research of the inductive charging technology. Additionally, I wish to acknowledge the contributions of many individuals at GM and elsewhere who have worked to bring the inductive charging technology from concept to production. Among the many contributors are Jon Bereisa, Paul Carosa, Scott Downer, Bailey Fong, Steve Hulsey, Dave Ouwerkerk, Ray Radys, Sergio Ramos, Steve Schulz, Rudy Severns, Herb Tanzer, George Woody, Eddie Yeow and Kwang Yi. Special mention goes to Marco Battigelli, Amy Bueno, Rami Helmy, Tim Lillard, Sam Nakagawa and Dr. Bill Pedler, for their respective contributions to my professional and academic pursuits.

The support of my family and friends has been ever so important to the success of my work. I especially want to thank my mother for her love and invaluable support. Thanks go to Cormac, Finbarr, Peggy, Hailey, Triona, Carl, Florrie, Joe, Kitty, Jerh, and Mary for being there.

Finally, I want to thank my wonderful girlfriend, Mary Herb, for her seemingly endless reserves of love, patience, and understanding during our bicontinental adventures.

TABLE OF CONTENTS

CHAPTER ONE

INTRODUCTION 1

1.1 Overview 1

1.2 Thesis Objectives 2

1.3 Thesis Structure 4

1.4 Inductive Coupling and the Electric Vehicle Application 5

1.4.1 Basic Principles of Inductive Coupling 7

1.4.2 Technology Selection 10

1.4.3 Standardization 11

1.4.4 Inductive Coupling Converter Requirements 13

References 15

CHAPTER TWO

STEADY-STATE OPERATION AND MODAL ANALYSIS OF THE SAE J-1773 INDUCTIVELY COUPLED SERIES RESONANT CONVERTER 17

2.1 Introduction 17

2.2 Converter Description and Operation 18

2.3 Modal Analysis 23

2.3.1 Modal Type A General Solution Equations 24

2.3.2 Modal Type B General Solution Equations 32

2.3.3 Trajectory Solutions 35

2.3.3.1 Trajectory 1 Solution 36

2.3.3.2 Trajectory 2 Solution 40

2.3.3.3 Program Flowchart 42

2.3.4 Converter Characteristics 43

2.4 Experimental Validation 46

2.5 Conclusions 50

References 51

CHAPTER THREE

FUNDAMENTAL MODE APPROXIMATION ANALYSIS OF THE SERIES-PARALLEL LCLC RESONANT CONVERTER WITH CAPACITIVE OUTPUT FILTER AND VOLTAGE-SOURCE LOAD 53

3.1 Introduction 53

3.2 Fundamental Mode Approximation Analysis 55

3.2.1 Basic Circuit Equations 56

3.2.2 RMS and Phase Relationships 56

3.2.3 Circuit Impedances 58

3.2.4 Current-Source Operation 60

3.2.5 Phasor Analysis and Circuit Solution 61

3.2.6 Normalization and Converter Characterization 63

3.2.7 Error Analysis 68

3.3 Rectifier-Compensated Fundamental Mode Approximation Analysis 70

3.3.1 RMS and Phase Angle Relationships 71

3.3.2 Circuit Equations 80

3.3.3 Converter Characterization 82

3.3.4 Error Analysis 84

3.4 Design Example 89

3.5 Conclusions 91

References 92

CHAPTER FOUR

APPLICATION OF PHASE CONTROL TO THE SERIES-PARALLEL LCLC RESONANT CONVERTER WITH CAPACITIVE OUTPUT FILTER AND VOLTAGE-SOURCE LOAD 93

4.1 Introduction 93

4.2 Converter Description and Operation 95

4.3 FMA Analysis of Converter 97

4.3.1 RMS and Phase Relationships 98

4.3.2 Basic Circuit Equations 100

4.4 RCFMA Analysis 104

4.4.1 RMS and Phase Relationships 104
4.4.2 Circuit Equations 105
4.5 Experimental Validation 108
4.6 Conclusions 114
References 115

CHAPTER FIVE
PHASE CONTROL OF THE PARALLEL-LOAD SERIES-PARALLEL RESONANT CONVERTER WITH CAPACITIVE FILTER AND VOLTAGE- SOURCE LOAD 116
5.1 Introduction 116
5.2 Converter Description and Operation 118
5.3 RCFMA Analysis 120
5.3.1 Equivalent Circuit 120
5.3.2 RMS and Phase Relationships 121
5.3.3 Circuit Equations 123
5.3.4 Converter Characterization 125
5.4 Experimental Validation 129
5.5 Comparison of the Frequency- and Phase-controlled Series-parallel Resonant Converters 134
5.6 Conclusions 136
References 137

CHAPTER SIX
OPERATION AND ANALYSIS OF NOVEL SINGLE-STAGE SERIES-PARALLEL RESONANT INDUCTIVE CHARGER 138
6.1 Introduction 138
6.2 Converter Description and Operation 140
6.2.1 Theory of Operation 141
6.2.2 Design Example 144
6.3 PSPICE Validation 149
6.4 Experimental Results 151

6.5 Conclusions 155
References 156

CHAPTER SEVEN
CONCLUSIONS 157

1. CHAPTER ONE

CHAPTER ONE

INTRODUCTION

1.1 OVERVIEW

Inductive coupling is a method of transferring electrical power from the source to the load magnetically rather than by direct ohmic contact. The technology offers advantages of galvanic isolation, safety, connector robustness and durability in power delivery applications where harsh or hazardous environmental conditions may exist [1-7]. Examples of these applications are mining and sub-sea power delivery and electric vehicle (EV) battery charging. General Motors (GM) introduced an EV to the consumer marketplace in December 1996 [1]. The car, known as EV1, featured many new technologies including a radically new design for inductively coupled battery charging. The GM product features all the advantages of inductive coupling and is additionally highly regarded by the general public for its pleasing aesthetics and ease of operation.

In the EV1 system, an off-vehicle high-frequency power converter feeds the cable, coupler, vehicle-charging inlet and battery load. The EV user physically inserts the coupler into the vehicle inlet where the high-frequency power is transformer-coupled, rectified and fed to the battery. The technology is presently being researched and productized at levels ranging from a few kilowatts to hundreds of kilowatts [6,8]. A recommended practice for inductive charging of electric vehicles, SAE J-1773, has been published by the Society of Automotive Engineers (SAE) [9]. The specifications, as outlined in SAE J-1773, for the coupler and vehicle inlet characteristics must be considered in selecting a driving topology. Among the most critical parameters are the frequency range, the low magnetizing inductance, the high leakage inductance and the significant discrete parallel capacitance. The off-vehicle EV1 charge module features a frequency-controlled series-resonant converter. Driving the SAE J-1773 vehicle interface with the series-resonant converter results in a four-element topology with many desirable features: utilization of leakage inductance; buck/boost voltage gain; optimized transformer turns ratio; current-source operation; monotonic power transfer characteristic over a

wide load range; throttling capability down to no-load; high-frequency operation; narrow modulation frequency range; use of zero-voltage-switched MOSFETs with slow integral diodes; high efficiency; inherent short-circuit protection; soft recovery of output rectifiers; secondary *dv/dt* control and current waveshaping for the cable, coupler and vehicle inlet resulting in enhanced electromagnetic compatibility.

1.2 THESIS OBJECTIVES

The first objective of the thesis is to analyze and understand the performance of a frequency-controlled, series-resonant converter driving the vehicle inlet. The combination of the two passive elements of the series-tank impedance and the two significant parallel elements of the inductive coupling vehicle inlet results in a four-element Series-Parallel LCLC (SP-LCLC) converter with a capacitive output filter rather than the more usual inductive output filter. This multi-element, multi-resonant topology had not previously been analyzed in the literature. The thesis develops two novel analytical approaches for the topology. The first analysis is the time-domain Modal Analysis and the second is the frequency-domain Rectifier-Compensated Fundamental Mode Approximation (RCFMA) Analysis.

The four-element SP-LCLC converter with an inductive output filter has previously been analyzed in the time domain [11] and an elegant state variable transformation was developed to decouple and simplify the solution of the fourth-order system. The analysis of the capacitively filtered converter is complicated because of its multi-resonant nature. Thus, a novel time domain analysis is developed for the new topology which extends the state variable transformation analysis [12,13]. This so called Modal Analysis is very accurate and can be used to characterize, design and optimize the inductive charger. However, it is important to note that the time-domain Modal Analysis is mathematically complex, requiring a numerical solution to two simultaneous transcendental equations and it does not yield closed-form expressions for the converter characteristics.

The frequency-domain Fundamental Mode Approximation (FMA) Analysis provides a much simpler and more intuitive approach for the analysis of resonant converters [14]. The initial investigation of the topology using FMA Analysis is insightful and demonstrates key converter characteristics, but its accuracy is poor.

However, a novel extension of the FMA Analysis, termed Rectifier-Compensated FMA Analysis, significantly enhances the accuracy of the predicted performance characteristics of the topology. RCFMA Analysis is a relatively simple but very accurate approach that provides a closed-form solution for the family of multi-element, multi-resonant converters used in the present application, and greatly simplifies the design procedure for the inductive charger.

The second objective of this thesis is to investigate and demonstrate the feasibility of other control and power topology options. The thesis maintains the MOSFET-based series resonant converter as the basic platform from which to explore these concepts. The principal alternative to frequency control is phase control. Phase control of a resonant converter offers the advantages of constant frequency operation resulting in higher efficiency over the load range, improved power component utilization with load, reduced component stresses and costs, and restricted bandwidths for electromagnetic interference (EMI). In the initial study of phase control, the standard inductive charging converter configuration is analyzed. The detailed steady-state analysis of the phase-controlled converter is very complex over the load range, but the relatively simple RCFMA can be extended to cover the phase-controlled converter and yield an insightful and relatively accurate characterization of the converter. The analysis demonstrates that while constant-frequency phase control is general results in a loss of zero voltage switching, a novel hybrid control scheme integrating frequency and phase control may be possible. This new hybrid control displays all of the positive characteristics of frequency control but has reduced frequency range, reduced gate drive requirements and improved light-load efficiency compared to frequency control only.

Further investigation of the phase control option generated a new possibility for constant-frequency operation based on a previously published family of series-parallel resonant converters [16]. The key to achieving soft-switching over the load range for this family is to configure the load in parallel with the outputs of the inverter poles of the charge module. The new converter is again investigated using the RCFMA methodology. The analysis and experimental validation demonstrates the key characteristics, advantages and feasibility of this new SAE J-1773 compatible constant-frequency parallel-load converter.

The proliferation of utility-connected power electronic converters has spurred the demand for products which limit the total harmonic distortion (THD) and maximize the power factor of the currents sourced from the utility. Power-factor-corrected (PFC) utility interfaces are of prime importance in the EV industry because the EV battery charger must minimize line distortion and maximize the real power available from the utility outlet. The EV1 inductive battery charger is a two stage converter featuring a PFC boost pre-regulator and a high-frequency resonant inverter. While two-stage approaches to power factor correction and power regulation are predominant, industry has shown interest in developing single-stage solutions with the desire to reduce the parts count and cost of the conversion stages [17].

The third objective of the thesis is to develop a single-stage inductive charger as a competitive option to the EV1 two-stage converter. The analysis of the frequency-controlled series-parallel resonant converter demonstrates that a key characteristic of the topology is its current-source nature. Thus, the converter is ideally suited to operate as a single-stage converter providing both output power regulation and input current waveshaping. The thesis investigates and demonstrates the feasibility of this novel converter.

1.3 THESIS STRUCTURE

The organization of the thesis is as follows. An overview of inductive charging and the EV application is presented in the second part of this introductory chapter. The background to the modern interest in EV technology is first discussed and the basic principles of inductive coupling are then introduced. Next, the present EV1 charging system is outlined. The significant issues related to the selection of the inductive charging technology are then presented to further explain the applicability of the technology to EVs. Finally, a brief discussion of the SAE J-1773 standard is presented followed by a summary of the desirable characteristics for an inductive charging topology .

In Chapter Two, the converter is analyzed using the time-domain Modal Analysis and the characteristics of the converter are determined. Chapter Three presents the FMA and RCFMA Analyses of the converter. The series- and parallel-

load phase-controlled converters are investigated in Chapters Four and Five, respectively. The single-stage converter is presented in Chapter Six. Each chapter contains a detailed literature review in the introduction and experimental validation is presented where necessary. The summary, conclusions, and suggestions for future work are contained in Chapter Seven.

1.4 Inductive Coupling and the Electric Vehicle Application

General Motors created automotive history by introducing an electric vehicle, EV1, to the Southern California and Arizona markets in December 1996. The EV1 was the first completely new design of a consumer-oriented EV by a major automotive manufacturer in almost a century. At the beginning of the twentieth century, more electric cars were being sold than gasoline-powered cars. However, this was all to change with the introduction of Henry Ford's low-priced Model T in 1908, and the replacement of the engine crank with an electric starter by Cadillac in 1912. The limited range and low speed of the quiet and reliable EV were technology barriers that could not be overcome and resulted in the fading of the EV from the landscape of modern propulsion. As the end of the twentieth century approaches, the renewed interest in EVs is motivated by the environmental concerns of pollution and air quality.

The gasoline-powered automobile has had a more profound effect on the world than any other invention. The technology ushered in a new period of mobility, freedom and societal change for the human race. Yet, these great strides in mechanized propulsion have resulted in new significant problems. Smog and air pollution threaten the health and quality of living of millions of people in urban centers around the world. The increased urbanization of the world's population together with the material desire for individual mechanized propulsion means that the environmental issue of air pollution could be one of the dominant global concerns in the approaching century.

Fig. 1-1. Charging the EV1 in the rain.

The present revival of EV technology at GM began with the “Sunraycer” entry in an Australian solar car race, held in late 1987. The success of the car spurred further interest at GM in designing a consumer electric vehicle and resulted in the building of an EV prototype, known as the “Impact”. The Impact was introduced to the media and the public at the Los Angeles Auto Show in January 1990. GM then surprised the automotive world when it announced at the same event that it would introduce an electric car to the marketplace. While EVs have maintained research status in recent decades, no automotive manufacturer has seriously considered bringing a car to the market in modern times.

Many technical hurdles had to be overcome by GM to bring an EV to the market. Among the more significant issues was battery charging. The Impact featured an on-vehicle conductive charger. However, GM engineers were concerned about the actual and perceived safety for the general public when charging EV batteries, especially at high power levels. As part of the strategy of GM to make the car and the battery charging system more consumer friendly, safer and rugged, a subsidiary of GM, Hughes Electronics (GMHE), developed an inductively coupled battery charger for EV1. Induction coupling in various forms had been considered

as a viable power transfer approach in such areas as EVs, mining and underwater power delivery [2-5]. The task for GMHE was to create a new EV charging system that would meet the expectations of the modern consumer.

1.4.1 Basic Principles of Inductive Coupling

As stated earlier, inductive coupling is a method of transferring electrical power from the source to the load magnetically rather than by direct ohmic contact. The basic principle underlying inductive coupling is that the two halves of the inductive coupling interface are the primary and secondary of a separable two-part transformer. When the charge coupler (i.e. primary) is juxtaposed with the vehicle inlet (i.e. the secondary), power can be transferred magnetically with complete electrical isolation, as with a standard transformer. The coupler and vehicle inlet featured in EV1 are shown in Fig. 1-2. The coupler is attached via the cable to the off-vehicle charging module. When the coupler is inserted into the vehicle inlet, power from the coupler is transformer coupled to the secondary, rectified and fed to the battery by the battery cable. Note that the coupler contains a ferrite block or "puck" at the center of the primary winding to complete the magnetic path when the coupler is inserted into the vehicle inlet.

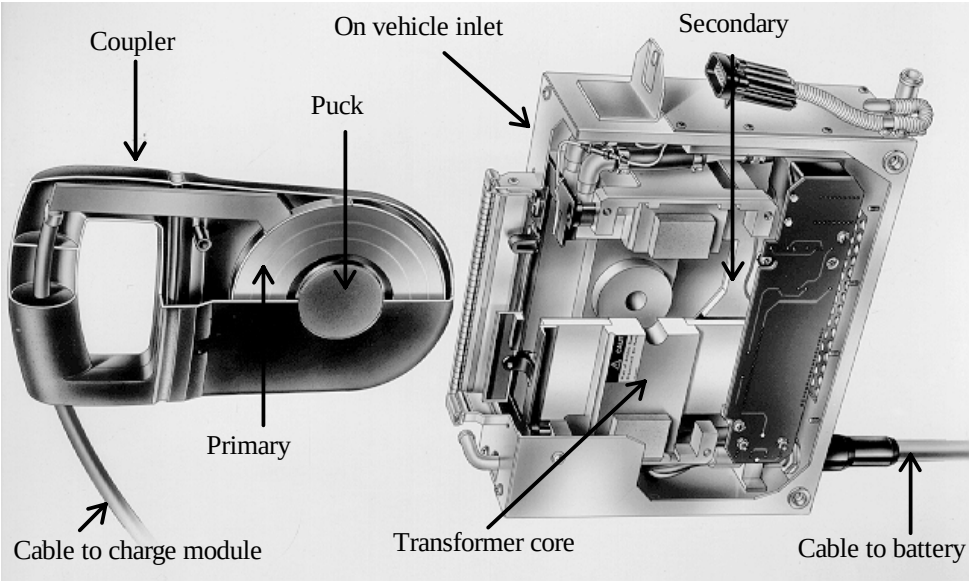

Fig. 1-2. EV1 coupler and vehicle inlet.

The simplified power flow diagram for inductive charging of the EV1 is shown in Fig. 1-3. The charger converts the low frequency utility power to high frequency ac (HFAC) power. The HFAC is transformer-coupled at the vehicle inlet, rectified and supplied to the batteries.

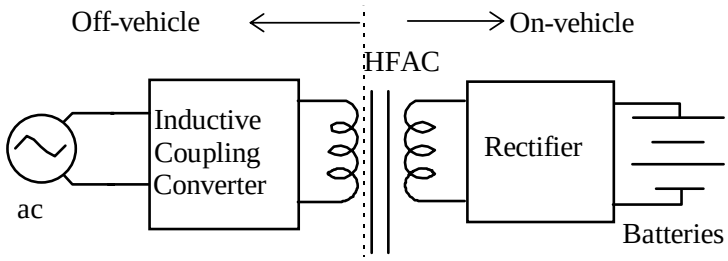

Fig. 1-3. Block diagram of power flow from the utility to the electric vehicle batteries.

The first version of the inductive charger developed at GMHE featured a vehicle inlet with moveable transformer cores and high frequency power supplied by a pulse-width-modulated (PWM) converter. Major problems were encountered with EMI, efficiency, heat distribution, mechanical reliability and electrical sensitivity to the air-gap between the cores. The problems associated with PWM and the moveable core set were overcome by adopting a high frequency resonant power conversion approach and a fixed core set in the vehicle inlet. The large leakage inductance and low magnetizing inductance of the port, major disadvantages for PWM converters, could now be integrated into the operation of the rugged resonant converter. This resonant approach is used in the GM EV1 charger.

A cutaway drawing of the EV1 and the 6.6 kW off-board Standard Charge Module (SCM) is shown in Fig. 1-4. The vehicle inlet is located at the front of the car as indicated. The battery is structured in a T shape, and is located behind the seats and runs through the center of the car. The battery pack has 26 lead-acid 12V batteries for a nominal battery voltage of 312V and an energy storage of 17 kWhr. The actual battery voltage can vary significantly over the charging and propulsion cycle.

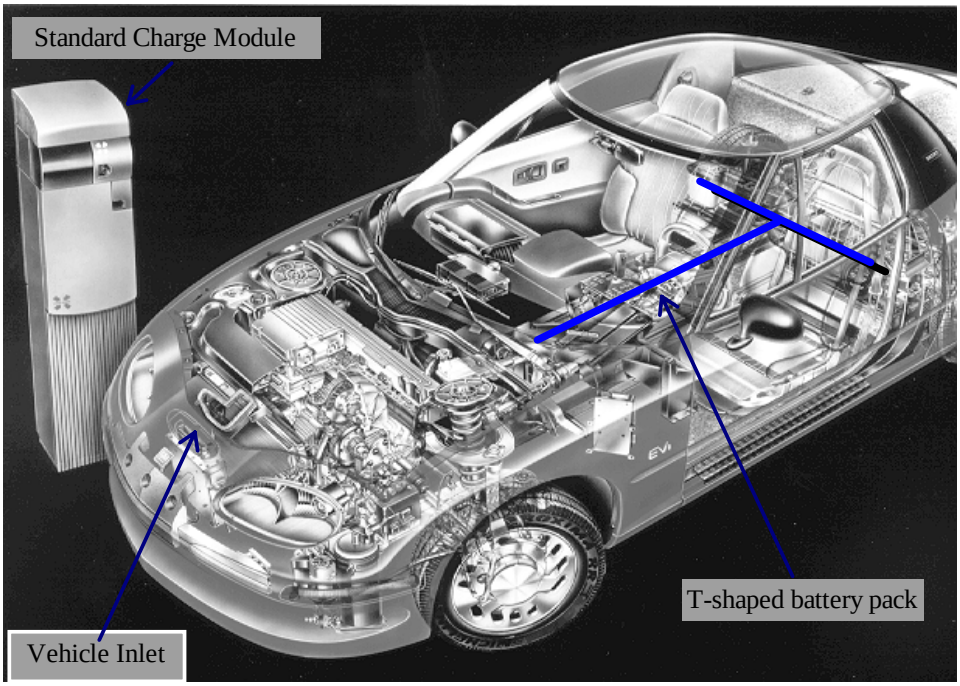

Fig. 1-4. General Motors EV1 electric car and Standard Charge Module.

The simplified system block diagram for EV1 battery charging is shown in Fig. 1-5.

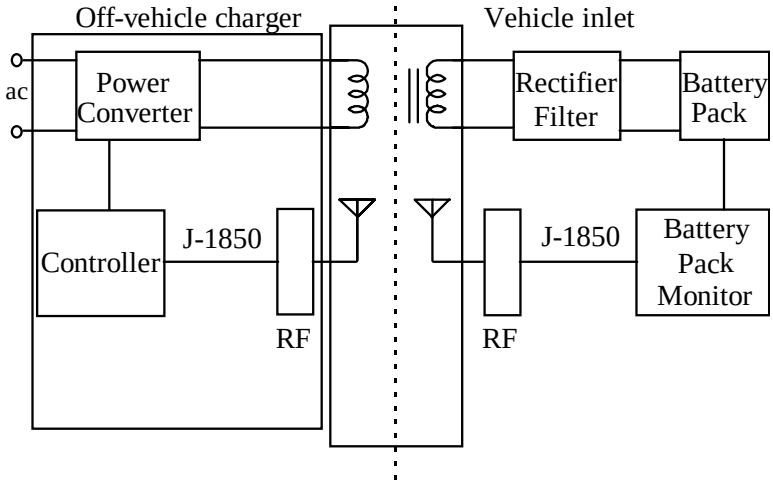

Fig. 1-5. Block diagram of inductive coupling battery charging system.

The control for battery charging operates as follows. A Battery Pack Monitor (BPM) monitors and tracks critical battery information such as voltage, current, state of charge and temperature. The BPM uses this data to generate charging commands for the off-vehicle charger module. The BPM communicates the power command and the state of charge information to the charger using the on-vehicle bi-

directional J-1850 communication bus. The charger module has a RF module for a bi-directional conversion of the RF signal and the J-1850 digital signals. The RF module converts the digital data to a radio frequency signal which is amplitude shift keyed at 915 MHz. The signal is coupled between the antennae which are located in both the coupler and vehicle inlet.

1.4.2 Technology Selection

Many important issues were considered when selecting the inductive charging system. The principal issues governing the choice between the inductive and conductive approaches are safety, reliability, user friendliness and the compatibility of the interface for low and high power operation. These issues are briefly discussed as follows.

Safety: This is the most serious consideration for any automotive manufacturer introducing an EV to the consumer marketplace. The battery charger system must minimize risk of electrical shock and injury to the end user in various operating conditions such as rain or snow. Inductive charging offers significant advantages over conductive charging because the “plug” or coupler and the “receptacle” or vehicle inlet have no exposed power contacts. This feature significantly reduces the risk of shock or injury to the consumer who has direct access to these components.

Reliability: The automotive environment is very harsh. The same performance is expected whether a car is driven in the dry heat of the Arizona desert, the freezing cold of Minnesota or the humid conditions of Florida. The car is exposed to significant shock and vibration in addition to corrosive solvents, salt, water and mud. The charger for the EV must have a long service life with daily operation. The electrical connector must be designed to withstand the 10,000 insertions and withdrawals in these harsh conditions and still remain safe for the consumer for any possible fault condition. The inductive charger with its largely plastic interface is much more suited to these demanding requirements than the conductive charger with its current carrying copper contacts which can be corroded and worn over time.

User friendliness: A consumer product such as a car requires that significant attention be paid to customer expectations, ergonomics and safety. The present way of fueling a vehicle with an internal combustion engine is simple and straight forward. The EV charging must also be simple and should pose minimal challenge

to EV consumers or to young children whom mom or dad may send to “plug in the car”. The inductive coupler design has been engineered to be ergonomic, user friendly and simple to use even at power levels exceeding 100kW. Development work by GMHE at the 120kW power level has shown that the coupler and cable for the high power fast charger can be very light, easy to use and require little insertion force as in the case of the gas nozzle. Greater emphasis has to be placed on the ergonomics of refueling an EV compared to a gasoline-powered car. The basic reason for this is that the EV will probably require daily charging while the gasoline-powered car may only be fueled once a week on average.

High power operation: Earlier work suggested that magnetic and thermal characteristics limited the inductive charging power to about 25kW. However, subsequent research and development pushed the power level to over 100kW. In fact, in 1994 a power conversion of 120kW was achieved using an inlet very similar to that used in the EV1 [6]. One of the main advantages of inductive charging is the universal compatibility. A vehicle inlet can be designed to operate over a wide voltage and frequency range and accept power from off-board charge modules ranging from 1kW to over 100kW. A major difference between a system designed for 6kW versus 100kW is that the copper losses can significantly dominate core losses in the charge vehicle inlet transformer at 100kW. Thus to achieve universal compatibility, the secondary is wound with a low number of turns to minimize vehicle inlet copper losses and the resulting on-vehicle weight and cost [6,7]. The combination of the low number of transformer turns, isolation and spacing requirements and the large airgap in the center-leg of the ferrite core to ensure mechanical fit, results in a relatively low magnetizing inductance. Conversely for the same reasons, the vehicle inlet has a considerable leakage inductance. Fortunately, as previously discussed, a resonant power conversion stage can be designed to work with these parameters.

1.4.3 Standardization

Market acceptance of a new product can be accelerated by creating a product standard. Thus, the Society of Automotive Engineers (SAE) drafted a recommended practice for inductive coupling based upon the GM product. The document is known as SAE J-1773 and was released in January 1995 [9].

According to SAE J-1773, the induction coupler can be represented by the equivalent circuit model shown in Fig. 1-6(a). For analysis, the transformer model can be simplified to include only the topologically significant components, as shown in Fig. 1-6(b). These are the magnetizing inductance, L_P, the parallel capacitor, C_P, and the lumped leakage inductance, L_l, equal to the sum of the primary and secondary leakage inductances, L_{pri} and L_{sec}. Component values and tolerances are shown in Table 1-1.

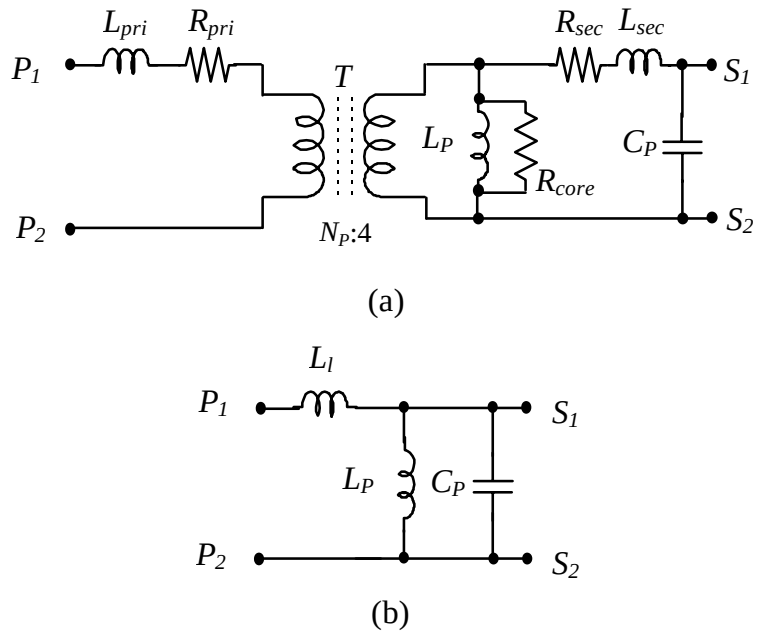

Fig. 1-6. Simplified electrical equivalent circuits of induction coupler.

As noted, the vehicle inlet secondary has 4 turns to minimize the high power conduction losses. The SAE J-1773 standard specifies the low number of turns so that vehicle charging inlets are compatible for different power levels, e.g. a Level 1 (120V, 15A) or Level 2 (230V, 40A) charge module can also charge a Level 3 (25kW to 160kW) vehicle inlet.

Table 1-1

Component values and tolerances as defined in SAE J-1773.

Component	L_P	L_l	C_P
Value	45μH +/-10%	1.6μH +/- 10%	40 nF +/- 5%

The secondary circuit has an additional discrete capacitor, C_P. The basic function of this capacitor is to resonate with the magnetizing inductance L_P. and the series resonant tank components when the inlet is driven with a series resonant converter. This capacitor acts as the fourth element in the series-parallel resonant converter and confers on it many desirable features and characteristics for inductive charging such as enabling soft-switching over the load range for Levels 1 and 2 charging. The capacitor also facilitates reducing the operating frequency range and increasing the converter voltage gain. These issues are discussed in detail in Chapter Three.

1.4.4 Inductive Coupling Converter Requirements

In this thesis it will be shown that a frequency-controlled series resonant converter can be integrated with the SAE J-1773 inlet to create a series-parallel resonant power conversion stage with many characteristics advantageous to inductive coupling. This converter has been the preferred approach for GM in their EV1 charging products [10,13]. The following is a list of the general desired converter characteristics for inductive charging.

1. *High transformer turns ratio.*

The rectified ac utility voltage will be in the 200-400V range with a nominal 220V single-phase input. The exact voltage level depends on whether or not a power-factor-correction stage is used. The dc link voltage will typically be in the 370V to 400V range if a boost-regulated PFC stage is used. The required battery charging voltage will be in the 200-500V range. However, it is to be noted that a unity transformer turns ratio is desirable to minimize primary side voltage and current stresses.

2. *Buck/boost voltage gain.*

Based on Note (1) above, buck/boost operation is required to regulate over the full input and output voltage range.

3. *Current source capability.*

A desirable feature of the converter is that it should operate as a controlled current source. The vehicle inlet has a capacitive rather than inductive output filter stage to reduce on-vehicle cost/weight and additionally desensitize the converter to operating frequency and power level.

4. *Monotonic power transfer curve over a wide load range.*

Wide load operation is required for the likely battery voltage range. The output power should be monotonic with the controlling variable over the load range.

5. *Throttling capability down to no-load.*

All battery technologies require a wide charging current range, varying from a rated power charge to a trickle charge for battery equalization.

6. *High frequency operation.*

High frequency operation is required to minimize vehicle inlet weight and cost.

7. *Full-load operation at minimum frequency for variable frequency control.*

Optimizing transformer operation over the load range suggests that full load operation takes place at low frequencies.

8. *Narrow frequency range.*

The charger should operate over as narrow a frequency range as possible for two principal reasons. Firstly, the passive components can be optimized and secondly, operation into the AM radio band is avoided as electromagnetic emissions in this region must be tightly controlled.

9. *Soft switching.*

Soft switching of the converter stage is required to minimize semiconductor switching loss for high frequency operation. Zero-voltage-switching of a power MOSFET with its slow integral diode can result in efficiency and cost advantages. Similarly, soft recovery of the output rectifiers results in reduced power loss and EMC benefits.

9. *High Efficiency.*

The power transfer must be highly efficient to minimize heat loss and to maximize the overall fuel economy of the electric vehicle charging and driving cycle.

10. *Secondary dv/dt control.*

Relatively slow *dv/dt*'s on the cable and secondary result in reduced high frequency harmonics and less parasitic ringing in the cable and secondary, minimizing electromagnetic emissions.

11. *Continuous-conduction-mode quasi-sinusoidal current waveforms.*

Quasi-sinusoidal current waveforms over the load range result in reduced high frequency-harmonics and less parasitic ringing in the cable and secondary, minimizing electromagnetic emissions.

It will be demonstrated that using the simple frequency-controlled LC series resonant converter to drive the SAE J-1773 compatible vehicle inlet achieves inductive charging, meeting all of the above desired characteristics. The detailed analysis and design of this converter is now described in Chapter Two.

REFERENCES

[1] M. Shnayerson, "The Car That Could, The Inside Story of GM's Revolutionary Electric Vehicle", Random House, 1996.

[2] K. Lashkari, S. Schladover, E. Lechner, "Inductive Power Transfer to an Electric Vehicle," 8th International Electric Vehicle Symposium, Washington D.C., October, 1986.

[3] K. Klontz, D. Divan, D. Novotny, R. Lorenz, "Contactless Power Delivery System for Mining Applications," *IEEE Industrial Applications Society Conf. Rec.*, 1991, pp. 1263-1269.

[4] B. Heeres, D. Divan, D. Novotny, R. Lorenz, "Contactless Underwater Power Delivery," *IEEE Power Electronics Specialists Conf. Rec.*, 1994, pp. 418-423.

[5] N. Kutkut, D.M. Divan and D. W. Novotny, "Inductive Charging Technologies for Electric Vehicles," *IPEC-Yokohama*, 1995, pp. 119-124.

[6] R. Severns, E. Yeow, G. Woody, J. Hall and J. Hayes, "An Ultra-Compact Transformer for a 100W to 120kW Inductive Coupler for Electric Vehicle Battery Charging," *IEEE Applied Power Electronics Conf. Rec.*, 1996, pp. 32-38.

[7] D. Ouwerkerk, “High Powered Charging through a Paddle,” 12th International Electric Vehicle Symposium, Anaheim, California, December, 1994.

[8] K. Klontz, D. Divan, D. Novotny, “An Actively Cooled 120 kW Coaxial Winding Transformer for Fast Charging Electric Vehicles,” *IEEE Trans. Industrial Applications*, Vol. 31, No. 6, Nov/Dec 1995, pp. 1257-1263.

[9] *SAE Electric Vehicle Inductive Coupling Recommended Practice, SAE J-1773*, Society of Automotive Engineers, Draft, Feb. 1, 1995.

[10] N. Kutkut, D.M. Divan, D. W. Novotny and R. Marion, “Design Considerations and Topology Selection for a 120kW IGBT Converter for EV Charging,” *IEEE Power Electronics Specialists Conf. Rec*., 1995, pp. 238-244.

[11] I. Batarseh and C.Q. Lee, “Steady-State Analysis of the Parallel Resonant Converter with LCLC Commutation Network,” *IEEE Trans. Power Electronics*, Vol. 6, No. 3, July 1991, pp. 525-538.

[12] J.G. Hayes, J.T. Hall, M.G. Egan, J.M.D. Murphy, “Full-Bridge, Series-Resonant Converter Supplying the SAE J-1773 Electric Vehicle Inductive Charging Interface,” *IEEE Power Electronics Specialists Conf. Rec*., 1996, pp. 1913-1918.

[13] J.G. Hayes, S.E. Schulz, J.T. Hall, M.G. Egan, J.M.D. Murphy, “Wide Load Range Resonant Converter Supplying the SAE J-1773 Electric Vehicle Inductive Charging Interface” *IEEE Industrial Applications Society Conf. Rec*., 1996, pp. 1065-1071.

[14] R.L. Steigerwald, “A Comparison of Half-Bridge Resonant Converter Topologies,” *IEEE Trans. Power Electronics*, Vol. 3, No. 2, April 1988, pp. 174-182.

[15] J. Hayes, C. Henze, N. Mohan, “Zero-Voltage Switching in a Constant Frequency Digitally Controlled Resonant DC-DC Power Supply,” *IEEE Applied Power Electronics Conf. Rec*., 1988, pp. 360-367.

[16] D. Czarkowski, M.K. Kazimierczuk, “Phase-Controlled Series-Parallel Resonant Converter,” *IEEE Trans. Power Electronics*, Vol. 8, No. 3, July 1993, pp. 309-319.

[17] M. Schutten, R. Steigerwald, M. Kheraluwala, “Characteristics of Load Resonant Converters Operated in a High Power Factor Mode”, *IEEE Applied Power Electronics Conf*., 1991, pp. 5-16.

[18] R. Watson, F. Lee, “A Soft-Switched Full-Bridge Boost Converter Employing an Active-Clamp Circuit,” *IEEE Power Electronics Specialists Conf*., 1996, pp. 1948-1954.

2.

CHAPTER TWO

STEADY-STATE OPERATION AND MODAL ANALYSIS OF THE SAE J-1773 INDUCTIVELY COUPLED SERIES RESONANT CONVERTER

Abstract - The SAE J-1773 recommended practice for electric vehicle battery charging using inductive coupling gives values and tolerances for critical vehicle inlet parameters which must be considered when selecting a coupler driving topology. Driving the vehicle interface with a frequency-controlled series-resonant converter results in a four-element topology with many desirable features. In this chapter, the four-element topology is investigated, analyzed and characterized. A novel time-domain analysis, known as Modal Analysis, is developed to analyze the multi-element multi-resonant converter. In this analysis the swing equations describing each mode of operation are derived and are shown to form a highly coupled fourth-order system. Using a linear state-variable transformation technique the equation sets can be reduced to two decoupled second-order systems and solved to determine the steady-state behavior of the converter. Experimental results show excellent correlation with the analysis.

2.1. INTRODUCTION

In this chapter, the application of the frequency-controlled series-resonant converter feeding the SAE J-1773 vehicle inlet is investigated and analyzed. The combination of the two passive elements of the series converter with the two significant parallel elements of the vehicle inlet results in a four-element Series-Parallel LCLC (SP-LCLC) resonant converter with a capacitive output filter. The large leakage inductance of the vehicle inlet forms part of the inductance of the series tank. The converter is operated in super-resonant mode and has many desirable features for inductive charging.

Accurate analysis of the SP-LCLC topology requires the solution of the time-domain state-variable equations governing the operation of the converter. This approach is termed Modal Analysis and will be used to demonstrate the principal operating characteristics of the converter. The analysis is used as a design tool to

accurately determine any instantaneous, peak, rms or average voltage or current in the topology.

Time-domain based modal analyses have been used extensively to characterize resonant converters. Two-element LC and three-element LLC and LCC-type series and parallel resonant circuits have been comprehensively discussed and analyzed [1-5]. The use of a capacitive output filter has been discussed in [2,3] for the simple LC parallel resonant circuit and in [4,5] for the three-element LCC circuit. Four-element and higher order topologies provide many variations with unique characteristics but have not been treated comprehensively in the literature due to their complexity and number. However, higher order models must be considered if, as discussed in this paper, the magnetizing inductance in the transformer of the inductive coupler is integrated into the study of the LCC converter discussed in [4,5].

The SP-LCLC converter with an inductive output filter has been analyzed in [6,7,10]. Reference [6] developed an elegant state transformation to decouple and simplify the solution of the fourth-order system. This transformation has provided the basis for subsequent analysis of fourth-order converters [8,9,10]. The analysis of the SP-LCLC converter with a capacitive output filter is more complicated because of its multi-resonant nature. Thus, a novel time-domain analysis is developed for the new topology which extends the state transformation technique [12,13]. Modal Analysis is demonstrated to be very accurate and can be used to characterize, design and optimize the inductive charging system.

The basic SP-LCLC converter topology and its operation are described in Section 2.2. Modal Analysis is developed in Section 2.3. The results from an experimental prototype and the analysis are presented and compared in Section 2.4.

2.2. Converter Description and Operation

The isolated full-bridge SP-LCLC converter with capacitive output filter and battery load is shown in Fig. 2-1. The vehicle inlet leakage inductance is significantly less than the series inductance, L_s, and can be included with L_s, thus incorporating the parasitic element in the topology and avoiding the possible detrimental effects which transformer leakage inductance can have in many other topologies.

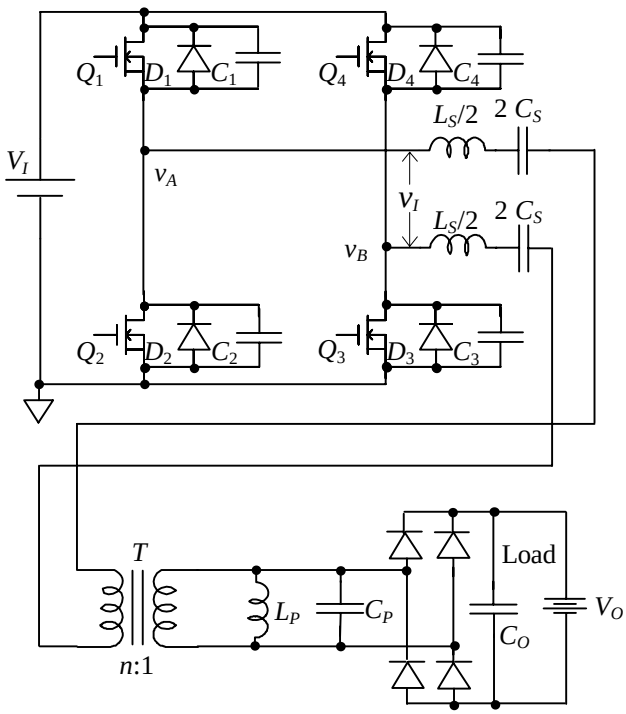

Fig. 2-1. Isolated full-bridge SP-LCLC converter with capacitive output filter and battery load.

The full bridge consists of the controlled switches, Q_1, Q_2, Q_3 and Q_4, their intrinsic anti-parallel diodes, D_1, D_2, D_3 and D_4, and the snubber capacitors, C_1, C_2, C_3 and C_4. Each snubber capacitor consists of the parasitic drain to source capacitance of the MOSFET and any additional discrete capacitance that may be required to achieve zero-voltage switching over the load range. The resonant network consists of two separate resonant tank circuits: the L_s - C_s series tank and the L_P - C_P parallel tank, as defined in the SAE J-1773 standard. Switches Q_1 and Q_3 are gated together in a complementary fashion to switches Q_2 and Q_4. The converter operates in a super-resonant mode and regulates power to the battery by increasing the operating frequency to reduce output current for a given battery voltage.

Several principal state plane trajectories can exist, each of which consists of a sequence of characteristic modes. However, only two are relevant for this four-element topology operating in the super-resonant frequency-controlled mode. The normalized voltage and current waveforms in the resonant tank for these two trajectories, designated Trajectory 1 and Trajectory 2, are shown in Fig. 2-2 and Fig. 2-3, respectively, for operation above the resonant frequency where the switches can transition at zero voltage. Trajectory 2 occurs at higher frequencies and lower load conditions.

The two sets of trajectory waveforms show similar characteristics. The switches experience zero-voltage transitions for both turn-on and turn-off commutations. Both trajectory waveforms show that the switches turn on at zero-voltage as the inverse diode is conducting. At the turn-off instant, t_3, in each case, a significant current flows in the switch allowing the snubber and parasitic switch capacitance to be resonantly charged and discharged resulting in a zero-voltage turn-off. In addition, the diode has a soft turn-off due to the relatively slow *di/dt* of the resonant current and the low voltage drop across the device resulting in significantly reduced reverse recovery loss. Consequently, standard MOSFETs with their slow intrinsic diodes can be used and power loss in the inverter bridge is predominantly due to device on-state conduction losses.

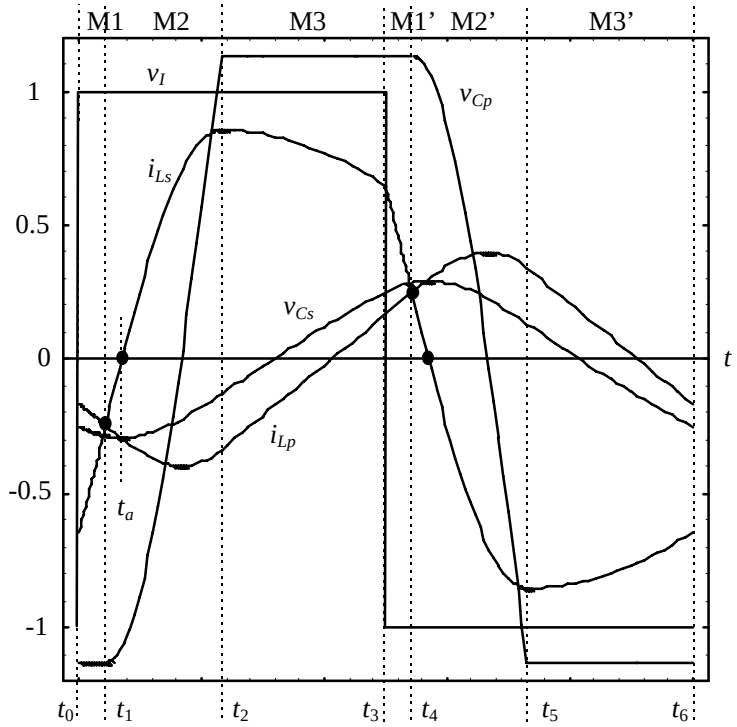

Fig. 2-2. Trajectory 1 normalized waveforms, v_I, v_{Cs}, i_{Ls}, v_{Cp} and i_{Lp}.

The detailed circuit operation for Trajectory 1, as shown in Fig. 2-2, can be understood as follows. Mode M1 occurs from time t_0 to t_1. At time t_0, transistors Q_2 and Q_4 are gated off and Q_1 and Q_3 can be gated on after a short dead time but they do not conduct because their inverse diodes, D_1 and D_3, are conducting. At time t_1, current i_{Ls} equals current i_{Lp} and the output rectifiers commutate with reduced reverse recovery, thus decoupling the capacitively-filtered load from the resonant tank. During Mode M2, from time t_1 to t_2, capacitor C_P is charged from - V_o at t_1 to + V_o at

t_2. At instant t_a during Mode M2, current i_{Ls} changes polarity, commutating diodes D_1 and D_3 with reduced reverse recovery, and transistors Q_1 and Q_3 now begin to conduct. At t_2, the output rectifiers again become forward biased and the parallel tank is once more clamped to the output voltage. Mode M3, from t_2 to t_3, is the main power transfer mode in which the series inductor current is delivered to the load. At t_3, Q_1 and Q_3 are gated off and Q_2 and Q_4 can be gated on after a short dead time, beginning the complementary half-cycle. These devices can be gated off at zero-voltage because the parallel capacitances C_1, C_3 and C_2, C_4 require some time to charge and discharge, respectively, while the current in the MOSFETs is reduced to zero very quickly, thereby minimizing the cross-over power loss. Current i_{Ls} must be sufficient to completely charge C_1 and C_3 and discharge C_2 and C_4 prior to gating on transistors Q_2 and Q_4 to enable a zero-voltage turn-on of Q_2 and Q_4. Modes M1', M2' and M3' are the complementary modes of M1, M2 and M3 respectively. Clearly in this trajectory, the switches turn on at zero voltage and zero current and turn off at zero voltage. The inverse diodes and the output rectifier diodes also turn off with reduced reverse recovery.

Similarly, the detailed circuit operation for Trajectory 2, as shown in Fig 2-3, can be understood as follows. Mode M4 occurs from time t_0 to t_1. At t_0, transistors Q_2 and Q_4 are gated off and Q_1 and Q_3 can be gated on after a short dead time but they do not conduct because their inverse diodes, D_1 and D_3, are conducting. During Mode M4, capacitor C_P is finally discharged and its voltage reaches $-V_o$ at t_1 when the output rectifiers again become forward biased and the parallel tank is once more clamped to the output voltage.

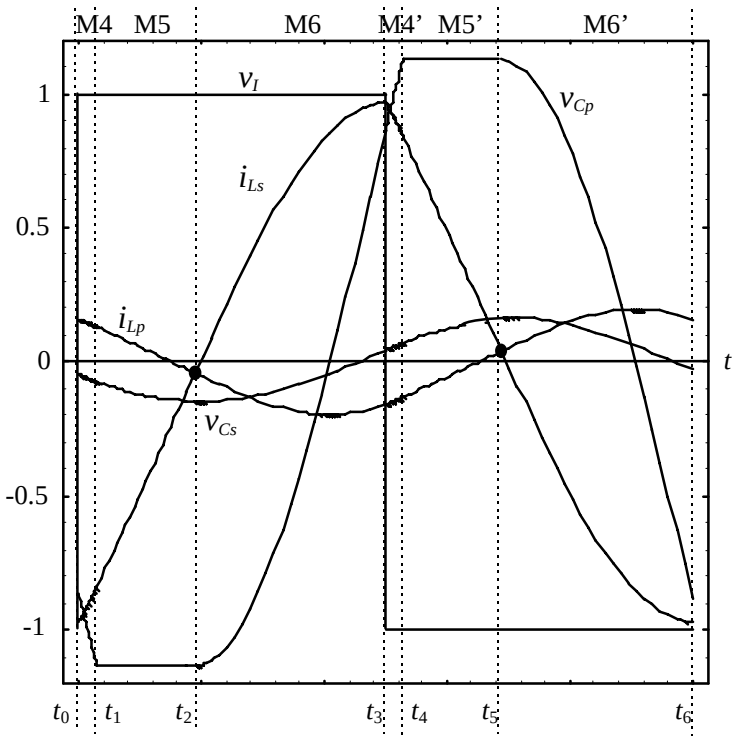

Fig. 2-3. Trajectory 2 normalized waveforms v_I, v_{Cs}, i_{Ls}, v_{Cp} and i_{Lp}.

Mode M5, from t_1 to t_2, is the only power transfer mode for Trajectory 2. At t_2, current i_{Ls} equals current i_{Lp} and the output rectifiers commutate, thus decoupling the capacitively-filtered load from the resonant tank. During Mode M5, from t_2 to t_3, capacitor C_P is charged from $-V_o$. At t_3, prior to v_{Cp} reaching $+V_o$, Q_1 and Q_3 are gated off and Q_2 and Q_4 can be gated on after a short dead time, beginning the complementary half-cycle. These devices can be gated off at zero-voltage as current i_{Ls} is sufficient to completely charge the parallel capacitances, C_1 and C_3, and discharge C_2 and C_4 prior to gating on transistors Q_2 and Q_4. Modes M4', M5' and M6' are the complementary modes of M4, M5 and M6 respectively. As in the previous case, the switches turn on at zero voltage and zero current and turn off at zero voltage. The inverse diodes and output rectifier diodes also turn off with reduced reverse recovery.

2.3. MODAL ANALYSIS

Accurate analysis of the SP-LCLC topology requires the simultaneous solution of the time-domain state-variable equations governing the operation of the converter. This approach is termed Modal Analysis and is used to demonstrate the principal operating characteristics of the converter. The analysis is also used as a design tool to solve for any instantaneous, peak, rms or average voltage or current in the topology.

Two different mode types can be distinguished in the trajectories described above and these are designated Type A and Type B modes. Type A modes are those in which the capacitively-filtered load is decoupled from the resonant elements and the driving voltage V_{E1} is connected to the four passive elements as shown in Fig. 2-4. Voltage sources V_{E1} and V_{E2} are the equivalent voltages across the resonant elements for the particular mode and are defined in detail in Table 2-1.

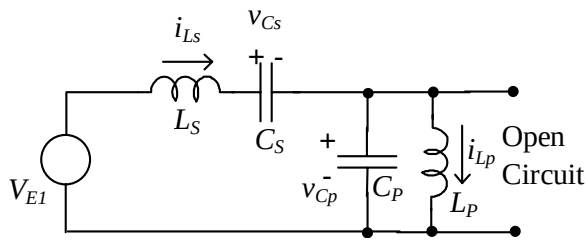

Fig. 2-4. Equivalent circuit for Type A modes.

Type B modes are those in which the load is diode-coupled to the resonant tanks and the voltage across the parallel capacitor C_P is clamped to the output voltage. Consequently, in this mode only the two series elements are resonating since the current in the third element, i_{Lp}, varies linearly as it is in parallel with a constant voltage source. Thus, the equivalent circuit for Type B modes can be reduced to the two simple decoupled sub-circuits shown in Fig. 2-5 (a) and (b).

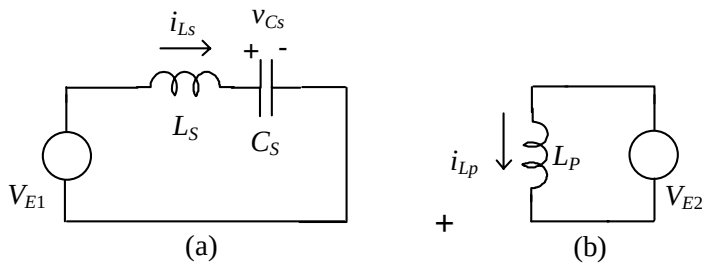

Fig. 2-5. Decoupled sub-circuits (a) and (b) for Type B modes.

Initially, the operation of the generic Type A and B modes is examined and general solution equations are derived. The resultant equations are then assigned initial and final values for each mode in the trajectory and the solution set is reduced to two equations in two unknowns. These equations are in transcendental form and the final solution is obtained numerically.

For this analysis, the following assumptions are made:

(1) The load can be represented by a ripple-free constant dc voltage source.

(2) The switches are gated in a complementary fashion for exactly 50% of the period.

(3) All switches and components are ideal.

2.3.1. Modal Type A General Solution Equations

For Type A modes the load is decoupled from the resonant tanks as shown in Fig. 2-4. The following four state-variable differential equations give the complete mathematical description of the circuit model :

$$\frac{dv_{Cs}(t)}{dt} = \frac{1}{C_S} i_{Ls}(t) \tag{2-1}$$

$$\frac{dv_{Cp}(t)}{dt} = \frac{1}{C_P}\left[i_{Ls}(t) - i_{Lp}(t)\right] \tag{2-2}$$

$$\frac{di_{Ls}(t)}{dt} = \frac{1}{L_S}\left[V_{E1} - v_{Cs}(t) - v_{Cp}(t)\right] \tag{2-3}$$

$$\frac{di_{Lp}(t)}{dt} = \frac{1}{L_P} v_{Cp}(t) \tag{2-4}$$

Equations (2-1) - (2-4) can be expressed in matrix form as

$$\frac{d}{dt}\begin{Bmatrix} v_{Cs}(t) \\ i_{Ls}(t) \\ v_{Cp}(t) \\ i_{Lp}(t) \end{Bmatrix} = \begin{Bmatrix} 0 & \frac{1}{C_S} & 0 & 0 \\ -\frac{1}{L_S} & 0 & -\frac{1}{L_S} & 0 \\ 0 & \frac{1}{C_P} & 0 & -\frac{1}{C_P} \\ 0 & 0 & \frac{1}{L_P} & 0 \end{Bmatrix} \begin{Bmatrix} v_{Cs}(t) \\ i_{Ls}(t) \\ v_{Cp}(t) \\ i_{Lp}(t) \end{Bmatrix} + \begin{Bmatrix} 0 \\ \frac{1}{L_S} \\ 0 \\ 0 \end{Bmatrix} V_{E1} \tag{2-5}$$

or $$\frac{d\mathbf{x}(t)}{dt} = \mathbf{A_A}\mathbf{x}(t) + \mathbf{B_A}U_A \tag{2-6}$$

where $\mathbf{x}(t) = [v_{Cs}(t),\ v_{Cp}(t),\ i_{Ls}(t),\ i_{Lp}(t)]^T$ is the vector representing the four coupled state variables, $\mathbf{A_A}$ is the characteristic matrix, $\mathbf{B_A}$ is the input matrix and U_A is a scalar representing the source voltage.

The above equation represents a fourth order system which can be solved in a systematic way by using the elegant state-variable transformation matrix approach described in [7]. This technique allows the mapping of the four coupled state variables, $\mathbf{x}(t)$, into two mutually decoupled state-variable pairs (v_1,i_1) and (v_2,i_2) defined by the linear transformation T such that

$$\begin{Bmatrix} v_1(t) \\ i_1(t) \\ v_2(t) \\ i_2(t) \end{Bmatrix} = \begin{Bmatrix} 1 & 0 & K_1 & 0 \\ 0 & 1 & 0 & K_3 \\ 1 & 0 & K_2 & 0 \\ 0 & 1 & 0 & K_4 \end{Bmatrix} \begin{Bmatrix} v_{Cs}(t) \\ i_{Ls}(t) \\ v_{Cp}(t) \\ i_{Lp}(t) \end{Bmatrix} \tag{2-7}$$

or $$\mathbf{x_D}(t) = \mathbf{T}\mathbf{x}(t) \tag{2-8}$$

where $\mathbf{x_D}(t) = [v_1,\ i_1\ ,\ v_2,\ i_2]^T$ and K_1, K_2, K_3 and K_4 are real constants.

The inverse of equations (2-7) and (2-8) are

$$\begin{Bmatrix} v_{Cs}(t) \\ i_{Ls}(t) \\ v_{Cp}(t) \\ i_{Lp}(t) \end{Bmatrix} = \begin{Bmatrix} \frac{K_2}{K_2 - K_1} & 0 & -\frac{K_1}{K_2 - K_1} & 0 \\ 0 & \frac{K_4}{K_4 - K_3} & 0 & -\frac{K_3}{K_4 - K_3} \\ -\frac{1}{K_2 - K_1} & 0 & \frac{1}{K_2 - K_1} & 0 \\ 0 & -\frac{1}{K_4 - K_3} & 0 & \frac{1}{K_4 - K_3} \end{Bmatrix} \begin{Bmatrix} v_1(t) \\ i_1(t) \\ v_2(t) \\ i_2(t) \end{Bmatrix} \tag{2-9}$$

or $$\mathbf{x}(t) = \mathbf{T}^{-1}\mathbf{x_D}(t) \tag{2-10}$$

A new differential equation in terms of the decoupled state variables can be defined by combining (2-6), (2-8) and (2-10):

$$\frac{d\mathbf{x_D}(t)}{dt} = \mathbf{T}\mathbf{A_A}\mathbf{T}^{-1}\mathbf{x_D}(t) + \mathbf{T}\mathbf{B_A}U_A \tag{2-11}$$

The next stage of the solution is to solve for **T** in (2-11) so that the state-variable pairs are decoupled. This will result in two mutually independent second-order differential equation sets in terms of the state-variable pairs only. The transformation is illustrated schematically in Fig. 2-6. The pairs L_1, C_1 and L_2, C_2

represent the equivalent passive component values in the second-order resonant circuits and are determined by the transformation **T**. The second-order equations are then easily solved in the normalized form to give a solution set for the decoupled variables. The coupled variables are then substituted for the decoupled variables in the solution set to yield a new generic solution set for the actual fourth-order system.

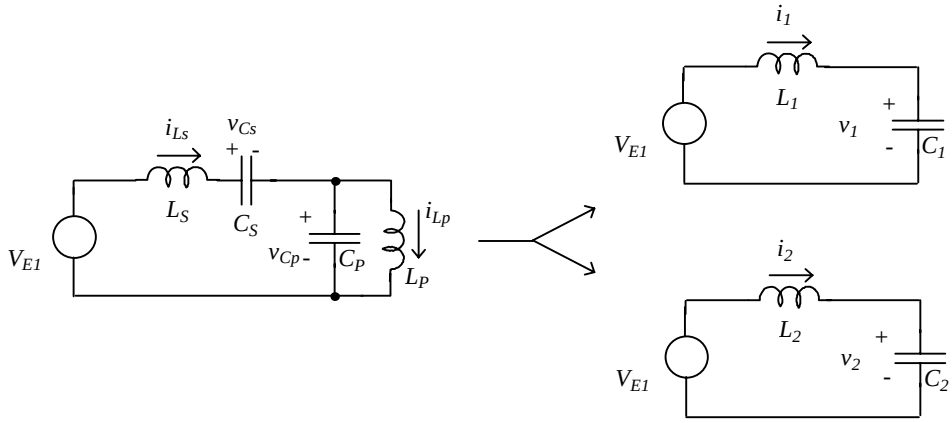

Fig. 2-6. State transformation of fourth-order system to two decoupled second-order systems.

The decoupling process is illustrated as follows for pair (v_1,i_1). The process for pair (v_2,i_2) is identical.

Differentiate v_1 as given by (2-7).

$$\frac{dv_1(t)}{dt} = \frac{dv_{Cs}(t)}{dt} + K_1 \frac{dv_{Cp}(t)}{dt} \tag{2-12}$$

Substitute the coupled currents from (2-1) and (2-2) into the right-hand side of (2-12):

$$\frac{dv_1(t)}{dt} = \frac{1}{C_S} i_{Ls}(t) + \frac{K_1}{C_P}\left[i_{Ls}(t) - i_{Lp}(t)\right] \tag{2-13}$$

Substitute into (2-13) the decoupled currents defined by (2-9) for a new differential equation in terms of decoupled variables only.

$$\frac{dv_1(t)}{dt} = \frac{1}{C_S}\frac{K_4 i_1(t) - K_3 i_2(t)}{K_4 - K_3} + \frac{K_1}{C_P}\left[\frac{K_4 i_1(t) - K_3 i_2(t)}{K_4 - K_3} - \frac{i_2(t) - i_1(t)}{K_4 - K_3}\right] \tag{2-14}$$

Rearrange (2-14) in terms of i_1 and i_2.

$$\frac{dv_1(t)}{dt} = \frac{1}{K_4 - K_3}\left\{\left[\frac{K_4}{C_S} + \frac{K_1(1+K_4)}{C_P}\right] i_1(t) + \left[-\frac{K_3}{C_S} - \frac{K_1(1+K_3)}{C_P}\right] i_2(t)\right\} \tag{2-15}$$

The derivative of v_1 can now be expressed in terms of variable i_1 only, and will be decoupled from i_2 by forcing the co-efficient of i_2 to zero. Hence, solving for K_3 in terms of K_1 yields

$$K_3 = \frac{-K_1}{K_1 + \frac{C_P}{C_S}} \tag{2-16}$$

Substitute (2-16) into (2-15) to give the new differential equation in terms of a single state-variable pair.

$$\frac{dv_1(t)}{dt} = \frac{1}{C_S}\left(1 + \frac{C_S}{C_P}K_1\right)i_1(t) \tag{2-17}$$

A similar procedure can be followed for the differential equation describing $i_1(t)$. Differentiate i_1 as given by (2-7).

$$\frac{di_1(t)}{dt} = \frac{di_{Ls}(t)}{dt} + K_3\frac{di_{Lp}(t)}{dt} \tag{2-18}$$

Substitute the coupled voltages from (2-3) and (2-4) into the right-hand side of (2-18):

$$\frac{di_1(t)}{dt} = \frac{1}{L_S}\left[V_{E1} - v_{Cs}(t) - v_{Cp}(t)\right] + \frac{K_3}{L_P}v_{Cp}(t) \tag{2-19}$$

Substitute in decoupled variables from (2-9).

$$\frac{di_1(t)}{dt} = \frac{1}{L_S}\left[V_{E1} - \frac{K_2 v_1(t) - K_1 v_2(t)}{K_2 - K_1} - \frac{v_2(t) - v_1(t)}{K_2 - K_1}\right] + \frac{K_3}{L_P}\frac{v_2(t) - v_1(t)}{K_2 - K_1} \tag{2-20}$$

Express in terms of v_1 and v_2.

$$\frac{di_1(t)}{dt} = \frac{1}{K_2 - K_1}\left\{\left[-\frac{K_2}{L_S} + \frac{1}{L_S} - \frac{K_3}{L_P}\right]v_1(t) + \left[\frac{K_1}{L_S} - \frac{1}{L_S} + \frac{K_3}{L_P}\right]v_2(t) + \frac{V_{E1}}{L_S}(K_2 - K_1)\right\} \tag{2-21}$$

The derivative of i_1 can now be expressed in terms of variable v_1 only, and will be decoupled from v_2 by forcing the co-efficient of v_2 to zero. Hence, solving for K_3 in terms of K_1 yields

$$K_3 = \frac{L_P}{L_S}(1 - K_1) \tag{2-22}$$

Substituting (2-22) into (2-21) results in a new decoupled differential equation.

$$\frac{di_1(t)}{dt} = \frac{1}{L_S}\left[V_{E1} - v_1(t)\right] \tag{2-23}$$

A similar equation set for (v_2,i_2) can be determined using the same procedure.

$$\frac{dv_2(t)}{dt} = \frac{1}{C_S}\left(1 + \frac{C_S}{C_P}K_2\right)i_2(t) \tag{2-24}$$

$$\frac{di_2(t)}{dt} = \frac{1}{L_S}\left[V_{E1} - v_2(t)\right] \tag{2-25}$$

$$K_4 = \frac{-K_2}{K_1 + \frac{C_P}{C_S}} \tag{2-26}$$

and

$$K_4 = \frac{L_P}{L_S}\left(1 - K_2\right) \tag{2-27}$$

Equations (2-16), (2-22), (2-26) and (2-27) can be solved as quadratic equations to express the K factors in terms of the passive component ratios. The resulting equations are

$$K_1 = \frac{1}{2}\left(1 + \frac{L_S}{L_P} - \frac{C_P}{C_S} + \sqrt{\left(1 + \frac{L_S}{L_P} - \frac{C_P}{C_S}\right)^2 + 4\frac{C_P}{C_S}}\right) \tag{2-28}$$

$$K_2 = \frac{1}{2}\left(1 + \frac{L_S}{L_P} - \frac{C_P}{C_S} - \sqrt{\left(1 + \frac{L_S}{L_P} - \frac{C_P}{C_S}\right)^2 + 4\frac{C_P}{C_S}}\right) \tag{2-29}$$

$$K_3 = \frac{L_P}{L_S}(1 - K_1) \tag{2-30}$$

and

$$K_4 = \frac{L_P}{L_S}(1 - K_2) \tag{2-31}$$

The differential equations (2-17), (2-23), (2-24) and (2-25) describing the decoupled variables for both state-variable pairs can be summarized by

$$\frac{dv_j(t)}{dt} = \frac{1}{C_S}\left(1 + \frac{C_S}{C_P}K_j\right)i_j(t) \tag{2-32}$$

and

$$\frac{di_j(t)}{dt} = \frac{1}{L_S}\left(V_{E1} - v_j(t)\right) \tag{2-33}$$

for j = 1,2.

Differentiating (2-33) and substituting (2-32) into the resulting equation gives

$$\frac{d^2 i_j(t)}{dt^2} = -\omega_{0j}{}^2 i_j(t) \tag{2-34}$$

The radian frequencies, designated by ω_{0j}, correspond to the undamped natural frequencies of the decoupled second-order circuits shown in Fig. 2-6 and are defined by

$$\omega_{0j} = \sqrt{\frac{1}{L_S C_S}\left(1 + \frac{C_S}{C_P} K_j\right)} \tag{2-35}$$

Additionally, there exist characteristic impedances, Z_{01} and Z_{02} defined by

$$Z_{0j} = \sqrt{\frac{L_S}{C_S}\left(1 + \frac{C_S}{C_P} K_j\right)} \tag{2-36}$$

for j = 1, 2.

It can be shown that ω_{0j} is the set of the input resonant frequencies for the four-element topology with an open-circuited output [6]. Similarly, Z_{0j} is the impedance of the series resonant inductor, L_s, at ω_{0j}.

Equation (2-34) represents a second-order differential equation which can be easily solved as follows using Laplace transformations. The Laplace transformation of (2-34) is

$$s^2 I_j(s) - s i_j(t_i) - i'_j(t_i) + \omega_{0j}^2 I_j(s) = 0 \tag{2-37}$$

where $I_j(s)$ is the Laplace transform of $i_j(t)$, and $i_j(t_i)$ and $i'_j(t_i)$ are the values of $i_j(t)$ and its first differential, respectively, at t_i. Rearranging (2-37) as

$$I_j(s) = \frac{s}{s^2 + \omega_{0j}^2} i_j(t_i) + \frac{1}{s^2 + \omega_{0j}^2} i'_j(t_i) \tag{2-38}$$

allows the equation to be easily transformed to the time-domain to yield the solution equation for $i_j(t)$:

$$i_j(t) = i_j(t_i)\cos\omega_{0j}(t - t_i) + \frac{i'_j(t_i)}{\omega_{0j}}\sin\omega_{0j}(t - t_i) \tag{2-39}$$

Substituting (2-33) for $i'_j(t_i)$ gives:

$$i_j(t) = i_j(t_i)\cos\omega_{0j}(t - t_i) - \frac{v_j(t_i) - V_{E1}}{Z_{0j}}\sin\omega_{0j}(t - t_i) \tag{2-40}$$

Combining equations (2-33) and (2-40) gives the complementary voltage solution equation.

$$v_j(t) = Z_{0j} i_j(t_i) \sin\omega_{0j}(t-t_i) + \left[v_j(t_i) - V_{E1}\right]\cos\omega_{0j}(t-t_i) \tag{2-41}$$

Using the above voltage and current equations, the general solution for the decoupled variables can be expressed in matrix form.

$$\begin{Bmatrix} v_1(t) \\ i_1(t) \\ v_2(t) \\ i_2(t) \end{Bmatrix} = \begin{Bmatrix} \cos\omega_{01}(t-t_i) & Z_{01}\sin\omega_{01}(t-t_i) & 0 & 0 \\ -\dfrac{\sin\omega_{01}(t-t_i)}{Z_{01}} & \cos\omega_{01}(t-t_i) & 0 & 0 \\ 0 & 0 & \cos\omega_{02}(t-t_i) & Z_{02}\sin\omega_{02}(t-t_i) \\ 0 & 0 & -\dfrac{\sin\omega_{02}(t-t_i)}{Z_{02}} & \cos\omega_{02}(t-t_i) \end{Bmatrix} \begin{Bmatrix} v_1(t_i) \\ i_1(t_i) \\ v_2(t_i) \\ i_2(t_i) \end{Bmatrix} + \begin{Bmatrix} 1-\cos\omega_{01}(t-t_i) \\ \dfrac{\sin\omega_{01}(t-t_i)}{Z_{01}} \\ 1-\cos\omega_{02}(t-t_i) \\ \dfrac{\sin\omega_{02}(t-t_i)}{Z_{02}} \end{Bmatrix} V_{E1} \tag{2-42}$$

or

$$\mathbf{x_D}(t) = \mathbf{S}_{A1}(t)\mathbf{x}_L(t_i) + \mathbf{S}_{A2}(t)U_A \tag{2-43}$$

The general solution in terms of the coupled variables can be easily derived by substituting (2-7) and (2-8) into (2-42) and (2-43), respectively. The following are the resulting equations in matrix form as

$$\begin{Bmatrix} v_{Cs}(t) + K_1 v_{Cp}(t) \\ i_{Ls}(t) + K_3 i_{Lp}(t) \\ v_{Cs}(t) + K_2 v_{Cp}(t) \\ i_{Ls}(t) + K_4 i_{Lp}(t) \end{Bmatrix} = \begin{Bmatrix} \cos\omega_{01}(t-t_i) & Z_{01}\sin\omega_{01}(t-t_i) & 0 & 0 \\ -\dfrac{\sin\omega_{01}(t-t_i)}{Z_{01}} & \cos\omega_{01}(t-t_i) & 0 & 0 \\ 0 & 0 & \cos\omega_{02}(t-t_i) & Z_{02}\sin\omega_{02}(t-t_i) \\ 0 & 0 & -\dfrac{\sin\omega_{02}(t-t_i)}{Z_{02}} & \cos\omega_{02}(t-t_i) \end{Bmatrix} \times \begin{Bmatrix} v_{Cs}(t_i) + K_1 v_{Cp}(t_i) \\ i_{Ls}(t_i) + K_3 i_{Lp}(t_i) \\ v_{Cs}(t_i) + K_2 v_{Cp}(t_i) \\ i_{Ls}(t_i) + K_4 i_{Lp}(t_i) \end{Bmatrix} + \begin{Bmatrix} 1-\cos\omega_{01}(t-t_i) \\ \dfrac{\sin\omega_{01}(t-t_i)}{Z_{01}} \\ 1-\cos\omega_{02}(t-t_i) \\ \dfrac{\sin\omega_{02}(t-t_i)}{Z_{02}} \end{Bmatrix} V_{E1} \tag{2-44}$$

or

$$\mathbf{T}^{-1}\mathbf{x}(t) = \mathbf{S}_{A1}(t)\mathbf{T}^{-1}\mathbf{x}(t_i) + \mathbf{S}_{A2}(t)U_A \tag{2-45}$$

To aid in the solution we solve for the boundary conditions at the initial and final time instants of the mode, designated t_i and t_f, respectively. Thus, i or f will be appended to the variable subscript to designate the value of variable at the given time instant. For example,

$$v_{Cs}(t_i) = V_{Csi} \tag{2-46}$$

The mode time duration is designated t_γ for Type A modes. In addition a pair of radian angles, γ_1 and γ_2, corresponding to frequencies ω_{01} and ω_{02}, exists for the time interval t_γ and are defined as follows.

$$t_\gamma = \frac{\gamma_1}{\omega_{01}} = \frac{\gamma_2}{\omega_{02}} \tag{2-47}$$

Equation (2-44) can now be written in terms of the boundary values and radian angles.

$$\begin{Bmatrix} V_{Csf} + K_1 V_{Cpf} \\ I_{Lsf} + K_3 I_{Lpf} \\ V_{Csf} + K_2 V_{Cpf} \\ I_{Lsf} + K_4 I_{Lpf} \end{Bmatrix} = \begin{Bmatrix} \cos\gamma_1 & Z_{01}\sin\gamma_1 & 0 & 0 \\ -\dfrac{\sin\gamma_1}{Z_{01}} & \cos\gamma_1 & 0 & 0 \\ 0 & 0 & \cos\gamma_2 & Z_{02}\sin\gamma_2 \\ 0 & 0 & -\dfrac{\sin\gamma_2}{Z_{02}} & \cos\gamma_2 \end{Bmatrix} \begin{Bmatrix} V_{Csi} + K_1 V_{Cpi} \\ I_{Lsi} + K_2 I_{Lpi} \\ V_{Csi} + K_3 V_{Cpi} \\ I_{Lsi} + K_2 I_{Lpi} \end{Bmatrix} + \begin{Bmatrix} 1-\cos\gamma_1 \\ \dfrac{\sin\gamma_1}{Z_{01}} \\ 1-\cos\gamma_2 \\ \dfrac{\sin\gamma_2}{Z_{02}} \end{Bmatrix} V_{E1} \tag{2-48}$$

Equation (2-48) can be solved to express the final value, $\mathbf{x}_f$, in terms of the initial value $\mathbf{x}_i$ and thus provide the overall swing matrix for the coupled variables.

$$\begin{Bmatrix} V_{Csf} \\ I_{Lsf} \\ V_{Cpf} \\ I_{Lpf} \end{Bmatrix} = \begin{Bmatrix} \dfrac{K_2\cos\gamma_1 - K_1\cos\gamma_2}{K_2 - K_1} & \dfrac{K_2 Z_{01}\sin\gamma_1 - K_1 Z_{02}\sin\gamma_2}{K_2 - K_1} & \dfrac{K_1K_2\cos\gamma_1 - K_1K_2\cos\gamma_2}{K_2 - K_1} & \dfrac{K_2K_3Z_{01}\sin\gamma_1 - K_1K_4Z_{02}\sin\gamma_2}{K_2 - K_1} \\ \dfrac{-K_4\sin\gamma_1/(Z_{01}) + K_3\sin\gamma_2/(Z_{02})}{K_4 - K_3} & \dfrac{K_4\cos\gamma_1 - K_3\cos\gamma_2}{K_4 - K_3} & \dfrac{-K_1K_4\sin\gamma_1/(Z_{01}) + K_2K_3\sin\gamma_2/(Z_{02})}{K_4 - K_3} & \dfrac{K_3K_4\cos\gamma_1 - K_3K_4\cos\gamma_2}{K_4 - K_3} \\ \dfrac{\cos\gamma_1 - \cos\gamma_2}{K_1 - K_2} & \dfrac{Z_{01}\sin\gamma_1 - Z_{02}\sin\gamma_2}{K_1 - K_2} & \dfrac{K_1\cos\gamma_1 - K_2\cos\gamma_2}{K_1 - K_2} & \dfrac{K_3Z_{01}\sin\gamma_1 - K_4Z_{02}\sin\gamma_2}{K_1 - K_2} \\ \dfrac{-\sin\gamma_1/(Z_{01}) + \sin\gamma_2/(Z_{02})}{K_3 - K_4} & \dfrac{\cos\gamma_1 - \cos\gamma_2}{K_3 - K_4} & \dfrac{-K_1\sin\gamma_1/(Z_{01}) + K_2\sin\gamma_2/(Z_{02})}{K_4 - K_3} & \dfrac{K_3\cos\gamma_1 - K_4\cos\gamma_2}{K_4 - K_3} \end{Bmatrix} \times$$
$$\begin{Bmatrix} V_{Csi} \\ I_{Lsi} \\ V_{Cpi} \\ I_{Lpi} \end{Bmatrix} + \begin{Bmatrix} -K_2\cos\gamma_1 + K_1\cos\gamma_2 \\ \dfrac{K_4}{Z_{01}}\sin\gamma_1 - \dfrac{K_3}{Z_{02}}\sin\gamma_2 \\ -\cos\gamma_1 + \cos\gamma_2 \\ \dfrac{1}{Z_{01}}\sin\gamma_1 - \dfrac{1}{Z_{02}}\sin\gamma_2 \end{Bmatrix} V_{E1} \tag{2-49}$$

or

$$\mathbf{x}_f = \mathbf{A}_\gamma \mathbf{x}_i + \mathbf{B}_\gamma U_A \tag{2-50}$$

In addition to the forward swing equations (2-49) and (2-50), there exists a complementary set of reverse swing equations. The reverse swing equations are the same as the forward swing equations with the single difference that the swing angle is -γ instead of +γ. The reverse swing equations are thus defined as follows.

$$\begin{Bmatrix} V_{Csf} \\ I_{Lsf} \\ V_{Cpf} \\ I_{Lpf} \end{Bmatrix} = \begin{Bmatrix} \dfrac{K_2\cos\gamma_1 - K_1\cos\gamma_2}{K_2 - K_1} & \dfrac{-K_2 Z_{01}\sin\gamma_1 + K_1 Z_{02}\sin\gamma_2}{K_2 - K_1} & \dfrac{K_1K_2\cos\gamma_1 - K_1K_2\cos\gamma_2}{K_2 - K_1} & \dfrac{-K_2K_3Z_{01}\sin\gamma_1 + K_1K_4Z_{02}\sin\gamma_2}{K_2 - K_1} \\ \dfrac{K_4\sin\gamma_1/(Z_{01}) - K_3\sin\gamma_2/(Z_{02})}{K_4 - K_3} & \dfrac{K_4\cos\gamma_1 - K_3\cos\gamma_2}{K_4 - K_3} & \dfrac{K_1K_4\sin\gamma_1/(Z_{01}) - K_2K_3\sin\gamma_2/(Z_{02})}{K_4 - K_3} & \dfrac{K_3K_4\cos\gamma_1 - K_3K_4\cos\gamma_2}{K_4 - K_3} \\ \dfrac{\cos\gamma_1 - \cos\gamma_2}{K_1 - K_2} & \dfrac{-Z_{01}\sin\gamma_1 + Z_{02}\sin\gamma_2}{K_1 - K_2} & \dfrac{K_1\cos\gamma_1 - K_2\cos\gamma_2}{K_1 - K_2} & \dfrac{-K_3Z_{01}\sin\gamma_1 + K_4Z_{02}\sin\gamma_2}{K_1 - K_2} \\ \dfrac{\sin\gamma_1/(Z_{01}) - \sin\gamma_2/(Z_{02})}{K_3 - K_4} & \dfrac{\cos\gamma_1 - \cos\gamma_2}{K_3 - K_4} & \dfrac{K_1\sin\gamma_1/(Z_{01}) - K_2\sin\gamma_2/(Z_{02})}{K_4 - K_3} & \dfrac{K_3\cos\gamma_1 - K_4\cos\gamma_2}{K_4 - K_3} \end{Bmatrix} \times$$
$$\begin{Bmatrix} V_{Csi} \\ I_{Lsi} \\ V_{Cpi} \\ I_{Lpi} \end{Bmatrix} + \begin{Bmatrix} -K_2\cos\gamma_1 + K_1\cos\gamma_2 \\ -\dfrac{K_4}{Z_{01}}\sin\gamma_1 + \dfrac{K_3}{Z_{02}}\sin\gamma_2 \\ -\cos\gamma_1 + \cos\gamma_2 \\ -\dfrac{1}{Z_{01}}\sin\gamma_1 + \dfrac{1}{Z_{02}}\sin\gamma_2 \end{Bmatrix} V_{E1} \tag{2-51}$$

or $$\mathbf{x}_i = \mathbf{A}_{-\gamma}\mathbf{x}_f + \mathbf{B}_{-\gamma}U_A \tag{2-52}$$

The newly-derived forward and reverse swing equations define the solution equation sets for Type A modes. Thus, when any set of boundary values of the variables are known, the intermediate values can be determined for any time instant within the mode. In the next section, a similar equation set is derived for Type B modes.

2.3.2. Modal Type B General Solution Equations

Type B modes differ from Type A modes as only three passive elements have to be considered, since v_{Cp} is clamped to the output voltage. The following differential equations give the mathematical description of the circuit model for the Type B mode sub-circuit shown in Fig. 2-5(a).

$$\frac{dv_{Cs}(t)}{dt} = \frac{1}{C_S} i_{Ls}(t) \tag{2-53}$$

$$\frac{di_{Ls}(t)}{dt} = \frac{1}{L_S}\left[V_{E1} - v_{Cs}(t)\right] \tag{2-54}$$

The equation for the output stage for the Type B mode sub-circuit shown in Fig. 2-5(b) is

$$\frac{di_{Lp}(t)}{dt} = \frac{1}{L_P} V_{E2} \tag{2-55}$$

Equations (2-53), (2-54) and (2-55) can be written in matrix form as

$$\frac{d}{dt}\begin{Bmatrix} v_{Cs}(t) \\ i_{Ls}(t) \\ v_{Cp}(t) \\ i_{Lp}(t) \end{Bmatrix} = \begin{Bmatrix} 0 & \frac{1}{C_S} & 0 & 0 \\ -\frac{1}{L_S} & 0 & 0 & 0 \\ 0 & 0 & 0 & 0 \\ 0 & 0 & 0 & 0 \end{Bmatrix} \begin{Bmatrix} v_{Cs}(t) \\ i_{Ls}(t) \\ v_{Cp}(t) \\ i_{Lp}(t) \end{Bmatrix} + \begin{Bmatrix} 0 & 0 \\ \frac{1}{L_S} & 0 \\ 0 & 0 \\ 0 & \frac{1}{L_P} \end{Bmatrix} \begin{Bmatrix} V_{E1} \\ V_{E2} \end{Bmatrix} \tag{2-56}$$

or $$\frac{d\mathbf{x}(t)}{dt} = \mathbf{A}_B\mathbf{x}(t) + \mathbf{B}_B\mathbf{U}_B \tag{2-57}$$

The solution of the differential equations can be determined as follows. Differentiate (2-54) and substitute (2-53) into the resulting equation to give

$$\frac{d^2 i_{Ls}(t)}{dt^2} = -\omega_0{}^2 i_{Ls}(t) \tag{2-58}$$

Equation (2-58) gives the following time-domain solution for $i_{Ls}(t)$.

$$i_{Ls}(t) = i_{Ls}(t_0)\cos\omega_0(t-t_0) - \frac{v_{Cs}(t_0)-V_{E1}}{Z_0}\sin\omega_0(t-t_0) \tag{2-59}$$

Combining equations (2-59) and (2-54) gives the voltage equation.

$$v_{Cs}(t) = Z_0 i_{Ls}(t_0)\sin\omega_0(t-t_0) + \left[v_{Cs}(t_0)-V_{E1}\right]\cos\omega_0(t-t_0) \tag{2-60}$$

where Z_0 and ω_o are the characteristic impedance and the resonant frequency of the series L_s - C_s tank, respectively, and are defined by:

$$Z_0 = \sqrt{\frac{L_S}{C_S}} \tag{2-61}$$

and

$$\omega_0 = \frac{1}{\sqrt{L_S C_S}} \tag{2-62}$$

The solution of the differential equation (2-55) is given by:

$$i_{Lp}(t) = i_{Lp}(t_0) + \frac{V_{E2}}{L_P}(t-t_0) \tag{2-63}$$

The generic solution can be summarized in matrix form as

$$\begin{Bmatrix} v_{Cs}(t) \\ i_{Ls}(t) \\ v_{Cp}(t) \\ i_{Lp}(t) \end{Bmatrix} = \begin{Bmatrix} \cos\omega_0(t-t_i) & Z_0\sin\omega_0(t-t_i) & 0 & 0 \\ -\sin\omega_0(t-t_i)/Z_0 & \cos\omega_0(t-t_i) & 0 & 0 \\ 0 & 0 & 1 & 0 \\ 0 & 0 & 0 & 1 \end{Bmatrix} \begin{Bmatrix} v_{Cs}(t_i) \\ i_{Ls}(t_i) \\ v_{Cp}(t_i) \\ i_{Lp}(t_i) \end{Bmatrix} + \begin{Bmatrix} 1-\cos\omega_0(t-t_i) & 0 \\ \sin\omega_0(t-t_i)/Z_0 & 0 \\ 0 & 0 \\ 0 & (t-t_i)/L_P \end{Bmatrix} \begin{Bmatrix} V_{E1} \\ V_{E2} \end{Bmatrix} \tag{2-64}$$

or

$$\mathbf{x}(t) = \mathbf{S}_{B1}(t)\mathbf{x}(t_i) + \mathbf{S}_{B2}(t)\mathbf{U}_B \tag{2-65}$$

As in the previous Type A mode, the forward and reverse swing equations will be defined in terms of the initial and final conditions and the time duration.

The forward swing equations are

$$\mathbf{x}_f = \mathbf{A}_\theta \mathbf{x}_i + \mathbf{B}_\theta \mathbf{U}_B \tag{2-66}$$

and

$$\begin{Bmatrix} v_{Csf} \\ i_{Lsf} \\ v_{Cpf} \\ i_{Lpf} \end{Bmatrix} = \begin{Bmatrix} \cos\theta & Z_0 \sin\theta & 0 & 0 \\ -\frac{1}{Z_0}\sin\theta & \cos\theta & 0 & 0 \\ 0 & 0 & 1 & 0 \\ 0 & 0 & 0 & 1 \end{Bmatrix} \begin{Bmatrix} v_{Csi} \\ i_{Lsi} \\ v_{Cpi} \\ i_{Lpi} \end{Bmatrix} + \begin{Bmatrix} 1-\cos\theta & 0 \\ \frac{1}{Z_0}\sin\theta & 0 \\ 0 & 0 \\ 0 & \frac{1}{L_P}\frac{\theta}{\omega_0} \end{Bmatrix} \begin{Bmatrix} V_{E1} \\ V_{E2} \end{Bmatrix} \tag{2-67}$$

where θ is designated as the generic swing angle for Type B modes.

The reverse swing equations are

$$\mathbf{x}_i = \mathbf{A}_{-\theta}\mathbf{x}_f + \mathbf{B}_{-\theta}\mathbf{U}_B \tag{2-68}$$

and

$$\begin{Bmatrix} v_{Csi} \\ i_{Lsi} \\ v_{Cpi} \\ i_{Lpi} \end{Bmatrix} = \begin{Bmatrix} \cos\theta & -Z_0 \sin\theta & 0 & 0 \\ \frac{1}{Z_0}\sin\theta & \cos\theta & 0 & 0 \\ 0 & 0 & 1 & 0 \\ 0 & 0 & 0 & 1 \end{Bmatrix} \begin{Bmatrix} v_{Csf} \\ i_{Lsf} \\ v_{Cpf} \\ i_{Lpf} \end{Bmatrix} + \begin{Bmatrix} 1-\cos\theta & 0 \\ -\frac{1}{Z_0}\sin\theta & 0 \\ 0 & 0 \\ 0 & -\frac{1}{L_P}\frac{\theta}{\omega_0} \end{Bmatrix} \begin{Bmatrix} V_{E1} \\ V_{E2} \end{Bmatrix} \tag{2-69}$$

Now that the forward and reverse swing equations have been derived for Type A and B modes, the trajectory equations can be generated and solved as discussed in the next section.

2.3.3. Trajectory Solutions

The steady-state behavior and the resulting operating characteristics of the converter are determined as follows. For a given set of circuit inputs Trajectory 1 and Trajectory 2 can be defined by the solution of either ten equations in ten unknowns or eleven equations in eleven unknowns, respectively. The equation set is composed of four swing equations in each of the three modes plus the operating frequency equation. The complete set of forward and reverse swing equations for each trajectory are systematically reduced to a set of two equations and two unknowns. These two transcendental equations are then solved simultaneously by computer-based numerical iteration.

Many analyses of resonant converters use a state-plane diagram to aid in solving for the steady-state characteristics [1,6]. The state-plane diagram is not used here explicitly because of the multi-resonant nature of the converter and consequently, the focus of the present analysis is on numerically solving the Modal Analysis equations.

There are a number of different approaches of varying mathematical complexity for the reduction of the complete equation set and the generation of a numerical computer solution for the two trajectories. The following approach is valid for both trajectories and provides a general solution which limits the complexity of the mathematical procedure. The solution will initially be outlined for Trajectory 1 and then extended to include Trajectory 2.

2.3.3.1. Trajectory 1 Solution

Both Trajectories 1 and 2 have a total of six modes as summarized below in Table 2-1. The third column lists the mode type. The fourth and fifth columns show the polarities of the input and output voltages, respectively, for the particular mode. The sixth and seventh columns define the equivalent voltage sources for the simplified equivalent circuits. The eight and ninth columns shows the time duration and the resonant frequencies of each mode.

Table 2-1

Characteristics of the twelve modes defining Trajectories 1 and 2.

Traj.	**Mode**	**Type**	V_I	V_O	V_{E1}	V_{E2}	**Time**	**Freq.**
1	M1	B	+	-	$+V_I+V_O$	$-V_O$	t_α	ω_o
	M2	A	+	O.C.	$+V_I$	*N/A*	t_γ	ω_{o1}, ω_{o2}
	M3	B	+	+	$+V_I-V_O$	$+V_O$	t_β	ω_o
	M1’	B	-	+	$-V_I-V_O$	$+V_O$	t_α	ω_o
	M2’	A	-	O.C.	$-V_I$	*N/A*	t_γ	ω_{o1}, ω_{o2}
	M3’	B	-	-	$-V_I+V_O$	$-V_O$	t_β	ω_o
2	M4	A	+	O.C.	$+V_I$	*N/A*	$t_{\gamma1}$	ω_{o1}, ω_{o2}
	M5	B	+	-	$+V_I+V_O$	$-V_O$	t_α	ω_o
	M6	A	+	O.C.	$+V_I$	*N/A*	$t_{\gamma2}$	ω_{o1}, ω_{o2}
	M4’	A	-	O.C.	$-V_I$	*N/A*	$t_{\gamma1}$	ω_{o1}, ω_{o2}
	M5’	B	-	+	$-V_I-V_O$	$+V_O$	t_α	ω_o
	M6’	A	-	O.C.	$-V_I$	*N/A*	$t_{\gamma2}$	ω_{o1}, ω_{o2}

The block diagram in Fig. 2-7 is a graphical representation of the various modes of operation and their initial and final states for Trajectory 1. As can be seen from Fig. 2-7, all of the relevant variables are already accounted for in the block diagram. However, note that vector $\mathbf{x}_1$ contains only two unknowns, one fewer than $\mathbf{x}_0$ and $\mathbf{x}_3$. Thus, the matrix-based equation reduction for Trajectory 1 can focus on solving for the two unknowns in $\mathbf{x}_1$ at time instant t_1. Only two unknowns exist at t_1 because the rectifier has just initiated commutation with V_{Cp1} clamped at - V_O and I_{Ls1} equal to I_{Lp1}.

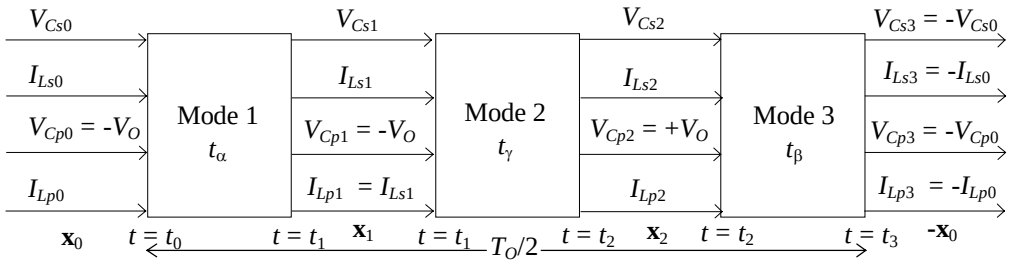

Fig. 2-7. Trajectory 1 block diagram.

The complementary sets of Modal Analysis matrix swing equations for Trajectory 1 are generated by substituting the boundary vectors into the previously derived generic swing equations.

Mode 1:

Forward: $$\mathbf{x}_1 = \mathbf{A}_\alpha \mathbf{x}_0 + \mathbf{B}_\alpha \mathbf{U}_{M1} \tag{2-70}$$

Reverse: $$\mathbf{x}_0 = \mathbf{A}_{-\alpha} \mathbf{x}_1 + \mathbf{B}_{-\alpha} \mathbf{U}_{M1} \tag{2-71}$$

Mode 2:

Forward: $$\mathbf{x}_2 = \mathbf{A}_\gamma \mathbf{x}_1 + \mathbf{B}_\gamma \mathbf{U}_{M2} \tag{2-72}$$

Reverse: $$\mathbf{x}_1 = \mathbf{A}_{-\gamma} \mathbf{x}_2 + \mathbf{B}_{-\gamma} \mathbf{U}_{M2} \tag{2-73}$$

Mode 3:

Forward: $$-\mathbf{x}_0 = \mathbf{A}_\beta \mathbf{x}_2 + \mathbf{B}_\beta \mathbf{U}_{M3} \tag{2-74}$$

Reverse: $$\mathbf{x}_2 = -\mathbf{A}_{-\beta} \mathbf{x}_0 + \mathbf{B}_{-\beta} \mathbf{U}_{M3} \tag{2-75}$$

Equation (2-72) expresses $\mathbf{x}_2$ in terms of $\mathbf{x}_1$ for Mode 2. The reverse swing equations for the other two modes, (2-71) and (2-75), are now combined to generate a second expression for $\mathbf{x}_2$ in terms of $\mathbf{x}_1$.

$$\mathbf{x}_2 = -\mathbf{A}_{-\beta}\left(\mathbf{A}_{-\alpha} \mathbf{x}_1 + \mathbf{B}_{-\alpha} \mathbf{U}_{M1}\right) + \mathbf{B}_{-\beta} \mathbf{U}_{M3} \tag{2-76}$$

or $$\mathbf{x}_2 = -\mathbf{A}_{-\beta} \mathbf{A}_{-\alpha} \mathbf{x}_1 - \mathbf{A}_{-\beta} \mathbf{B}_{-\alpha} \mathbf{U}_{M1} + \mathbf{B}_{-\beta} \mathbf{U}_{M3} \tag{2-77}$$

Equate the right hand sides of (2-72) and (2-77) to yield an expression in terms of $\mathbf{x}_1$ and the radian angles only:

$$\mathbf{A}_\gamma \mathbf{x}_1 + \mathbf{B}_\gamma \mathbf{U}_{M2} = -\mathbf{A}_{-\beta} \mathbf{A}_{-\alpha} \mathbf{x}_1 - \mathbf{A}_{-\beta} \mathbf{B}_{-\alpha} \mathbf{U}_{M1} + \mathbf{B}_{-\beta} \mathbf{U}_{M3} \tag{2-78}$$

which can be rearranged as:

$$\left(\mathbf{A}_\gamma + \mathbf{A}_{-\beta} \mathbf{A}_{-\alpha}\right) \mathbf{x}_1 = -\mathbf{A}_{-\beta} \mathbf{B}_{-\alpha} \mathbf{U}_{M1} + \mathbf{B}_{-\beta} \mathbf{U}_{M3} - \mathbf{B}_\gamma \mathbf{U}_{M2} \tag{2-79}$$

For simplicity, (2-79) will now be written in terms of two new matrices **G** and **H**:

$$\mathbf{G}\mathbf{x}_1 = \mathbf{H} \tag{2-80}$$

where

$$\mathbf{G} = \mathbf{A}_{\gamma} + \mathbf{A}_{-\beta}\mathbf{A}_{-\alpha} \tag{2-81}$$

and

$$\mathbf{H} = -\mathbf{A}_{-\beta}\mathbf{B}_{-\alpha}\mathbf{U}_{M1} + \mathbf{B}_{-\beta}\mathbf{U}_{M3} - \mathbf{B}_{\gamma}\mathbf{U}_{M2} \tag{2-82}$$

The matrices **G** and **H** are functions of the radian angles, α, β, and γ only, for a given set of circuit parameters.

Equation (2-80) consists of four equations and five unknowns, V_{Cs1}, I_{Ls1} α, β, and γ. The next step is to eliminate V_{Cs1}. Initially, express (2-80) in a more detailed format as follows:

$$\begin{Bmatrix} G_{11} & G_{12} & G_{13} & G_{14} \\ G_{21} & G_{22} & G_{23} & G_{24} \\ G_{31} & G_{32} & G_{33} & G_{34} \\ G_{41} & G_{42} & G_{43} & G_{44} \end{Bmatrix} \begin{Bmatrix} V_{Cs1} \\ I_{Ls1} \\ -V_O \\ I_{Ls1} \end{Bmatrix} = \begin{Bmatrix} H_1 \\ H_2 \\ H_3 \\ H_4 \end{Bmatrix} \tag{2-83}$$

Express V_{Cs1} in terms of the elements of the above equation as follows:

$$V_{Cs1} = -I_{Ls1}\left(\frac{G_{m2} + G_{m4}}{G_{m1}}\right) + \frac{H_m}{G_{m1}} - V_O\frac{G_{m2}}{G_{m1}} \tag{2-84}$$

for m = 1..4.

Voltage V_{Cs1} can be eliminated from the solution by equating the right hand sides of (2-84) as follows:

$$I_{Ls1}\left(\frac{G_{m2} + G_{m4}}{G_{m1}}\right) - \frac{H_m}{G_{m1}} + V_O\frac{G_{m2}}{G_{m1}} = I_{Ls1}\left(\frac{G_{(m+1)2} + G_{(m+1)4}}{G_{(m+1)1}}\right) - \frac{H_{(m+1)}}{G_{(m+1)1}} + V_O\frac{G_{(m+1)2}}{G_{(m+1)1}} \tag{2-85}$$

for m = 1..3.

Current I_{Ls1} can be expressed in terms of the radian angles.

$$I_{Ls1} = \frac{\dfrac{H_{(m+1)}}{G_{(m+1)1}} - V_O\dfrac{G_{(m+1)2}}{G_{(m+1)1}} - \dfrac{H_m}{G_{m1}} + V_O\dfrac{G_{m2}}{G_{m1}}}{\dfrac{G_{(m+1)2} + G_{(m+1)4}}{G_{(m+1)1}} - \dfrac{G_{m2} + G_{m4}}{G_{m1}}} \tag{2-86}$$

for m = 1..3.

Current I_{Ls1} can be eliminated form the solution set by equating the right hand sides of (2-86) as follows:

$$\frac{\dfrac{H_{(m+1)}}{G_{(m+1)1}} - V_O \dfrac{G_{(m+1)2}}{G_{(m+1)1}} - \dfrac{H_m}{G_{m1}} + V_O \dfrac{G_{m2}}{G_{m1}}}{\dfrac{G_{(m+1)2} + G_{(m+1)4}}{G_{(m+1)1}} - \dfrac{G_{m2} + G_{m4}}{G_{m1}}} = \frac{\dfrac{H_{(m+2)}}{G_{(m+2)1}} - V_O \dfrac{G_{(m+2)2}}{G_{(m+2)1}} - \dfrac{H_{(m+1)}}{G_{(m+1)1}} + V_O \dfrac{G_{(m+1)2}}{G_{(m+1)1}}}{\dfrac{G_{(m+2)2} + G_{(m+2)4}}{G_{(m+2)1}} - \dfrac{G_{(m+1)2} + G_{(m+1)4}}{G_{(m+1)1}}}$$

(2-87)

for m = 1, 2.

The pair of equations represented by (2-87) contains three unknowns α, β and γ. Angle β can be eliminated by using a third equation relating the operating frequency and the radian angles as follows,

$$f_O = \frac{\omega_0}{2\left(\alpha + \beta + \dfrac{\omega_0}{\omega_{01}}\gamma_1\right)} \tag{2-88}$$

where f_o is the operating frequency of the converter.

A Mathematica-based computer program has been written which solves numerically the two equations given by (2-87) in terms of two radian angles, α and γ. When a valid solution has been obtained, all the other trajectory unknowns can be determined from the relationships shown above. For example, β is given by (2-88), while the $\mathbf{x}_1$ unknowns, V_{Cs1} and I_{Ls1}, can be determined from (2-86) and (2-84), respectively. The other unknowns in $\mathbf{x}_0$ and $\mathbf{x}_1$ can easily be determined by using the swing equations (2-71) and (2-72), respectively.

All the converter waveforms can be constructed when the boundary values, $\mathbf{x}_0$, $\mathbf{x}_1$ and $\mathbf{x}_2$, and the radian angles, α, β and γ, have been determined for a given set of circuit inputs. As an example, the series tank current, $i_{Ls}(t)$ can be generated as follows. The currents for the Type B Modes 1 and 3 are easily determined.

Mode 1: $$i_{Ls}(t) = I_{Ls0}\cos\omega_0(t - t_0) - \frac{V_{Cs0} - V_I - V_O}{Z_0}\sin\omega_0(t - t_0) \tag{2-89}$$

Mode 3: $$i_{Ls}(t) = I_{Ls2}\cos\omega_0(t - t_2) - \frac{V_{Cs2} - V_I + V_O}{Z_0}\sin\omega_0(t - t_2) \tag{2-90}$$

The decoupled current variables $i_1(t)$ and $i_2(t)$ must first be determined in order to construct the actual currents in the Type A Mode 2.

Hence,

$$i_1(t) = (1+K_3)I_{Ls1}\cos\omega_{01}(t-t_1) - \frac{(V_{Cs1}-K_1V_O)-V_I}{Z_{01}}\sin\omega_{01}(t-t_1) \tag{2-91}$$

$$i_2(t) = (1+K_4)I_{Ls1}\cos\omega_{02}(t-t_1) - \frac{(V_{Cs1}-K_1V_O)-V_I}{Z_{02}}\sin\omega_{02}(t-t_1) \tag{2-92}$$

and as previously shown

$$i_{Ls}(t) = \frac{i_1(t)-i_2(t)}{K_4-K_3} \tag{2-93}$$

All the significant circuit voltages and currents for steady-state operation in Trajectory 1 can be similarly constructed. When this has been done, the average, peak and rms currents can be determined numerically.

2.3.3.2. Trajectory 2 Solution

The solution for Trajectory 2 can be determined in a similar manner to that employed to solve Trajectory 1. The block diagram for Trajectory 2 is given in Fig. 2-8. The principal difference from the solution for Trajectory 1 is that for Trajectory 2 the solution is based on the vector $\mathbf{x}_2$ at t_2 when the output rectifier commutates and only two unknowns exist.

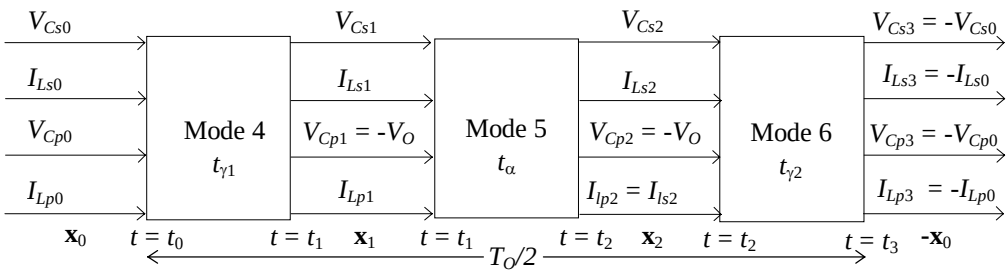

Fig. 2-8. Trajectory 2 block diagram.

A new set of forward and reverse equations can be generated for Trajectory 2.

Mode 4:

Forward: $$\mathbf{x}_1 = \mathbf{A}_{\gamma 1}\mathbf{x}_0 + \mathbf{B}_{\gamma 1}\mathbf{U}_{M4} \tag{2-94}$$

Reverse: $$\mathbf{x}_0 = \mathbf{A}_{-\gamma 1}\mathbf{x}_1 + \mathbf{B}_{-\gamma 1}\mathbf{U}_{M4} \tag{2-95}$$

Mode 5:

Forward: $$\mathbf{x}_2 = \mathbf{A}_{\alpha}\mathbf{x}_1 + \mathbf{B}_{\alpha}\mathbf{U}_{M5} \tag{2-96}$$

Reverse: $$\mathbf{x}_1 = \mathbf{A}_{-\alpha}\mathbf{x}_2 + \mathbf{B}_{-\alpha}\mathbf{U}_{M5} \tag{2-97}$$

Mode 6:

Forward: $$-\mathbf{x}_0 = \mathbf{A}_{\gamma 2}\mathbf{x}_2 + \mathbf{B}_{\gamma 2}\mathbf{U}_{M6} \tag{2-98}$$

Reverse: $$\mathbf{x}_2 = -\mathbf{A}_{-\gamma 2}\mathbf{x}_0 + \mathbf{B}_{-\gamma 2}\mathbf{U}_{M6} \tag{2-99}$$

The full equation set for Trajectory 2 can be reduced to a new equation set with two equations and two unknowns in an identical process to Trajectory 1. The only difference between the procedures is that in Trajectory 2 the decoupled variables in Modes 4 and 6 must first be transformed to actual circuit variables before peak, rms and average quantities can be evaluated. In the case of Trajectory 1 this was only necessary for Mode 2.

2.3.3.3. Program Flowchart

A program has been written to compute the steady-state converter characteristics for a given set of inputs. The flowchart for the Mathematica-based program is shown in Fig. 2-9.

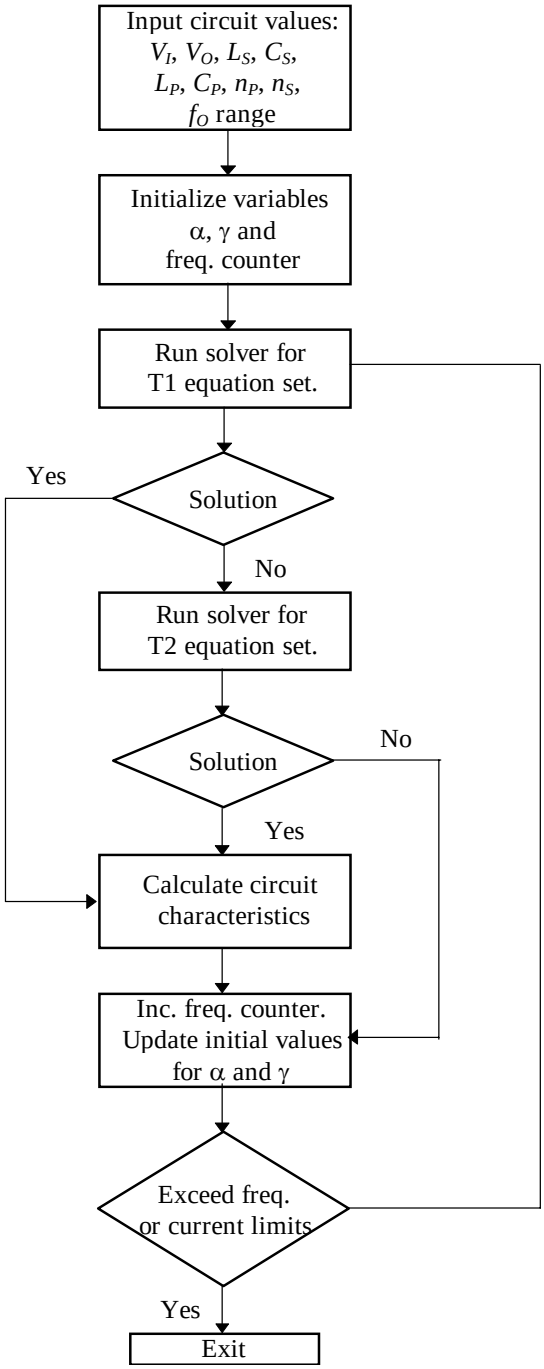

Fig. 2-9. Modal Analysis program flowchart.

The flow of the program is relatively simple. The program solves for α and γ, the variables which are common to both trajectories. The circuit component values, voltages and frequency range are given as inputs, and initial guesses are made for α

and γ. The program calculates the converter characteristics over a predefined frequency range and so a frequency counter is required. The program numerically solves the transcendental equations for Trajectory 1 (T1). If a valid solution does not exist in Trajectory 1, the program looks for a solution in Trajectory 2 (T2). A valid solution in either trajectory results in the circuit characteristics being calculated. The frequency counter is then incremented and the solution values are stored as the initial guesses for α and γ for the next operating frequency. If a valid solution does not exist, then the circuit may be operating outside the ZVS trajectories. Other possibilities such as insufficient accuracy or too few iterations can also result in failure to find a solution and care must be taken in selecting these control inputs.

2.3.4. Converter Characteristics

The converter characteristics for any given set of circuit parameters can be generated using the solution equations and computer program developed in the previous sections. Critical normalized converter currents are plotted in Fig. 2-10 to Fig. 2-12 for two values of the ratio L_r, defined as L_S/L_P, and for a fixed series tank natural resonant frequency, $\omega_{OS} = 0.5\ \omega_{OP}$. Voltages are normalized with respect to V_I the dc source voltage, and currents are normalized with respect to V_I/Z_{OP}, the input source voltage divided by the magnitude of the parallel tank characteristic impedance.

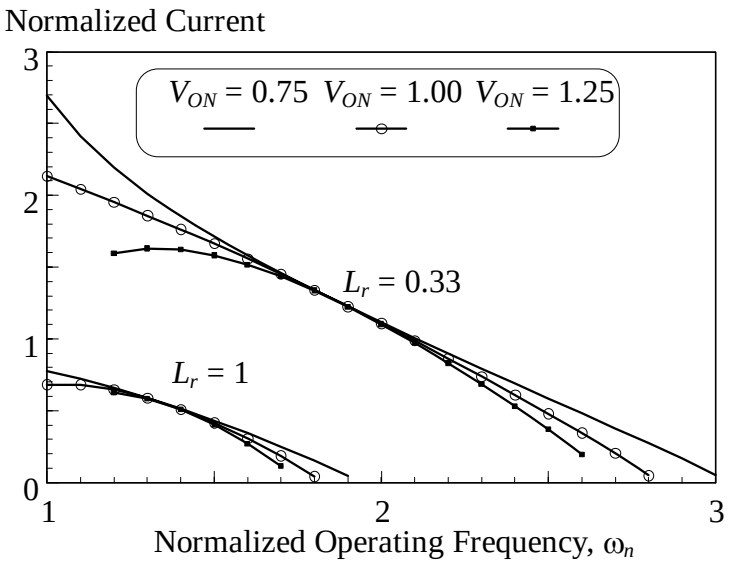

Fig. 2-10. Modal Analysis plots of I_{ON} as a function of ω_N at $\omega_{OS} = 0.5\omega_{OP}$.

The normalized dc output current, I_o, is plotted in Fig. 2-10. For the plots shown, the output current decreases as the operating frequency is increased. The general form of the output curves shows that the topology acts as a frequency-controlled current source over a significant part of the frequency range, thus rendering it ideally suitable to the inductive charging application. It is clear from both sets of curves that a current source frequency exists where the output current is independent of output voltage. This particular condition will be examined further in the next chapter.

For the range of voltages used in Fig. 2-10, the output power increases essentially monotonically as the frequency decreases over the frequency range. This linear large-signal transfer function characteristic of the topology greatly simplifies the design of the control loop. Additionally, the frequency range from zero to full load is limited to a reasonable value. For L_r = 1.0, the frequency range is just under 2:1, whilst for L_r = 0.33, the frequency range is increased to approximately 3:1 with a corresponding increase in output power.

As shown in Fig. 2-10, the output current and consequently the output power can effectively be reduced to zero by increasing the frequency. This is a critical characteristic for steady-state trickle charging of batteries.

The variation of the rms series tank current, I_{Ls}, as a function of frequency for a range of normalized output voltages is shown in Fig. 2-11. The plots illustrate that at the lower voltage levels, the series tank current decreases as the frequency increases and the output current decreases. However, at high output voltage levels, the current in the series tank can actually increase as frequency increases, peaking in the mid-frequency range near the current source frequency and then decreasing. This behavior can result in reduced efficiencies at light loads and higher output voltages.

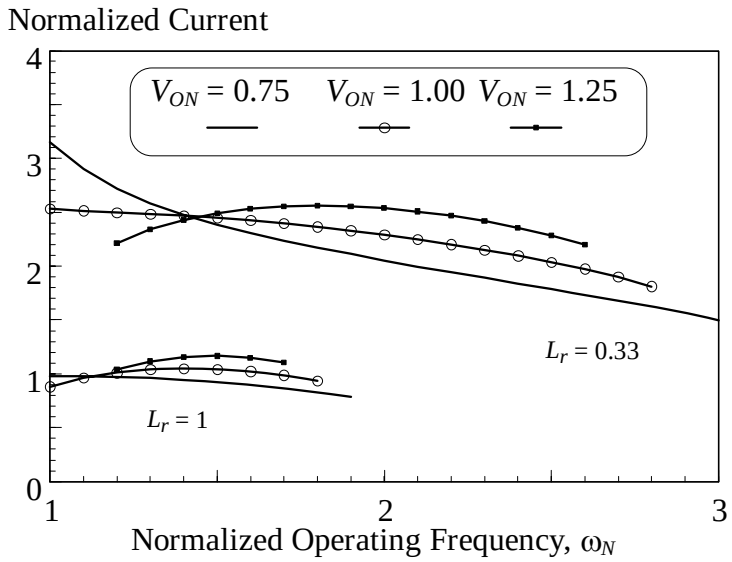

Fig. 2-11. Modal Analysis plots of I_{LsN} as a function of ω_N, at $\omega_{OS} = 0.5\ \omega_{OP}$.

A critical parameter for soft switching in the converter is the turn-off current in the switch, I_{QON} which is plotted in Fig. 2-12. The curves illustrate that over the required frequency range there is a significant current in the switch at turn-off. This current magnitude is critical as sufficient current must be present to completely charge and discharge the parasitic capacitances of the commutating switches and enable a soft switching voltage transition.

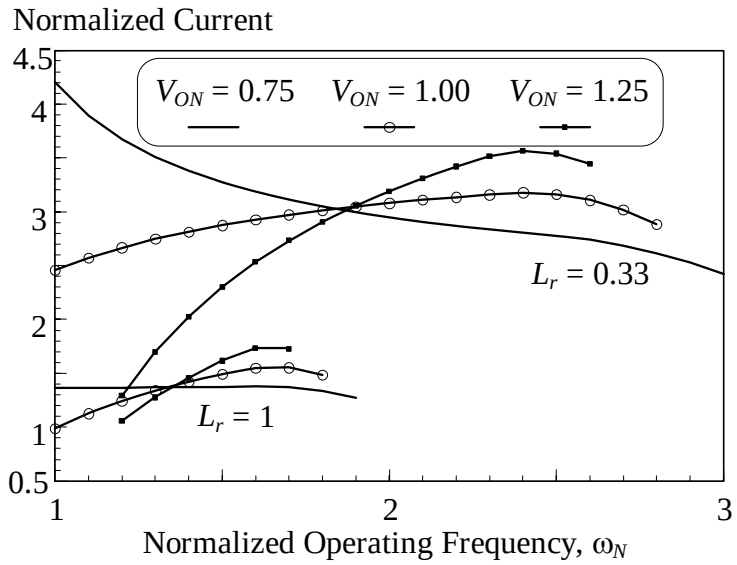

Fig. 2-12. Modal Analysis plots of I_{QON} as a function of ω_N, at $\omega_{OS} = 0.5\ \omega_{OP}$.

2.4. EXPERIMENTAL VALIDATION

A MOSFET-based prototype converter has been built and experimentally tested. The converter is designed to be SAE J-1773 compatible. The basic design

requirements of the converter are to output 1kW at 250V at a minimum frequency of 150 kHz. The converter has the following parameters:

$$V_I = 200 \text{ V}$$

$$f_{OS} = 27 \text{ kHz}$$

$$f_{OP} = 119 \text{ kHz}$$

$$Z_{OS} = 5.4\ \Omega$$

$$Y_{OP} = 0.03 \text{ S}$$

$$n_P = 4$$

$$n_S = 4$$

Experimental and theoretical converter waveforms for Trajectories 1 and 2 are shown in Fig. 2-13 and Fig. 2-14, respectively. The two sets of waveforms correlate closely. The parasitic oscillations in the experimental waveforms for v_I and v_{Cp} are independent of each other and are a function of the capacitances and parasitic inductances of the MOSFET-based H-bridge and the output rectifiers.

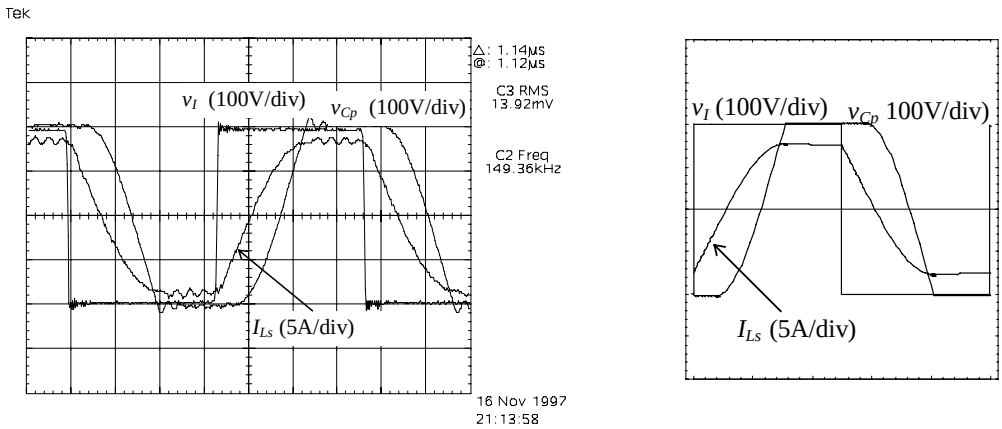

Fig. 2-13. Trajectory 1 experimental and theoretical waveforms for v_I, v_{Cp} and i_{Ls} at 150 kHz.

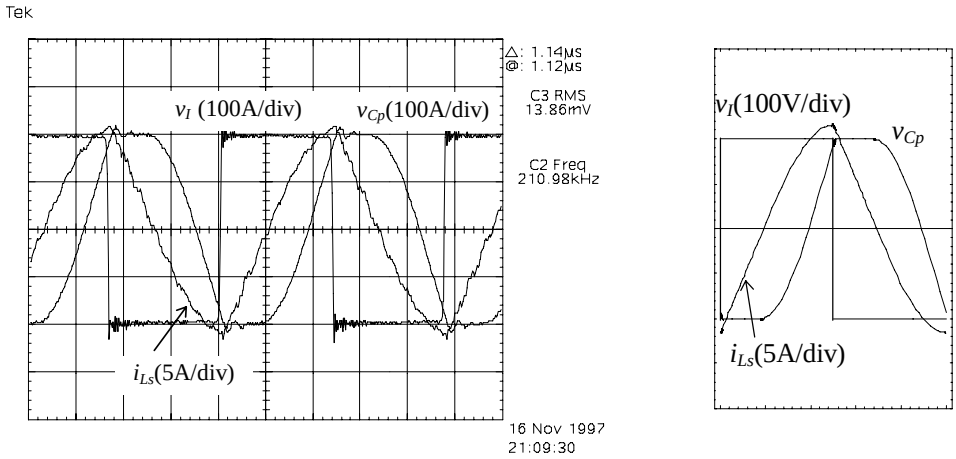

Fig. 2-14. Trajectory 2 experimental and theoretical waveforms for v_I, v_{Cp} and i_{Ls} at 220 kHz.

A comparison of experimental and analytical output power, P_o, is shown in Fig. 2-15. The experimental results correlate closely with the plots generated by the Modal Analysis. The discrepancy between the experimental data and the Modal Analysis data can be explained by the converter inefficiency. Converter efficiency is discussed in greater detail later in this section.

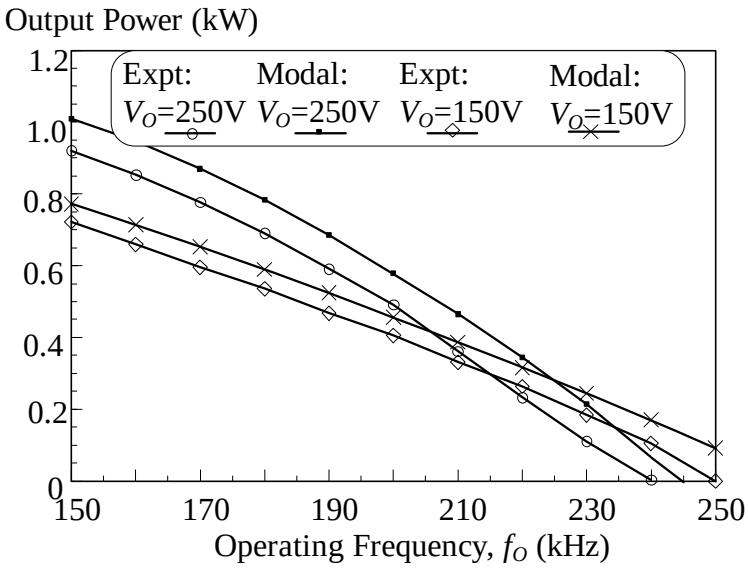

Fig. 2-15. Experimental and theoretical P_o, as a function of f_o for various V_o.

A comparison of experimental and theoretical data for two particular converter currents is shown in Fig. 2-16. The plots for the rms series tank current, I_{Ls}, and dc output current, I_o, agree well over the range, with a relatively consistent error between analysis and experimental data.

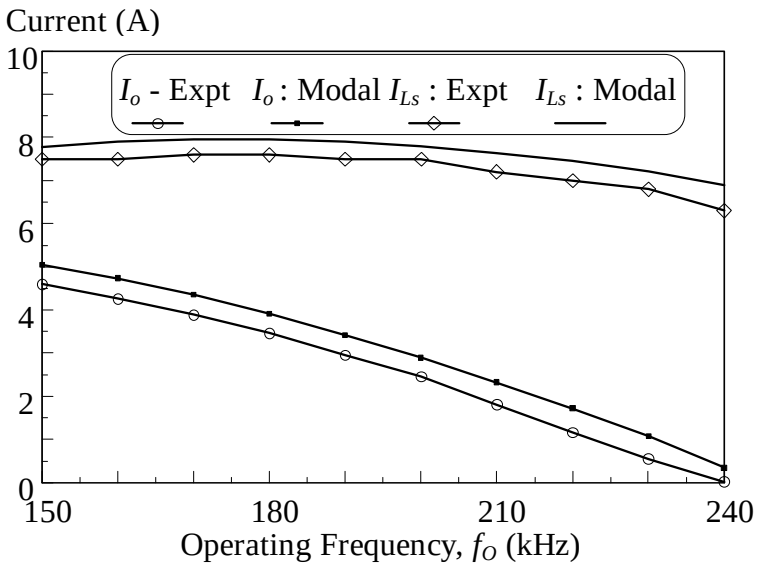

Fig. 2-16. Experimental and Modal Analysis plots of I_{Ls} and I_o, as a function of f_o at V_o = 200V.

The discrepancies between the predicted results and the measured experimental results are now investigated in greater detail. The Modal Analysis equations are solved to generate values for the critical currents in the converter. Fig. 2-17 and Fig. 2-18 plot the variations of the following converter currents as a function of operating frequency:

I_O = dc output current,

I_{Ls} = rms series tank current,

I_{Cb} = rms bus capacitor current,

I_Q = rms MOSFET current,

I_{QO} = instantaneous turn-off current in MOSFET,

I_{Dq} = average current of MOSFET antiparallel diode,

I_{Lp} = rms current in parallel or magnetizing inductance,

I_{Cp} = rms current in parallel capacitor,

I_{Do} = rms current in output rectifier diode,

I_{Co} = rms output capacitor current.

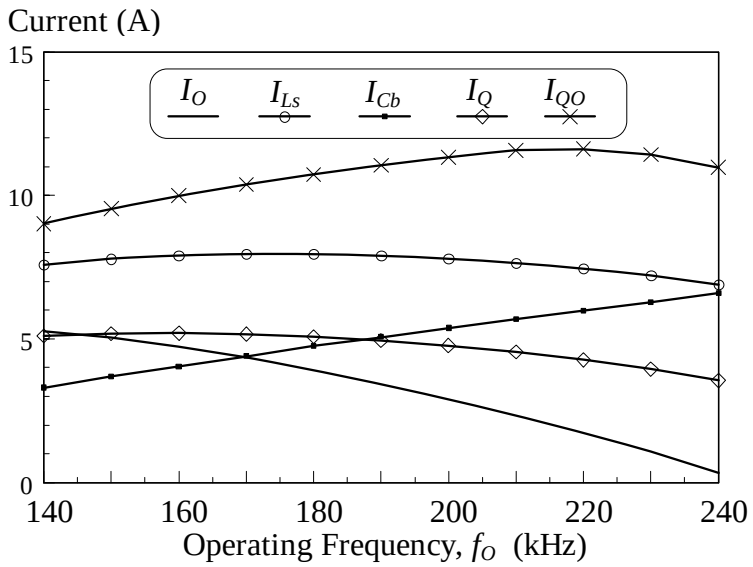

Fig. 2-17. Modal Analysis data sets for I_O, I_{Ls}, I_{Cb}, I_Q and I_{QO} as a function of f_O at V_O =200V.

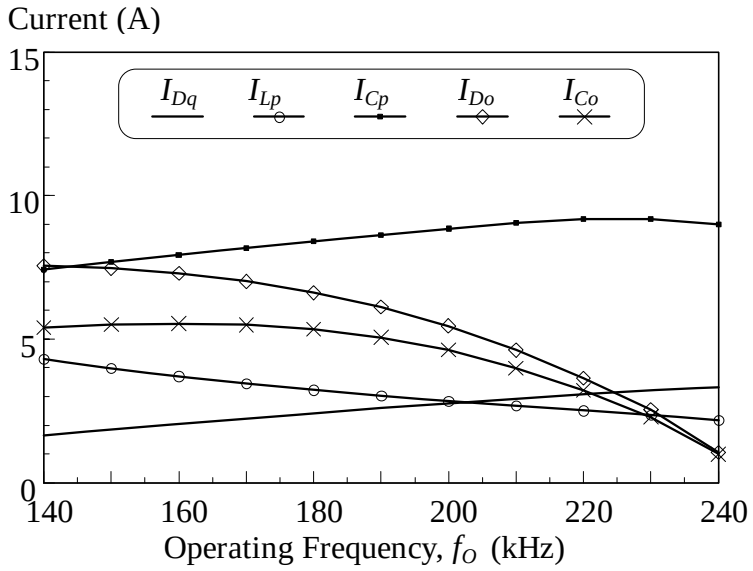

Fig. 2-18. Modal Analysis data sets for I_{Dq}, I_{Lp}, I_{Cp}, I_{Do} and I_{Co} as a function of f_O at V_O =200V.

Data from these current curve sets are combined with typical component specifications, such as MOSFET on-state resistance and diode forward voltage drop, to calculate theoretical power losses for the converter. Comparisons of measured and calculated power loss, P_L, and efficiency, η, are shown in Fig. 2-19 and the curves show good correlation. In addition, the curves show that most of the error between analytical and experimental results previously presented can be explained by converter inefficiency. Note that the calculated component power losses do not

consider second order loss mechanisms such as diode forward recovery or passive component resistance variations with frequency, etc.

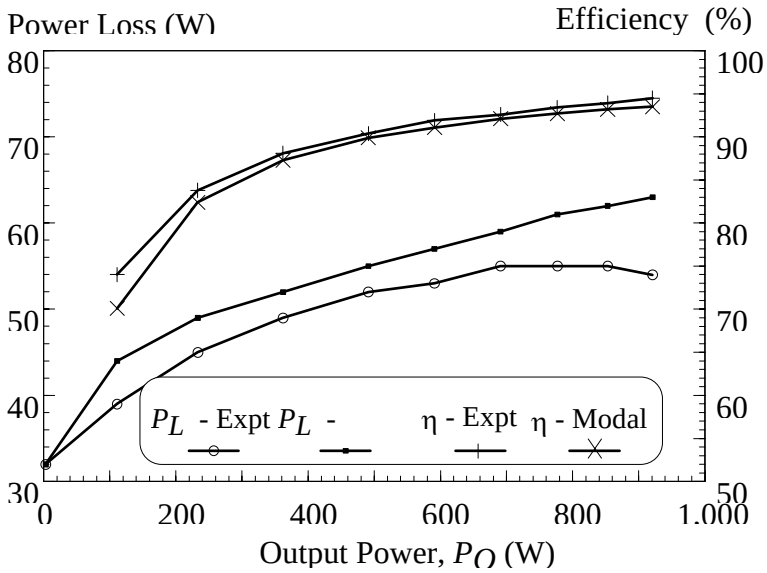

Fig. 2-19. Experimental and Modal Analysis plots of power loss and efficiency as a function of output power for V_o = 200V.

2.5. CONCLUSIONS

Driving the SAE J-1773 vehicle interface with a frequency-controlled series-resonant converter results in a four-element topology. In this chapter, the four-element topology is investigated, analyzed and characterized. Experimental and analytical results show that this topology has many desirable characteristics for use in inductive coupling battery charging, most notably:

1. Utilization of leakage inductance.
2. Optimized transformer turns ratio.
3. Buck/boost converter voltage gain.
4. Current source capability
5. Monotonic power transfer curve over a wide load range.
6. Throttling capability down to no-load.
7. High frequency operation.
8. Complementary lower-load/higher frequency operation.
9. Narrow control frequency range.
10. Zero-voltage switching.

11. High efficiency.
12. Inherent short circuit protection.
13. Soft recovery of output rectifiers.
14. Secondary dv/dt control.
15. Continuous-conduction-mode quasi-sinusoidal current wave shaping.

A novel time-domain analysis, known as Modal Analysis, is developed to derive the operating characteristics of the multi-element multi-resonant converter. In this analysis, the swing equations describing each mode of operation are derived and shown to form a highly coupled fourth-order system. Using a linear state-variable transformation technique the equation sets can be reduced to two decoupled second-order systems. The solution equations for the two second-order systems are transformed back into the fourth-order coupled system to give unique equations for the actual converter state variables. The full set of equations for each trajectory are then reduced to two transcendental equations in two unknowns which can be solved numerically for a given set of circuit inputs. The analysis is used to generate a detailed characterization of the topology.

Experimental results obtained from a MOSFET-based prototype converter show excellent correlation with the predictions generated by the Modal Analysis. The discrepancies between the measured and predicted results were investigated using a power loss model of the converter and are explained by the converter inefficiency.

REFERENCES

[1] R. Oruganti and F.C. Lee, "Resonant Power Processors: Part I - State Plane Analysis", *IEEE Industry Applications Conf. Rec*., 1984, pp. 860-867.

[2] R.L. Steigerwald, "Analysis of a Resonant Transistor DC-DC Converter with Capacitive Output Filter," *IEEE Trans. Industrial Electronics*, Vol. 1E-32, Nov. 1985, pp. 439-444.

[3] S.D. Johnson, R.W. Erickson, "Steady-State Analysis and Design of the Parallel Resonant Converter," *IEEE Power Electronics Specialists Conf. Rec*., 1986, pp. 154-165.

[4] A.K.S. Bhat, "Analysis and Design of a Series-Parallel Resonant Converter with Capacitive Output Filter," *IEEE Trans. Industry Applications*, Vol. 27, No. 3, May/June 1991, pp. 523-530.

[5] U. Kirchenberger, D. Schroeder, “Comparison of Multiresonant Half-Bridge DC-DC Converters for High Voltage and High Output Power,” *IEEE Industrial Applications Society Conf. Rec*., 1992, pp. 902-909.

[6] I. Batarseh, “Analysis and Design of High-Order Parallel Resonant Converters,” Ph.D. Dissertation, University of Illinois at Chicago, April, 1990.

[7] I. Batarseh and C.Q. Lee, “Steady-State Analysis of the Parallel Resonant Converter with LCLC Commutation Network,” *IEEE Trans. Power Electronics*, Vol. 6, No. 3, July 1991, pp. 525-538.

[8] J.G. Hayes, J.T. Hall, M.G. Egan, J.M.D. Murphy, “Full-Bridge, Series-Resonant Converter Supplying the SAE J-1773 Electric Vehicle Inductive Charging Interface,” *IEEE Power Electronics Specialists Conf. Rec*., 1996, pp. 1913-1918.

[9] J.G. Hayes, S.E. Schulz, J.T. Hall, M.G. Egan, J.M.D. Murphy, “Wide Load Range Resonant Converter Supplying the SAE J-1773 Electric Vehicle Inductive Charging Interface” *IEEE Industrial Applications Society Conf. Rec*., 1996, pp. 1065-1071.

[10] J. Cheng, A.F. Witulski, “Analytical Solutions for LLCC Parallel Resonant Converters Unify the Design and Analysis of Two- and Three- Element Converters,” *IEEE Power Electronics Specialists Conf. Rec*., 1996, pp. 266-271.

3.

CHAPTER THREE

FUNDAMENTAL MODE APPROXIMATION ANALYSIS OF THE SERIES-PARALLEL LCLC RESONANT CONVERTER WITH CAPACITIVE OUTPUT FILTER AND VOLTAGE-SOURCE LOAD

Abstract: In this chapter, the application of Fundamental Mode Approximation (FMA) Analysis to the four-element series-parallel LCLC resonant converter with capacitive output filter and voltage source load is investigated. The resulting understanding of the analytical technique and the specific application allows development of an extension to the basic FMA Analysis technique which is designated Rectifier-Compensated FMA (RCFMA) Analysis. RCFMA Analysis is a relatively simple, but very accurate analysis that provides a closed-form solution for the family of multi-element multi-resonant converters being studied. The development of FMA and RCFMA Analyses are discussed in detail and the results are compared with the more accurate but time intensive and mathematically complex Modal Analysis discussed in the previous chapter. A sample design procedure is presented.

3.1 INTRODUCTION

Driving the SAE J-1773 inductive charging interface with a series resonant converter results in a novel topology: the four-element, series-parallel LCLC resonant converter with a capacitive output filter. This topology has been analyzed in Chapter Two using the time-domain Modal Analysis which is mathematically complex and requires a numerical solution to transcendental equations [1,2]. Fundamental Mode Approximation (FMA) Analysis provides a much simpler and more intuitive approach for the analysis of resonant converters. The theoretical basis for FMA Analysis has been developed in references [3,4]. The objective is to analyze the resonant circuit in terms of the first harmonic or fundamental components of the circuit waveforms. FMA Analysis has been used extensively to analyze resonant circuits of different order and configuration [5,6], and also to investigate resonant converter topologies for the inductive charging application [7].

The application of FMA Analysis to two-element and three-element series-parallel converters with a capacitive output filter has also been investigated in [8].

As discussed in [3], FMA Analysis is particularly applicable to a converter which is super-resonant and Zero-Voltage-Switched (ZVS). Using FMA Analysis to study such converters results in a very simple, but accurate analysis because the resonant components significantly attenuate the higher-order harmonics. Thus, each circuit voltage and current can be approximated by the amplitude and phase of its fundamental component at the operating frequency. This approximation allows the application of single frequency ac circuit analysis to resonant converters of any configuration.

The FMA Analysis approach has usually modeled the load by an equivalent resistor except in [5] where the load is represented by an equivalent voltage source for a second-order series-resonant converter. Representing the load as a voltage source is particularly appropriate in the case of battery loads, the application upon which this work is based.

The first portion of this chapter applies the FMA Analysis technique to the four-element, series-parallel converter with capacitive output filter and voltage source load. While this approach provides a simple analysis, it is shown to have significant inaccuracies due to the limited applicability of the assumptions regarding the rms values and phase angles of the rectifier voltage and current.

A more in-depth understanding of the specific application allows development of an extension to the basic FMA Analysis known as Rectifier-Compensated FMA (RCFMA) Analysis. RCFMA Analysis is a reasonably simple, but very accurate analysis that provides a closed-form solution for the operation of multi-element, multi-resonant converters in the battery-charging application. The key to the simplicity of RCFMA Analysis is the use of a simplified time-domain model to generate accurate approximations for the true rms values and phase angles of the rectifier voltage and current. These approximations are then input to the basic FMA Analysis model.

The application of FMA Analysis to the converter is investigated in Section 3.2. The development of RCFMA Analysis is outlined in Section 3.3. A sample design using RCFMA Analysis is presented in Section 3.4.

The simplified equivalent circuit of the full-bridge SP-LCLC dc-dc converter with capacitive output filter and battery load is shown in Fig 3.1(a). The switching H-bridge is represented by a square-wave voltage source, $v_I(t)$. The input voltage is filtered by the four passive elements of the resonant tanks and the voltage across the parallel tank is rectified and fed to the dc battery or voltage-source load.

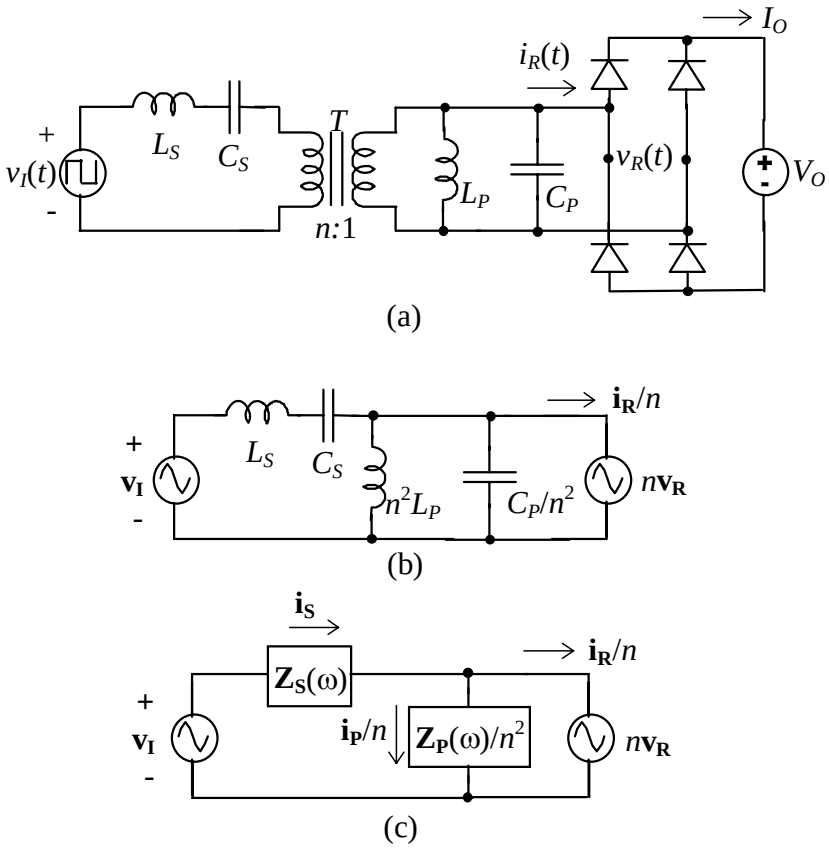

Fig. 3-1. Fundamental mode equivalent circuit.

In the fundamental mode equivalent circuit of Fig. 3-1(b), the input square-wave voltage source, $v_I(t)$, is represented by a sine wave voltage source phasor, $\mathbf{v_I}$, whose magnitude and phase are those of $v_{I,1}(t)$, the fundamental component of $v_I(t)$. Likewise, the voltage across the rectifier, $v_R(t)$, is represented by a sine wave voltage source phasor, $\mathbf{v_R}$, whose magnitude and phase are those of $v_{R,1}(t)$ the fundamental component of $v(t)$. Similarly, the current into the rectifier, $i_R(t)$, is represented by a sine wave current phasor, $\mathbf{i_R}$, whose magnitude and phase are those of $i_{R,1}(t)$ the fundamental component of $i_R(t)$. In the basic FMA Analysis, it is assumed that $v_{R,1}$(t)

and $i_{R,1}(t)$ are in phase with each other. In the RCFMA Analysis, this assumption is rejected and a more thorough investigation of the relationship between the rectifier voltage and current is conducted.

3.2.1 Basic Circuit Equations

From the simplified fundamental mode equivalent circuit of Fig 3.1(c), a relationship between the input voltage, the dc output voltage and the output current can be derived as outlined below.

The complex impedance and admittance of the series and parallel branches of the circuit are represented by $\mathbf{Z_S}(\omega)$ and $\mathbf{Y_P}(\omega)$, respectively, where ω is the operating or switching frequency of the converter. The phasors $\mathbf{i_S}$ and $\mathbf{i_P}$ represent the current in the series tank and the current in the parallel branch, respectively. The quantity n is the primary to secondary turns ratio of the transformer.

From Kirchhoff's voltage law

$$\mathbf{v_I} = \mathbf{Z_S}(\omega)\mathbf{i_S} + n\mathbf{v_R} \tag{3-1}$$

Substituting for the series current $\mathbf{i_S}$ gives

$$\mathbf{v_I} = \mathbf{Z_S}(\omega)\{\mathbf{i_R} + \mathbf{i_P}\}/n + n\mathbf{v_R} \tag{3-2}$$

Introducing the parallel branch relationship,

$$\mathbf{i_P} = \mathbf{Y_P}(\omega)\mathbf{v_R} \tag{3-3}$$

into (3-2) gives

$$\mathbf{v_I} = \{1 + \mathbf{Z_S}(\omega)\mathbf{Y_P}(\omega)/n^2\}n\mathbf{v_R} + \mathbf{Z_S}(\omega)\mathbf{i_R}/n \tag{3-4}$$

Equation (3-4) defines converter operation in terms of the input voltage, the output voltage and current, the circuit impedances, the operating frequency and the transformer turns ratio.

3.2.2 RMS and Phase Relationships

In FMA Analysis the following relationships are assumed.

(1) The input voltage to the tank, $v_I(t)$, is a square wave of amplitude V_I as shown in Fig. 3-2. The rms value, V_{Irms}, of the fundamental component of the square wave can be easily shown to be

$$V_{Irms} = \frac{2\sqrt{2}}{\pi} V_I \tag{3-5}$$

The fundamental component, $v_{I,1}(t)$, is in phase with $v_I(t)$ as shown in Fig. 3-2.

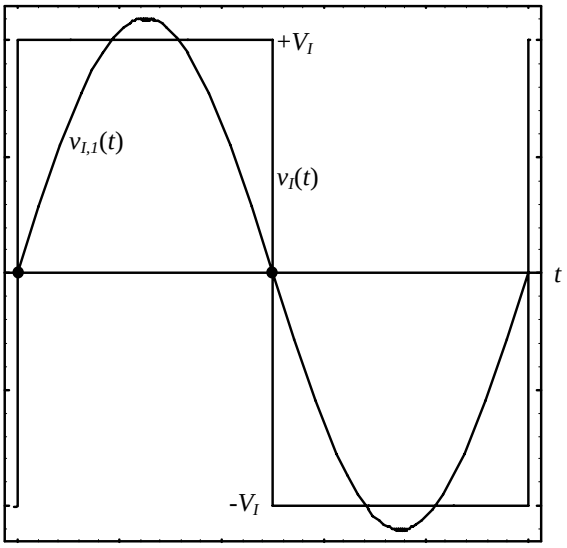

Fig. 3-2. Input voltage, $v_I(t)$, and its fundamental component, $v_{I,1}(t)$.

(2) As was previously shown in Chapter Two, the output rectifier voltage $v_R(t)$ is only approximately a square wave, but for the purpose of the FMA Analysis, $v_R(t)$ is assumed to be a square wave of amplitude V_O, where V_O is the dc output or battery voltage, as shown in Fig. 3-3. The rms value of the fundamental rectifier voltage, V_{Rrms}, is then given by

$$V_{Rrms} = \frac{2\sqrt{2}}{\pi} V_O \tag{3-6}$$

It is also assumed that the fundamental component, $v_{R,1}(t)$, is in phase with $v_R(t)$, as shown in Fig. 3-3.

(3) The current, $i_R(t)$, into the rectifier bridge is assumed to be a sine wave in phase with $v_R(t)$, and having a rectified average value equal to the dc output or battery current I_O. The relationship between the fundamental rms component I_{Rrms} and the average of the sinusoidal output current is

$$I_{Rrms} = \frac{\pi}{2\sqrt{2}} I_O \tag{3-7}$$

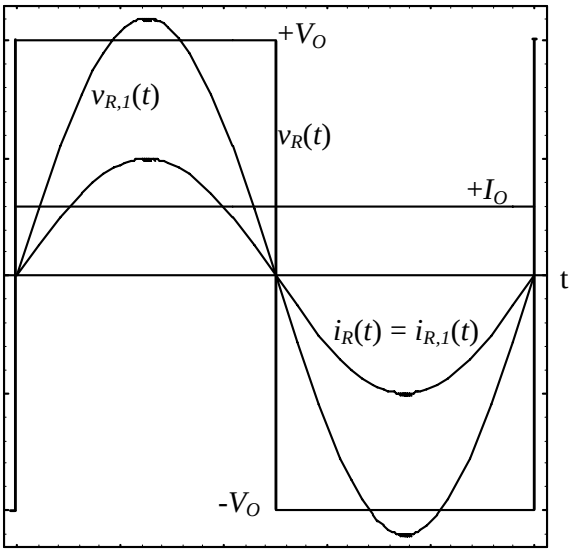

Fig. 3-3. Output current, I_O, rectifier voltage, $v_R(t)$, and rectifier current, $i_R(t)$, and their fundamental components, $v_{R,1}(t)$ and $i_{R,1}(t)$.

3.2.3 Circuit Impedances

The series tank impedance, $\mathbf{Z_S}(\omega)$ is defined by

$$\mathbf{Z}_S(\omega) = j\omega L_S + \frac{1}{j\omega C_S} \tag{3-8}$$

The natural resonant frequency, ω_{OS}, and the characteristic impedance, Z_{OS}, of the series resonant tank are defined by:

$$Z_{OS} = \sqrt{\frac{L_S}{C_S}} \tag{3-9}$$

and

$$\omega_{OS} = \frac{1}{\sqrt{L_S C_S}} \tag{3-10}$$

Substituting (3-9) and (3-10) into (3-8) results in equation (3-11) which defines $\mathbf{Z_S}(\omega)$ in terms of the characteristic impedance and resonant frequency.

$$\mathbf{Z_S}(\omega) = j\frac{\omega}{\omega_{OS}}\left(1-\frac{\omega_{OS}^{\ 2}}{\omega^2}\right)Z_{OS} \tag{3-11}$$

$$\mathbf{Z_S}(\omega) = jZ_S(\omega) \tag{3-12}$$

Thus, $Z_S(\omega)$ is the magnitude of the series tank impedance and is defined by

$$Z_S(\omega) = \frac{\omega}{\omega_{OS}}\left(1-\frac{\omega_{OS}^{\ 2}}{\omega^2}\right)Z_{OS} \tag{3-13}$$

Similarly, the admittance of the parallel tank, $\mathbf{Y_P}(\omega)$, composed of inductance L_P in parallel with capacitance C_P is defined by

$$\mathbf{Y_P}(\omega) = j\omega C_P + \frac{1}{j\omega L_P} \tag{3-14}$$

The resonant frequency, ω_{OP}, and the characteristic admittance, Y_{OP}, of the parallel resonant tank are defined by:

$$Y_{OP} = \sqrt{\frac{C_P}{L_P}} \tag{3-15}$$

and

$$\omega_{OP} = \frac{1}{\sqrt{L_P C_P}} \tag{3-16}$$

Substituting (3-15) and (3-16) into (3-14) results in equation (3-17) which defines $\mathbf{Y_P}(\omega)$ in terms of the characteristic admittance and resonant frequency.

$$\mathbf{Y_P}(\omega) = j\frac{\omega}{\omega_{OP}}\left(1-\frac{\omega_{OP}^{\ 2}}{\omega^2}\right)Y_{OP} \tag{3-17}$$

$$\mathbf{Y_P}(\omega) = jY_{OP}(\omega) \tag{3-18}$$

Thus, $Y_P(\omega)$ is the magnitude of the admittance of the parallel tank and is defined by

$$Y_P(\omega) = \frac{\omega}{\omega_{OP}}\left(1-\frac{\omega_{OP}^{\ 2}}{\omega^2}\right)Y_{OP} \tag{3-19}$$

Substituting (3-12) and (3-18) into the basic circuit equation (3-4) gives

$$\mathbf{v_I} = \left\{1 - Z_S(\omega)Y_P(\omega)/n^2\right\}n\mathbf{v_R} + jZ_S(\omega)\mathbf{i_R}/n \tag{3-20}$$

The circuit equation can be expressed in terms of the tank characteristic frequencies, admittance and impedance by substituting (3-13) and (3-19) into (3-20).

$$\mathbf{v_I} = \left\{1-\frac{\omega^2}{n^2\omega_{OS}\omega_{OP}}\left(1-\frac{\omega_{OS}^{\ 2}}{\omega^2}\right)\left(1-\frac{\omega_{OP}^{\ 2}}{\omega^2}\right)Z_{OS}Y_{OP}\right\}n\mathbf{v_R} + j\frac{\omega}{\omega_{OS}}\left(1-\frac{\omega_{OS}^{\ 2}}{\omega^2}\right)Z_{OS}\mathbf{i_R}/n \tag{3-21}$$

3.2.4 Current-Source Operation

Referring to (3-20), it can be seen that a particular frequency ω_C exists such that the coefficient of $\mathbf{v_R}$ is set to zero. Thus, at ω_C,

$$1 - Z_S(\omega_C)Y_P(\omega_C)/n^2 = 0 \tag{3-22}$$

Substituting (3-22) into (3-20) gives the rectifier current at ω_C as

$$\mathbf{i_R} = \frac{n\mathbf{v_I}}{Z_S(\omega_C)} \tag{3-23}$$

We can express the rectified output current I_O in terms of the input voltage V_I and series tank impedance at ω_C by substituting (3-5) and (3-7) into (3-23) as follows

$$I_O = \frac{8}{\pi^2}\frac{nV_I}{Z_S(\omega_C)} \tag{3-24}$$

At ω_C, the output voltage V_O has been eliminated from the circuit equation and the output current magnitude is determined only by the source voltage and the series tank impedance at $\omega = \omega_C$. Clearly, at ω_C the converter acts as a current source and ω_C is henceforth referred to as the current-source frequency.

The equation defining ω_C can be obtained by substituting (3-13) and (3-19) into (3-22).

$$1 - \frac{\omega_C^{\ 2}}{n^2\omega_{OS}\omega_{OP}}\left(1 - \frac{\omega_{OS}^{\ 2}}{\omega_C^{\ 2}}\right)\left(1 - \frac{\omega_{OP}^{\ 2}}{\omega_C^{\ 2}}\right)Z_{OS}Y_{OP} = 0 \tag{3-25}$$

It can also be seen that the current-source frequency, ω_C, is the resonant frequency of the equivalent parallel resonant circuit made up of Z_S and Y_P, with the output terminals open-circuited. Thus, ω_C is that frequency at which the impedance, looking from the input terminals, goes to zero.

Equation (3-25) can be used to express Z_{OS} in terms of Y_{OP} and the characteristic frequencies, ω_{OS}, ω_{OP} and ω_C.

$$Z_{OS} = \frac{1}{\frac{\omega_C^{\ 2}}{n^2\omega_{OS}\omega_{OP}}\left(1 - \frac{\omega_{OS}^{\ 2}}{\omega_C^{\ 2}}\right)\left(1 - \frac{\omega_{OP}^{\ 2}}{\omega_C^{\ 2}}\right)Y_{OP}} \tag{3-26}$$

Substituting (3-26) into (3-21), the voltage equation of the series-parallel converter can be defined in terms of ω_{OS}, ω_{OP} and ω_C such that

$$\mathbf{v_I} = \left\{1 - \frac{\omega^2\left(1-\frac{\omega_{OS}{}^2}{\omega^2}\right)\left(1-\frac{\omega_{OP}{}^2}{\omega^2}\right)}{\omega_C{}^2\left(1-\frac{\omega_{OS}{}^2}{\omega_C{}^2}\right)\left(1-\frac{\omega_{OP}{}^2}{\omega_C{}^2}\right)}\right\} n\mathbf{v_R} + j\frac{\omega}{n\omega_{OS}}\left(1-\frac{\omega_{OS}{}^2}{\omega^2}\right) Z_{OS}\mathbf{i_R}/n \qquad (3\text{-}27)$$

3.2.5 Phasor Analysis and Circuit Solution

Equation (3-20) describing the operation of the converter can be expressed in terms of phasor quantities as follows:

$$V_{Irms}\angle\delta_I = \left\{1 - Z_S(\omega)Y_P(\omega)/n^2\right\} nV_{Rrms}\angle\delta_V + jZ_S(\omega)\left(I_{Rrms}/n\right)\angle\delta_A \qquad (3\text{-}28)$$

where δ_I is the phase angle of the input voltage, and δ_V and δ_A are the phase angles of the rectifier voltage and current, respectively. According to the FMA Analysis assumptions the phase angles δ_V and δ_A are equal and are taken to be zero, i.e. $\mathbf{v_R}$ and $\mathbf{i_R}$ are the reference phasors.

Substitute the dc variables into (3-28) and express in complex notation:

$$\frac{2\sqrt{2}}{\pi}V_I\left(\cos\delta_I + j\sin\delta_I\right) = \left\{1 - Z_S(\omega)Y_P(\omega)/n^2\right\}\frac{2\sqrt{2}}{\pi}nV_O + jZ_S(\omega)\frac{\pi}{2\sqrt{2}}\frac{I_O}{n} \qquad (3\text{-}29)$$

giving $V_I\left(\cos\delta_I + j\sin\delta_I\right) = \left\{1 - Z_S(\omega)Y_P(\omega)/n^2\right\}nV_O + jZ_S(\omega)\frac{\pi^2}{8}\frac{I_O}{n}$ (3-30)

The above circuit equation can be expressed in non-complex form by equating the real and imaginary components:

$$V_I\cos\delta_I = \left\{1 - Z_S(\omega)Y_P(\omega)/n^2\right\}nV_O \qquad (3\text{-}31)$$

$$V_I\sin\delta_I = Z_S(\omega)\frac{\pi^2}{8}\frac{I_O}{n} \qquad (3\text{-}32)$$

Squaring both sides of the above two equations and adding gives the following equation:

$$V_I{}^2 = \left\{1 - Z_S(\omega)Y_P(\omega)/n^2\right\}^2 n^2V_O{}^2 + \left(Z_S(\omega)\frac{\pi^2}{8n}\right)^2\left(\frac{I_O}{n}\right)^2 \qquad (3\text{-}33)$$

which can also be written in standard elliptical format as

$$V_I{}^2 = \frac{n^2V_O{}^2}{\left\{\frac{1}{1 - Z_S(\omega)Y_P(\omega)/n^2}\right\}^2} + \frac{\left(I_O/n\right)^2}{\left(\frac{8}{\pi^2}\frac{1}{Z_S(\omega)}\right)^2} \qquad (3\text{-}34)$$

Equation (3-34) is a very important equation as it can be used to calculate or plot any single unknown for a given set of circuit parameters or to develop design characteristics for the converter. For example, the dc output current I_o can be determined if the input and output voltages and circuit parameters are known.

$$I_O = \frac{8n}{\pi^2}\frac{1}{Z_S(\omega)}\sqrt{V_I^{\,2} - \left(1 - Z_S(\omega)Y_P(\omega)/n^2\right)^2 n^2 V_O^{\,2}} \tag{3-35}$$

Equation (3-35) can alternatively be expressed in terms of ω_{OS}, ω_{OP} and ω_C and Z_{OS}.

$$I_O = \frac{8n}{\pi^2}\frac{1}{\frac{\omega}{\omega_{OS}}\left(1-\frac{\omega_{OS}^{\,2}}{\omega^2}\right)Z_{OS}}\sqrt{V_I^{\,2} - \left[1 - \frac{\omega^2\left(1-\frac{\omega_{OS}^{\,2}}{\omega^2}\right)\left(1-\frac{\omega_{OP}^{\,2}}{\omega^2}\right)}{\omega_C^{\,2}\left(1-\frac{\omega_{OS}^{\,2}}{\omega_C^{\,2}}\right)\left(1-\frac{\omega_{OP}^{\,2}}{\omega_C^{\,2}}\right)}\right]^2 n^2 V_O^{\,2}} \tag{3-36}$$

Equation (3-36) can also be expressed in terms of the parallel tank admittance by substituting (3-26) into (3-36) as follows.

$$I_O = \frac{8Y_{OP}}{n\pi^2}\frac{\omega_C^{\,2}\left(1-\frac{\omega_{OS}^{\,2}}{\omega_C^{\,2}}\right)\left(1-\frac{\omega_{OP}^{\,2}}{\omega_C^{\,2}}\right)}{\omega_{OP}\omega\left(1-\frac{\omega_{OS}^{\,2}}{\omega^2}\right)}\sqrt{V_I^{\,2} - \left[1 - \frac{\omega^2\left(1-\frac{\omega_{OS}^{\,2}}{\omega^2}\right)\left(1-\frac{\omega_{OP}^{\,2}}{\omega^2}\right)}{\omega_C^{\,2}\left(1-\frac{\omega_{OS}^{\,2}}{\omega_C^{\,2}}\right)\left(1-\frac{\omega_{OP}^{\,2}}{\omega_C^{\,2}}\right)}\right]^2 n^2 V_O^{\,2}} \tag{3-37}$$

If I_o is known, other critical circuit currents can be easily derived. In this analysis, the currents in the parallel branch are independent of the output current and only dependent on output voltage.

The current in the parallel branch is obtained by substituting (3-6) and (3-17) into (3-3). If $\mathbf{v_R}$ is the reference phasor, then

$$\mathbf{i_P} = j\frac{\omega}{\omega_{OP}}\left(1-\frac{\omega_{OP}^{\,2}}{\omega^2}\right)Y_{OP}\frac{2\sqrt{2}}{\pi}V_O \tag{3-38}$$

The currents $\mathbf{i_{Cp}}$ and $\mathbf{i_{Lp}}$ in the parallel capacitor and the parallel inductance, respectively, are easily derived as:

$$\mathbf{i_{Cp}} = j\frac{\omega}{\omega_{OP}}Y_{OP}\frac{2\sqrt{2}}{\pi}V_O \tag{3-39}$$

and

$$\mathbf{i_{Lp}} = -j\frac{\omega_{OP}}{\omega}Y_{OP}\frac{2\sqrt{2}}{\pi}V_O \tag{3-40}$$

The series tank current, $\mathbf{i_S}$, is the sum of the reflected rectifier current and the parallel tank current,

$$\mathbf{i_S} = \mathbf{i_R} / n + \mathbf{i_P} / n \tag{3-41}$$

or

$$\mathbf{i_S} = \frac{\pi}{2\sqrt{2}} \frac{I_O}{n} + j \frac{\omega}{\omega_{OP}} \left(1 - \frac{\omega_{OP}{}^2}{\omega^2} \right) Y_{OP} \frac{2\sqrt{2}}{\pi n} V_O \tag{3-42}$$

The phase angle of $\mathbf{i_S}$, δ_S , is easily determined:

$$\delta_S = \tan^{-1}\left(\frac{|\mathbf{i_P}|}{|\mathbf{i_R}|} \right) = \tan^{-1}\left[\frac{8}{\pi^2} \frac{\omega}{\omega_{OP}} \left(1 - \frac{\omega_{OP}{}^2}{\omega^2} \right) \frac{Y_{OP} V_O}{I_O} \right] \tag{3-43}$$

The phase angle of the input voltage, δ_I , is given by (3-31) as

$$\delta_I = \cos^{-1}\left\{ 1 - Z_S(\omega) Y_P(\omega) / n^2 \right\} n V_O / V_I \tag{3-44}$$

The power factor angle, δ_L, of the series current relative to input voltage is given by

$$\delta_L = \delta_I - \delta_S \tag{3-45}$$

The current in the transistors is the main heat generating current in the bridge. This current is designated $i_Q(t)$ and is equal to the series current in each half cycle from δ_L to π. The rms current per transistor I_{Qrms} is given by

$$I_{Qrms} = I_S \sqrt{\left[\pi - \delta_L - 0.5 \sin 2(\pi - \delta_L) \right] / 2\pi} \tag{3-46}$$

where I_s is the rms value of the series tank current.

3.2.6 Normalization and Converter Characterization

The circuit voltage equation can be normalized in terms of voltage, current and frequency. The normalizing voltage can be either input or output voltage. The normalizing current can be the normalizing voltage divided by either of the tank characteristic impedances. Similarly, the normalizing frequency can be any of the three resonant frequencies, ω_{OS}, ω_{OP} or ω_C.

For the purpose of discussing the generic behavior of the converter, the normalizing values are chosen as the input voltage and the parallel tank characteristic impedance and resonant frequency. The parallel tank is chosen as the reference because it is the only tank specified in the inductive coupling standard, SAE J-1773. The circuit may also be normalized using the series tank at its resonant frequency, or at the current-source frequency, and this may be preferable depending on the design constraints. In the following treatment, voltages are normalized with respect to the input voltage, V_I; currents are normalized with respect to the product of the input voltage and the parallel tank characteristic admittance, V_I Y_{OP} and

frequencies are normalized with respect to the parallel tank resonant frequency, ω_{OP}. The subscript "N" is added to each variable to show that it is a normalized variable.

Rewriting (3-37) in normalized form gives

$$I_{ON} = \frac{8}{n\pi^2} \frac{\omega_{CN}^{\ 2}\left(1-\frac{\omega_{OSN}^{\ 2}}{\omega_{CN}^{\ 2}}\right)\left(1-\frac{1}{\omega_{CN}^{\ 2}}\right)}{\omega_N\left(1-\frac{\omega_{OSN}^{\ 2}}{\omega_N^{\ 2}}\right)} \sqrt{1-\left[1-\frac{\omega_N^{\ 2}\left(1-\frac{\omega_{OSN}^{\ 2}}{\omega_N^{\ 2}}\right)\left(1-\frac{1}{\omega_N^{\ 2}}\right)}{\omega_{CN}^{\ 2}\left(1-\frac{\omega_{OSN}^{\ 2}}{\omega_{CN}^{\ 2}}\right)\left(1-\frac{1}{\omega_{CN}^{\ 2}}\right)}\right]^2 n^2 V_{ON}^{\ 2}} \tag{3-47}$$

The above equation represents an ellipse when plotted in the plane of I_{ON} and V_{ON} and Fig. 3-4 shows the elliptical plot for various values of ω_N all four quadrants of operation.

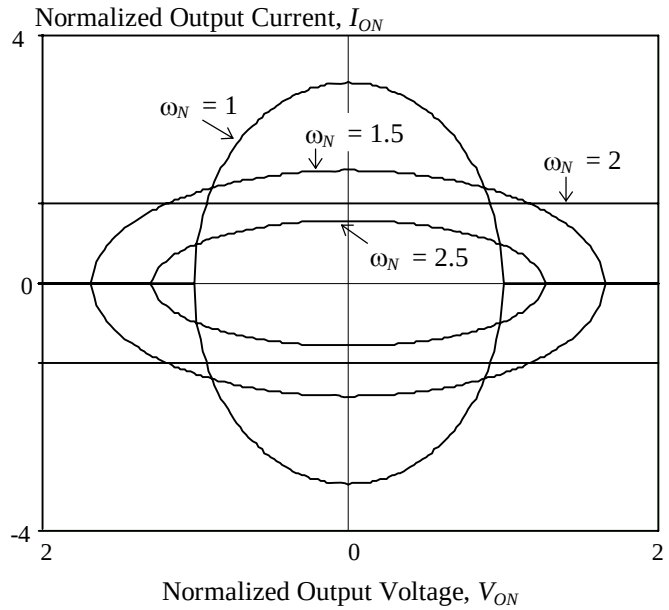

Fig. 3-4. Normalized output current, I_{ON}, as a function of normalized output voltage, V_{ON}, for various values of ω_N , at ω_{CN} = 2 and ω_{OSN} = 0.5.

The four quadrants are of course symmetrical and the first quadrant represents the power transfer quadrant for battery charging. These plots illustrate graphically the charging characteristics of the series-parallel topology with a voltage-source load. At a low frequency of ω_N = 1, the parallel admittance is zero and the only significant tank is the series tank. Thus, the converter acts as a series resonant converter and has no voltage boosting capability but significant current is available at the lower voltages. As the frequency is increased to ω_N = 1.5, the converter can provide a voltage boost as the parallel admittance has increased and is capacitive.

However, the available current is reduced at the lower voltages. At the current-source frequency of $\omega_N = 2$, the converter has theoretically infinite voltage gain for a constant output current. Increasing the frequency beyond the current-source frequency to $\omega_N = 2.5$ results in a reduction of the voltage gain and available output current at the lower voltages. As the frequency is increased further, the voltage gain and output current continue to decrease.

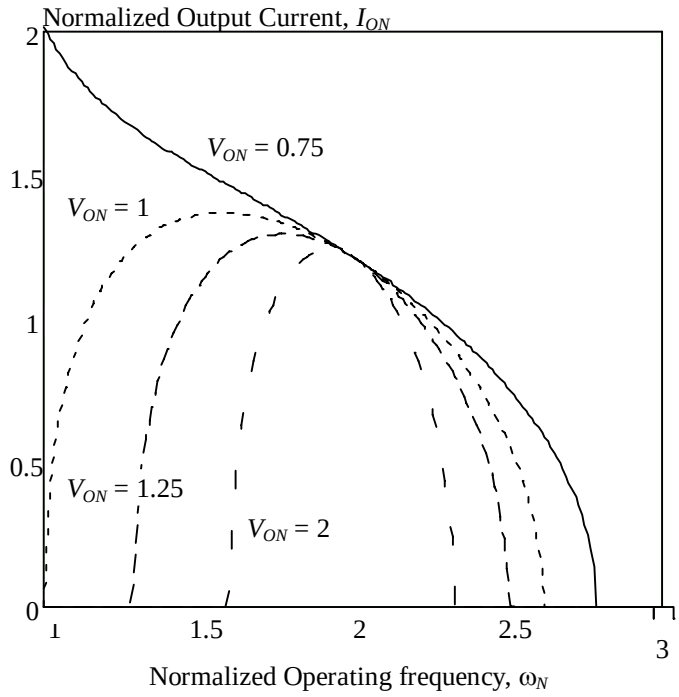

Fig. 3-5. Plot of normalized output current, I_{ON}, as a function of normalized operating frequency, ω_N, for various values of V_{ON} at $\omega_{OSN} = 0.5$ and $\omega_{CN} = 2$.

Using (3-47) The output current can also be plotted as a function of the normalized operating frequency ω_N for constant values of V_{ON}, as shown in Fig. 3-5. For the low gain normalized output voltage, $V_{ON} = 0.75$, the output current monotonically increases as the normalized operating frequency is reduced. As the voltage gain increases to $V_{ON} = 1.0$ and 1.25 the low frequency output current decreases. At the current-source frequency, $\omega_{CN} = 2$, the output current is constant irrespective of the output voltage. It can be seen from the curves that the frequency range decreases as the voltage gain increases. Thus the higher the output voltage, the smaller the modulating frequency range and the lower the full-load current available.

Plots of the significant normalized converter rms currents are shown in Fig. 3-6. These are the rms currents in the rectifier, I_{RN}, the series tank, I_{SN}, the transistor, I_{QN},

the parallel branch, I_{PN}, the parallel capacitor, I_{CpN}, and the parallel inductance, I_{LpN}. This diagram can be used to extract important design information concerning converter operation. At the natural frequency of the parallel tank, $\omega_N = 1$, the converter has no voltage gain and thus the dc output current and consequently the rectifier current, I_{RN}, are zero. At $\omega_N = 1$, the rms currents, I_{CpN} in the parallel capacitor and I_{LpN} in the parallel inductance, are equal and opposite and the net current in the parallel branch, I_{PN}, is zero. As the frequency is increased, I_{LpN} decreases and I_{CpN} increases. At $\omega_N = 1.5$, I_{RN} is at its peak value of 1.6. As the frequency increases beyond $\omega_N = 1.5$, I_{RN} decreases. However, I_{CpN} is increasing which causes both I_{PN} and I_{SN} to increase. This topological characteristic that I_{SN} can increase for decreasing load current is a significant negative feature of the topology as the converter losses are closely related to I_{SN}. However, the transistor current, I_{QN} does not follow I_{SN}. It peaks at $\omega_N = 2$ and then starts to decrease because of the reduced conduction angle of the transistor.

As a first approximation, the converter can be designed using this simplified analysis to operate in a frequency range around the current-source point where the charging current is determined solely by the dc input voltage and is independent of the output voltage at that frequency. Plots of I_{ON} for various values of ω_{CN} and a constant output voltage are shown in Fig. 3-7. The plots show that if the current-source frequency is increased while the other variables are held constant then the power throughput of the converter increases. However, the frequency range also increases which may be disadvantageous in a practical design.

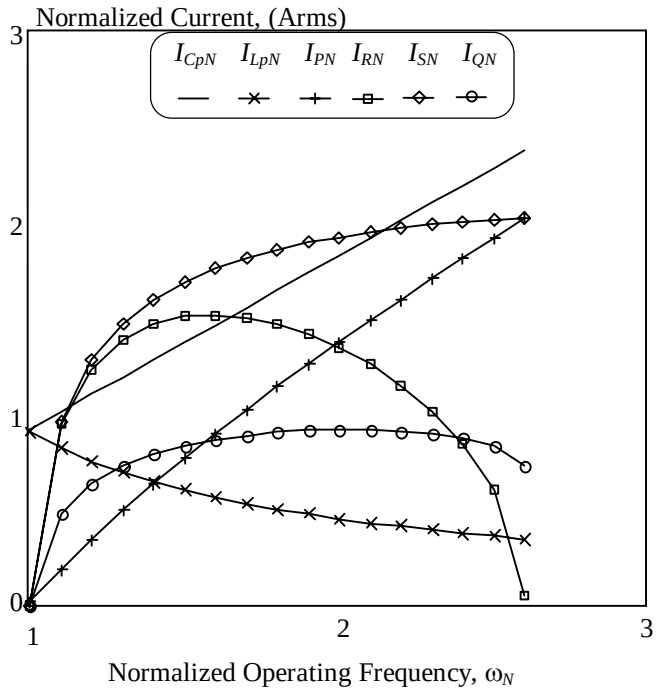

Fig. 3-6. Plot of normalized currents as a function of normalized operating frequency, ω_N, at V_{ON} = 1, ω_{OSN} = 0.5 and ω_{CN} = 2.

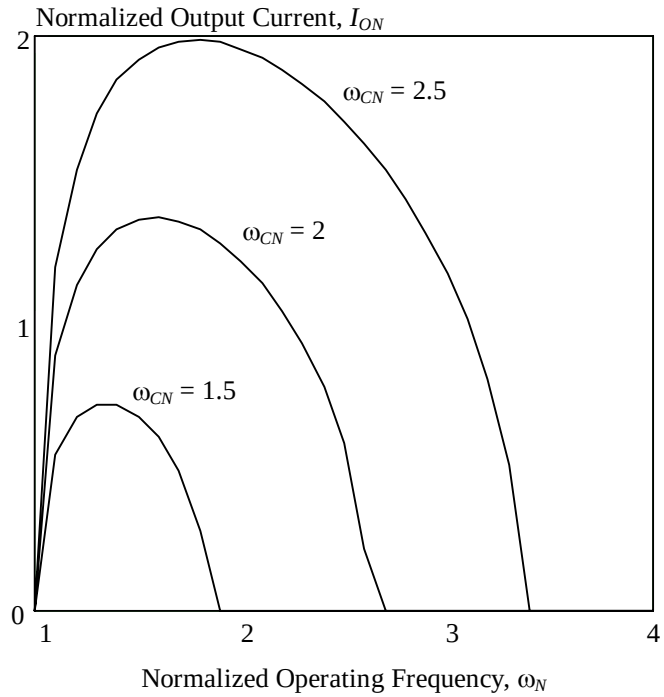

Fig. 3-7. Plot of normalized output current, I_{ON}, as a function of normalized operating frequency, ω_N, for various values of ω_{CN} at ω_{OSN} = 0.5 and V_{ON} = 1.

3.2.7 Error Analysis

In order to quantify the error in the basic FMA Analysis, the converter operating characteristics predicted by FMA Analysis are compared with those predicted by the ideal Modal Analysis. Experimental data is also available for the following parameter set and so these values will be used for the comparison.

$$V_I = 200 \text{ V}$$
$$f_{OS} = 27 \text{ kHz}$$
$$f_{OP} = 119 \text{ kHz}$$
$$f_C = 185 \text{ kHz}$$
$$Y_{OP} = 0.03 \text{ S}$$
$$n_P = 4$$
$$n_S = 4$$

Plots of theoretical dc output current versus frequency are shown in Fig. 3-8 and Fig. 3-9 for output voltages of 150V and 250V, respectively. The data for these plots are shown in Table 3-1. Modal Analysis shows that the frequency range for zero-voltage switching (ZVS) is greater that the range predicted by the FMA Analysis. The full range for ZVS is given in the table. The minimum frequency for ZVS at V_O = 150V is 30 kHz and is just above the series resonant frequency. However, the minimum frequency for ZVS for V_O = 250V is only 130 kHz because of the lack of voltage gain when the frequency approaches the parallel resonant frequency, 119 kHz.

The plots and the table show that significant errors exist between the FMA and Modal Analyses. There are crossover frequencies at approximately 160 kHz in both diagrams where the error goes to zero. However, the error can increase to 100% as the frequency decreases and the load current increases. The very significant errors in this simple FMA Analysis can be reduced by employing the more accurate RCFMA Analysis, which is discussed in the next section.

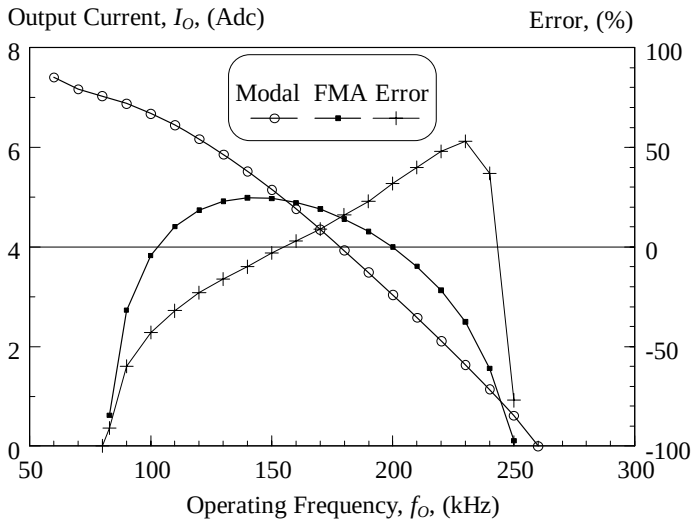

Fig. 3-8. Modal and FMA Analysis output currents and analytical error versus operating frequency at V_o = 150V.

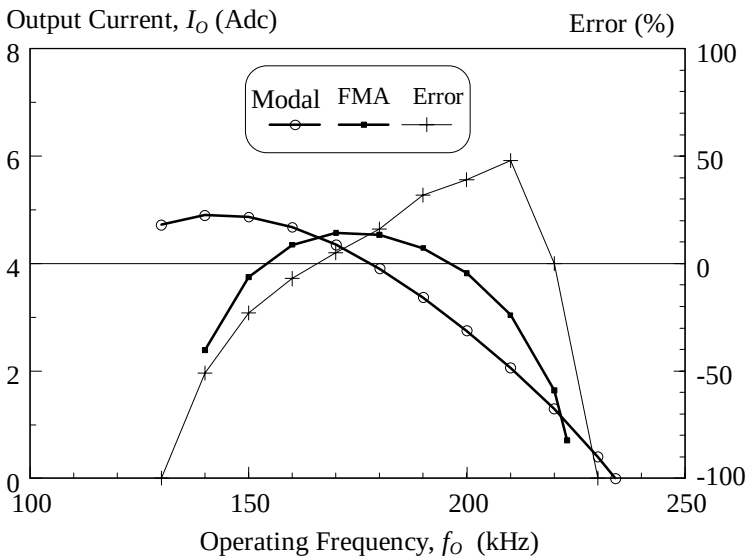

Fig. 3-9. Modal and FMA Analysis output currents and analytical error versus operating frequency at V_o = 250V.

Table 3-1

Modal and FMA Analysis output currents and analytical errors versus operating frequency for V_o = 150V and V_o = 250V.

V_O = 150V				V_O = 250V			
f_o (kHz)	Modal (A)	FMA (A)	Error (%)	f_o (kHz)	Modal (A)	FMA (A)	Error (%)
30	81.3	0	-100	130	4.72	0	-100
50	8.25	0	-100	140	4.9	2.39	-51
70	7.17	0	-100	150	4.87	3.75	-23
90	6.88	2.73	-60	160	4.68	4.35	-7
110	6.17	4.41	-32	170	4.35	4.57	5
130	5.86	4.92	-16	180	3.91	4.54	16
150	5.15	4.97	-3	190	3.37	4.29	32
170	4.35	4.76	9	200	2.75	3.82	39
190	3.49	4.31	23	210	2.06	3.04	48
210	2.48	3.61	40	220	1.3	1.64	0
230	1.63	2.5	53	230	0.4	0	-100
250	0.61	0.14	-71				

3.3 Rectifier-Compensated Fundamental Mode Approximation Analysis

Referring to the basic phasor voltage equation (3-28) repeated below, it can be seen that the equation is specified in terms of the rms voltages and currents and their respective phase angles.

$$V_{Irms}\angle\delta_I = \left\{1 - n^2 Z_S(\omega) Y_P(\omega)\right\} n V_{Rrms}\angle\delta_V + jZ_S(\omega) I_{Rrms} / n\angle\delta_A \qquad (3\text{-}48)$$

The circuit waveforms generated in Chapter Two show that the rectifier voltage in practice has a clamped quasi-sinusoidal wave shape, as shown in Fig. 2-2 and Fig. 2-3 for Trajectories 1 and 2, respectively. The basic assumption of the FMA Analysis theory that the rectifier voltage can be approximated by a square wave does not strictly apply, and furthermore, it varies over the load range. Thus, more accurate estimations of the rms voltage and phase angle must be derived in order to enhance the accuracy of the FMA Analysis. Similarly, improved estimations of the rms value and the phase angle of the rectifier current are also required.

The basic FMA Analysis equation (3-48) can be rewritten as

$$\frac{2\sqrt{2}}{\pi} V_I\angle\delta_I = \left\{1 - Z_S(\omega) Y_P(\omega) / n^2\right\} K_V n V_O\angle\delta_V + jZ_S(\omega) K_A I_O / n\angle\delta_A \qquad (3\text{-}49)$$

where K_V and K_A are factors directly relating the rms values to the dc amplitudes of the output voltage and current, respectively. These conversion factors are defined as:

$$K_V = \frac{V_{Rrms}}{V_O} \tag{3-50}$$

and

$$K_A = \frac{I_{Rrms}}{I_O} \tag{3-51}$$

The next step in the RCFMA Analysis is to generate expressions for the factors K_V and K_A and the phase angles δ_V and δ_A. As demonstrated in Chapter Two, an accurate estimation of these rms factors and phase angles for the four-element topology is mathematically complex and not of closed form. However, the estimation is simplified in the RCFMA Analysis by using an approximate equivalent two-element LC converter instead of the four-element LCLC converter. The rms values and phase angles derived from the two-element circuit are then used in the basic four-element FMA Analysis equation (3-49) to yield a more accurate calculation. RCFMA Analysis is not as precise as Modal Analysis but provides a relatively simple, accurate and intuitive, closed-form solution.

3.3.1 RMS and Phase Angle Relationships

RCFMA Analysis uses the following assumptions about the topology.

1. The four-element topology can be approximated by a two-element parallel resonant LC tank, as shown in Fig. 3-10. This can be seen as a valid approximation because of the following two circuit attributes. Firstly, the series tank must be inductive to maintain ZVS and will not become capacitive within the operating range. The role of the series capacitance, C_S, is secondary to that of the series inductance, L_S. Thus, the capacitance, C_S, is neglected in deriving the estimations but is later included in the FMA Analysis circuit equation. Secondly, the parallel branch is capacitive over the operating frequency range where voltage gain is required. The most significant component in the parallel branch is the capacitance, C_P, and the magnetizing inductance, L_P, plays a secondary role. Thus, the inductance, L_P, is neglected in

deriving the estimations but is again later included in the FMA Analysis circuit equation.

2. The converter operates with continuous conduction in the series inductor.
3. The current in the series inductor is approximated by its first harmonic.
4. The resonant frequency of the parallel resonant tank is assumed to be the current-source frequency, ω_C, of the four-element topology and not the natural frequency of L_S and C_P. This assumption generalizes and simplifies the derivation of the estimations and achieves relatively accurate results.
5. Trajectory 1 estimations will be used over the full load range. This greatly simplifies the derivation and avoids the transcendental solutions required if similar estimations are also used for Trajectory 2.

The equivalent circuit used for estimation of the rms values and phase angles in the RCFMA Analysis is shown in Fig. 3-10. The resonant tank consists of two elements, a series inductor, L_C, and a parallel capacitor, C_C. These two elements have a resonant frequency at the current-source frequency, ω_C, of the four element tank. The specific values of L_C and C_C are not necessarily the same as the original L_S and C_P.

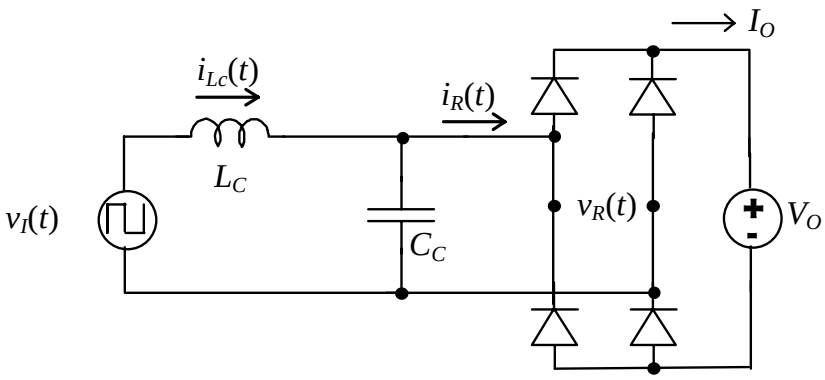

Fig. 3-10. RCFMA Analysis equivalent simplified two-element resonant circuit.

The waveforms for the two-element topology are shown in Fig. 3-11. The actual current is $i_{Lc}(t)$ while its first harmonic (slightly reduced in the figure for clarity) is $i_{Lc,1}(t)$.

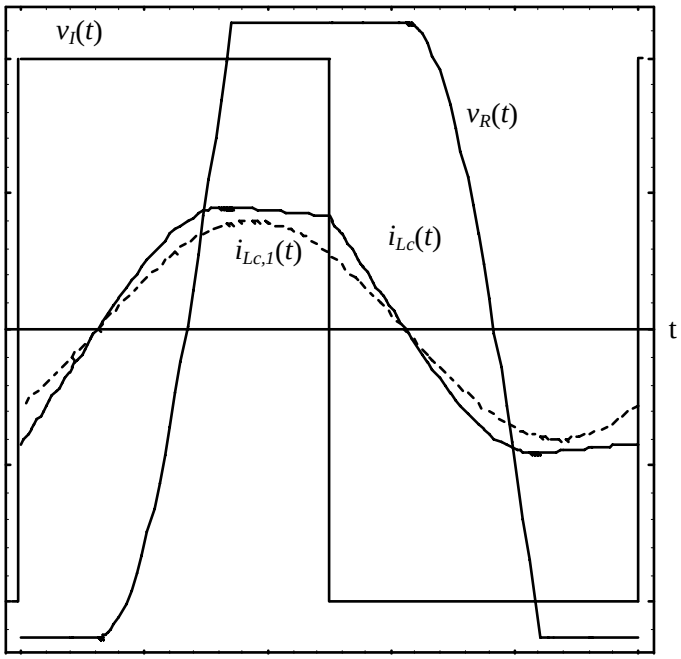

Fig. 3-11. Equivalent two-element resonant circuit waveforms.

In Trajectory 1, the rectifier voltage across capacitor C_C is completely charged or discharged by the current in L_C during the first or second half cycle, as illustrated in Fig. 2-2. In Trajectory 2, the charge or discharge begins in one half cycle and finishes in the next half cycle, as illustrated in Fig. 2-3. Clearly, it is easier to derive a simple expression for the rectifier voltage swing angle, which is critical for the analysis, for Trajectory 1 than for Trajectory 2. This is due to the fact that Trajectory 1 has only one tri-state interval while Trajectory 2 has two tri-state intervals whose unique solution must be found by solving a transcendental equation.

The rectifier voltage and current and their respective fundamental components are shown in Fig. 3-12 for Trajectory 1. The current into the rectifier, $i_R(t)$, is the segment of the sine-wave inductor current, $i_{Lc,1}(t)$, between t_3 and $T_O/2$. The circuit operates as follows. The current $i_{Lc,1}(t)$ goes to zero at t_0. At this time instant, the rectifier commutates and charging of C_C by $i_{Lc,1}(t)$ begins. The capacitor is completely charged over the angle γ, or by time instant t_3. Thus, reasonable accurate estimations of the fundamental components of the rectifier voltage and current can be

determined if angle γ is known since δ_V and δ_A, as well as K_V and K_A, depend on this parameter. The zero-crossing of the current $i_{Lc,1}(t)$ is selected as the zero phase reference. Thus, the phase angles of the first harmonics of the rectifier voltage and current, δ_V and δ_A, are specified with respect to the zero crossing of $i_{Lc,1}(t)$.

The waveforms $i_R(t)$ and $v_R(t)$ are periodic waveforms and so the rms values and phase angles of their first harmonics can be determined using standard Fourier Series analysis. The Fourier Series expressions for of the waveforms can be easily determined for Trajectory 1 when the phase angle γ is defined.

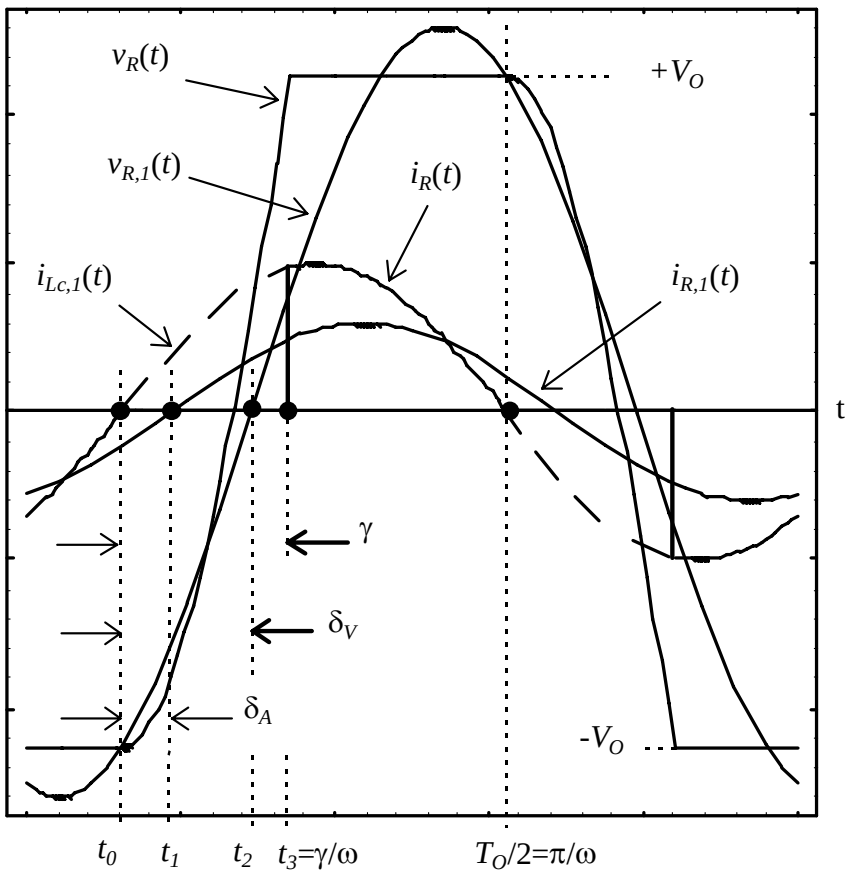

Fig. 3-12. Waveforms for $v_R(t)$ and $i_R(t)$ and their first harmonics for the two-element model.

From the theory of second-order resonant circuits the swing equation governing the capacitor voltage is

$$v_R(t) = Z_C I_{Lc,1}(t_0)\sin\left[\omega_C(t-t_0)\right] + \left[v_R(t_0) - V_I\right]\cos\left[\omega_C(t-t_0)\right] + V_I \qquad (3\text{-}52)$$

where Z_C is the characteristic impedance of L_C and C_C and equals $\sqrt{L_C / C_C}$.

As can be seen from Fig. 3-11, the initial value for $i_{Lc,1}(t)$ is zero at t_0 while the initial voltage on C_C is $-V_O$ and the input voltage is $+ V_I$. The capacitor is charged to

$+V_o$ over the time interval t_o to t_3, or angle γ to $+V_o$. Thus, the angle γ is given by the solution of

$$V_O = \left(-V_O - V_I\right)\cos\omega_C t_{0-3} + V_I \tag{3-53}$$

or using normalized quantities,

$$t_{0-3} = \frac{1}{\omega_C}\cos^{-1}\left(\frac{1-V_{ON}}{1+V_{ON}}\right) \tag{3-54}$$

and

$$\gamma = \omega t_{0-3} = \frac{\omega}{\omega_C}\cos^{-1}\left(\frac{1-V_{ON}}{1+V_{ON}}\right) \tag{3-55}$$

Now that a simple expression for γ has been obtained, the Fourier series co-efficient of the fundamental components of the rectifier voltage and current can be determined.

The Fourier series of a periodic function $f(t)$ of period T_o is defined by:

$$f\left(t\right) = a_0 + \sum_{n=1}^{\infty}\left(a_n \cos n\omega t + b_n \sin n\omega t\right) \tag{3-56}$$

For the fundamental components the Fourier co-efficients a_1 and b_1 are defined by:

$$a_1 = \frac{2}{T_O}\int_{-T_0/2}^{+T_0/2} f\left(t\right)\cos\omega t\, dt \tag{3-57}$$

and

$$b_1 = \frac{2}{T_O}\int_{-T_0/2}^{+T_0/2} f\left(t\right)\sin\omega t\, dt \tag{3-58}$$

The rms value, f_{1rms}, of $f_1(t)$, the first harmonic of $f(t)$ is given by:

$$f_{1rms} = \sqrt{\frac{a_1^{\,2} + b_1^{\,2}}{2}} \tag{3-59}$$

The phase angle of $f_1(t)$, δ, is given by:

$$\delta = \tan^{-1}\left(\frac{a_1}{b_1}\right) \tag{3-60}$$

The fundamental component of the rectifier current is derived first. The Fourier co-efficients are designated A_{A1} and B_{A1}. Thus, given the half-wave symmetry of the current waveforms, A_{A1} is defined by

$$A_{A1} = \frac{2\omega}{\pi}\int_0^{\pi/\omega} i_R\left(t\right)\cos\omega t\, dt \tag{3-61}$$

The rectifier current, $i_R(t)$, is defined by the series tank current, $i_{Lc}(t)$, during the interval that the rectifier conducts. The current $i_{Lc}(t)$ is defined as:

$$i_{Lc,1}\left(t\right) = I_{Lc,1}\sin\omega_C t \tag{3-62}$$

where $I_{Lc,1}$ is the peak value.

Substituting for $i_R(t)$ in (3-61) with the approximate rectifier conduction time gives

$$A_{A1} = \frac{2\omega}{\pi}\int_{\gamma/\omega}^{\pi/\omega} I_{Lc,1}\sin\omega t\cos\omega t\,dt \tag{3-63}$$

which can be integrated to give

$$A_{A1} = \frac{\omega}{\pi} I_{Lc,1}\left[\frac{-\cos 2\omega t}{2\omega}\right]_{\gamma/\omega}^{\pi/\omega} \tag{3-64}$$

or

$$A_{A1} = \frac{1}{2\pi} I_{Lc,1}\left(\cos 2\gamma - 1\right) \tag{3-65}$$

Similarly, Fourier co-efficient B_{A1} can be determined by

$$B_{A1} = \frac{2\omega}{\pi}\int_{0}^{\pi/\omega} i_R(t)\sin\omega t\,dt \tag{3-66}$$

or

$$B_{A1} = \frac{2\omega}{\pi}\int_{\gamma/\omega}^{\pi/\omega} I_{Lc,1}\sin\omega t\sin\omega t\,dt \tag{3-67}$$

Integrate to give

$$B_{A1} = \frac{\omega}{\pi} I_{Lc,1}\left[t - \frac{\sin 2\omega t}{2\omega}\right]_{\gamma/\omega}^{\pi/\omega} \tag{3-68}$$

or

$$B_{A1} = \frac{1}{\pi} I_{Lc,1}\left(\pi - \gamma + \frac{\sin 2\gamma}{2}\right) \tag{3-69}$$

The rms value of the fundamental component of the rectifier current can now be determined:

$$I_{Rrms} = \sqrt{\frac{A_{A1}{}^2 + B_{A1}{}^2}{2}} \tag{3-70}$$

or

$$I_{Rrms} = \frac{I_{Lc,1}}{\pi}\sqrt{\frac{1}{8}\left(\cos 2\gamma - 1\right)^2 + \frac{1}{2}\left(\pi - \gamma + \frac{\sin 2\gamma}{2}\right)^2} \tag{3-71}$$

The phase angle of the fundamental component of the rectifier current can also be determined from:

$$\delta_A = \tan^{-1}\left(\frac{A_{A1}}{B_{A1}}\right) \tag{3-72}$$

or

$$\delta_A = \tan^{-1}\left(\frac{\frac{1}{\sqrt{2}\pi} I_{Lc,1}\left(\cos 2\gamma - 1\right)}{\frac{1}{\pi} I_{Lc,1}\left(\pi - \gamma + \frac{\sin 2\gamma}{2}\right)}\right) \tag{3-73}$$

which can be simplified to

$$\delta_A = \tan^{-1}\left(\frac{\cos 2\gamma - 1}{2\pi - 2\gamma + \sin 2\gamma}\right) \tag{3-74}$$

The half-cycle average value of the rectifier current, which is also the dc current supplied to the battery, I_o, can be more easily derived as

$$I_O = \frac{\omega}{\pi}\int_0^{\pi/\omega} i_R(t)dt \tag{3-75}$$

or

$$I_O = \frac{\omega}{\pi}\int_{\gamma/\omega}^{\pi/\omega} I_{Lc,1}\sin\omega t\, dt \tag{3-76}$$

Performing this integration gives

$$I_O = \frac{\omega}{\pi} I_{Lc,1}\left[\frac{-\cos\omega t}{\omega}\right]_{\gamma/\omega}^{\pi/\omega} \tag{3-77}$$

or finally,

$$I_O = \frac{1}{\pi} I_{Lc,1}(1+\cos\gamma) \tag{3-78}$$

The relationship between the rms and average components of the rectifier current, K_A, can now be determined.

$$K_A = \frac{\frac{I_{Lc,1}}{\pi}\sqrt{\frac{1}{8}(\cos 2\gamma - 1)^2 + \frac{1}{2}\left(\pi - \gamma + \frac{\sin 2\gamma}{2}\right)^2}}{\frac{I_{Lc,1}}{\pi}(1+\cos\gamma)} \tag{3-79}$$

which can be simplified to

$$K_A = \frac{\sqrt{\frac{1}{8}(\cos 2\gamma - 1)^2 + \frac{1}{2}\left(\pi - \gamma + \frac{1}{2}\sin 2\gamma\right)^2}}{1+\cos\gamma} \tag{3-80}$$

The rms value and phase angle of the rectifier voltage can also be determined using Fourier series. The derivation of these equations is slightly more complex because of the clamped resonant nature of the voltage waveform. From Fig. 3-12 it can be seen that the waveform has two distinct sections. From t_0 to t_3, the rectifier voltage is the voltage across the parallel capacitor, C_C, which is charged in a resonant manner by the input voltage, V_I. From t_3 to $T_o/2$, the rectifier voltage is clamped at the output voltage. Thus the rectifier voltage is defined from t_0 to t_3 as

$$v_R(t) = (-V_O - V_I)\cos\omega_C t + V_I \tag{3-81}$$

and from t_3 to $T_o/2$ as

$$v_R(t) = +V_O \tag{3-82}$$

The waveform is obviously half-wave symmetric. The Fourier coefficients of the fundamental of the rectifier voltage, A_{V1} and B_{V1}, can now be derived using the half-wave symmetry property

$$A_{V1} = \frac{2\omega}{\pi}\int_0^{\pi/\omega} v_R(t)\cos\omega t\,dt \tag{3-83}$$

or $$A_{V1} = \frac{2\omega}{\pi}\int_0^{\gamma/\omega}\left[(-V_O - V_I)\cos\omega_C t + V_I\right]\cos\omega t\,dt + \frac{2\omega}{\pi}\int_{\gamma/\omega}^{\pi/\omega} V_O\cos\omega t\,dt \tag{3-84}$$

Hence,

$$\begin{aligned} A_{V1} = &-\frac{2\omega}{\pi}(V_I + V_O)\int_0^{\gamma/\omega}\cos\omega_C t\cos\omega t\,dt \\ &+\frac{2\omega}{\pi}V_I\int_0^{\gamma/\omega}\cos\omega t\,dt + \frac{2\omega}{\pi}V_O\int_{\gamma/\omega}^{\pi/\omega}\cos\omega t\,dt \end{aligned} \tag{3-85}$$

which is integrated to give

$$\begin{aligned} A_{V1} = &-\frac{\omega}{\pi}(V_I + V_O)\left[\frac{\sin(\omega+\omega_C)t}{(\omega+\omega_C)} + \frac{\sin(\omega-\omega_C)t}{(\omega-\omega_C)}\right]_0^{\gamma/\omega} \\ &+\frac{2\omega}{\pi}V_I\left[\frac{\sin\omega t}{\omega}\right]_0^{\gamma/\omega} + \frac{2\omega}{\pi}V_O\left[\frac{\sin\omega t}{\omega}\right]_{\gamma/\omega}^{\pi/\omega} \end{aligned} \tag{3-86}$$

or

$$A_{V1} = -\frac{\omega}{\pi}(V_I + V_O)\left[\frac{\sin(1+\omega_C/\omega)\gamma}{(\omega+\omega_C)} + \frac{\sin(1-\omega_C/\omega)\gamma}{(\omega-\omega_C)}\right] + \frac{2}{\pi}(V_I - V_O)\sin\gamma \tag{3-87}$$

Similarly, Fourier co-efficient B_{V1} can be determined.

$$B_{V1} = \frac{2\omega}{\pi}\int_0^{\pi/\omega} v_R(t)\sin\omega t\,dt \tag{3-88}$$

$$\therefore\ B_{V1} = \frac{2\omega}{\pi}\int_0^{\gamma/\omega}\left[(-V_O - V_I)\cos\omega_C t + V_I\right]\sin\omega t\,dt + \frac{2\omega}{\pi}\int_{\gamma/\omega}^{\pi/\omega} V_O\sin\omega t\,dt \tag{3-89}$$

$$B_{V1} = -\frac{2\omega}{\pi}(V_I + V_O)\int_0^{\gamma/\omega}\cos\omega_C t\sin\omega t\,dt + \frac{2\omega}{\pi}V_I\int_0^{\gamma/\omega}\sin\omega t\,dt + \frac{2\omega}{\pi}V_O\int_{\gamma/\omega}^{\pi/\omega}\sin\omega t\,dt \tag{3-90}$$

Integrate to give

$$\begin{aligned} B_{V1} = &\frac{\omega}{\pi}(V_I + V_O)\left[\frac{\cos(\omega+\omega_C)t}{(\omega+\omega_C)} - \frac{\cos(\omega-\omega_C)t}{(\omega-\omega_C)}\right]_0^{\gamma/\omega} + \\ &\frac{2\omega}{\pi}V_I\left[\frac{-\cos\omega t}{\omega}\right]_0^{\gamma/\omega} + \frac{2\omega}{\pi}V_O\left[\frac{-\cos\omega t}{\omega}\right]_{\gamma/\omega}^{\pi/\omega} \end{aligned} \tag{3-91}$$

or

$$B_{V1} = -\frac{\omega}{\pi}(V_I + V_O)\left[\frac{1-\cos(1+\omega_C/\omega)\gamma}{(\omega+\omega_C)} + \frac{1-\cos(1-\omega_C/\omega)\gamma}{(\omega-\omega_C)} - \frac{2}{\omega}\right] - \frac{2}{\pi}(V_I - V_O)\cos\gamma \tag{3-92}$$

The rms value of the fundamental component of the rectifier voltage can now be determined from

$$V_{Rrms} = \sqrt{\frac{A_{V1}{}^2 + B_{V1}{}^2}{2}} \tag{3-93}$$

The phase angle of the fundamental of the rectifier voltage is given by

$$\delta_V = \tan^{-1}\left(\frac{A_{V1}}{B_{V1}}\right) \tag{3-94}$$

The ratio of the rms value of the fundamental of the rectifier voltage and the battery voltage can now be determined as

$$K_V = \frac{\sqrt{\left(A_{V1}{}^2 + B_{V1}{}^2\right)/2}}{V_O} \tag{3-95}$$

The validity of this expression for K_v can be demonstrated by plotting K_v as a function of frequency as shown in Fig. 3-13. At low frequencies, K_v tends to $\frac{2\sqrt{2}}{\pi}$, the rms voltage factor for a square wave. As frequency increases, K_v tends to $\frac{1}{\sqrt{2}}$, the rms voltage factor for a sine wave. The rectifier voltage is actually a sine wave at no-load since the output rectifier no longer conducts. Thus K_v, as derived, provides a good estimation of the rms voltage and will be used in future analysis along with K_A, δ_v and δ_A.

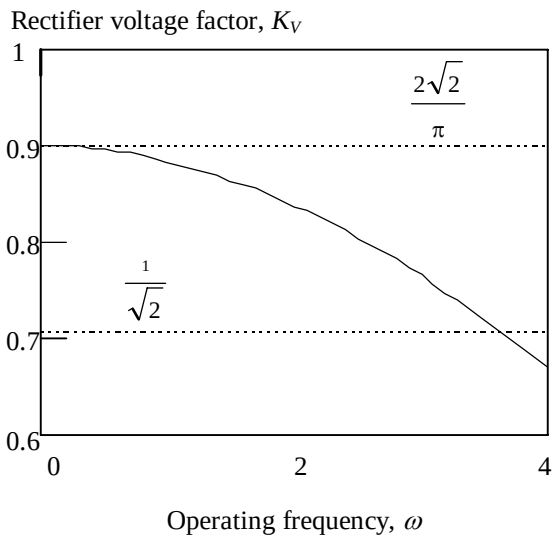

Fig. 3-13. Rectifier voltage factor, K_V, as a function of frequency, ω, at V_{ON} = 1 and ω_C = 2.

3.3.2 Circuit Equations

The earlier voltage equation (3-49) can be expanded in trigonometric notation as:

$$V_I(\cos\delta_I + j\sin\delta_I) = \{1 - Z_S(\omega)Y_P(\omega)/n^2\}\frac{\pi}{2\sqrt{2}}K_V nV_O(\cos\delta_V + j\sin\delta_V) + jZ_S(\omega)\frac{\pi}{2\sqrt{2}}K_A\frac{I_O}{n}(\cos\delta_A + j\sin\delta_A) \tag{3-96}$$

Equate the real and imaginary components of (3-96) to give

$$V_I\cos\delta_I = \{1 - Z_S(\omega)Y_P(\omega)/n^2\}\frac{\pi}{2\sqrt{2}}K_V nV_O\cos\delta_V - Z_S(\omega)n\frac{\pi}{2\sqrt{2}}K_A\frac{I_O}{n}\sin\delta_A \tag{3-97}$$

$$V_I\sin\delta_I = \{1 - Z_S(\omega)Y_P(\omega)/n^2\}\frac{\pi}{2\sqrt{2}}K_V nV_O\sin\delta_V + Z_S(\omega)\frac{\pi}{2\sqrt{2}}K_A\frac{I_O}{n}\cos\delta_A \tag{3-98}$$

Squaring both sides of the above two equations and adding the resulting equations gives the following result.

$$V_I^2 = \{1 - Z_S(\omega)Y_P(\omega)/n^2\}^2\left(\frac{\pi}{2\sqrt{2}}K_V\right)^2 n^2V_O^2 + \left(Z_S(\omega)\frac{\pi}{2\sqrt{2}}K_A\right)^2\frac{I_O^2}{n^2} + 2\{1 - Z_S(\omega)Y_P(\omega)/n^2\}Z_S(\omega)\frac{\pi^2}{8}K_V K_A\sin(\delta_V - \delta_A)V_O I_O \tag{3-99}$$

Equation (3-99) can be used to calculate or plot any single unknown for a given set of circuit parameters and to develop design characteristics for the converter. For example, the dc output current I_o can be determined if the input and output voltages

and the circuit parameters and operating frequency are known. The above equation can be expressed in terms of I_o as

$$0 = a(\omega) I_O^{\ 2} + b(\omega) I_O + c(\omega) \tag{3-100}$$

Thus, equation (3-100) can be solved for the dc output current I_o using the standard solution for a quadratic equation

$$I_O = \frac{-b(\omega) - \sqrt{b(\omega)^2 - 4a(\omega)c(\omega)}}{2a(\omega)} \tag{3-101}$$

When I_o is known, other critical circuit currents can be easily derived.

The rectifier voltage phasor is given by:

$$\mathbf{v_R} = K_V V_O \angle \delta_V \tag{3-102}$$

Hence, the currents in the parallel capacitor, $\mathbf{i_{Cp}}$, and in the parallel inductance, $\mathbf{i_{Lp}}$, are readily obtained:

$$\mathbf{i_{Cp}} = j \frac{\omega}{\omega_{OP}} Y_{OP} \mathbf{v_R} \tag{3-103}$$

and

$$\mathbf{i_{Lp}} = -j \frac{\omega_{OP}}{\omega} Y_{OP} \mathbf{v_R} \tag{3-104}$$

The current in the parallel tank, $\mathbf{i_P}$, is the sum of the above two currents:

$$\mathbf{i_P} = \mathbf{i_{Cp}} + \mathbf{i_{Lp}} \tag{3-105}$$

The rectifier current phasor is given by:

$$\mathbf{i_R} = K_A I_O \angle \delta_A \tag{3-106}$$

The series current is the sum of the rectifier and parallel currents:

$$\mathbf{i_S} = \mathbf{i_R} / n + \mathbf{i_P} / n \tag{3-107}$$

The phase angle, δ_s, of $\mathbf{i_S}$ is easily derived from the real and imaginary components:

$$\delta_S = \tan^{-1}\left(\mathrm{Im}ag(\mathbf{i_S}) / \mathrm{Re}al(\mathbf{i_S})\right) \tag{3-108}$$

The phase angle of the input voltage, δ_i, is given by (3-97) as

$$\delta_I = \cos^{-1}\left[\left\{1 - Z_S(\omega) Y_P(\omega) / n^2\right\} \frac{\pi}{2\sqrt{2}} K_V \frac{nV_O}{V_I} \cos\delta_V - Z_S(\omega) \frac{\pi}{2\sqrt{2}} K_A \frac{I_O}{nV_I} \sin\delta_A\right] \tag{3-109}$$

The power factor angle, δ_L , of the series current relative to the input voltage is then given by

$$\delta_L = \delta_I - \delta_S \tag{3-110}$$

As before, the current in the transistor is the main heat generating current in the bridge. This current is designated $i_Q(t)$ and is equal to the series current in each half cycle from δ_L to π. The rms current in each transistor I_{Qrms} is given by

$$I_{Qrms} = I_S \sqrt{\left[\pi - \delta_L - 0.5 \sin 2(\pi - \delta_L)\right] / 2\pi} \tag{3-111}$$

where I_s is the peak value of the series current.

The rms current in the rectifier can be more accurately calculated using the actual waveform, rather than the first harmonic. The rms current in the rectifier, I_{RCrms}, is therefore given by

$$I_{RCrms} = I_{Lc,1} \sqrt{\left[\pi - \gamma - 0.5 \sin 2(\pi - \gamma)\right] / 2\pi} \tag{3-112}$$

where $I_{Lc,1}$ is the peak value of the two-element model series current and γ is the rectifier voltage risetime.

3.3.3 Converter Characterization

The formulae just derived can now be used to characterize the converter. Plots of normalized current versus frequency are shown in Fig. 3-14.

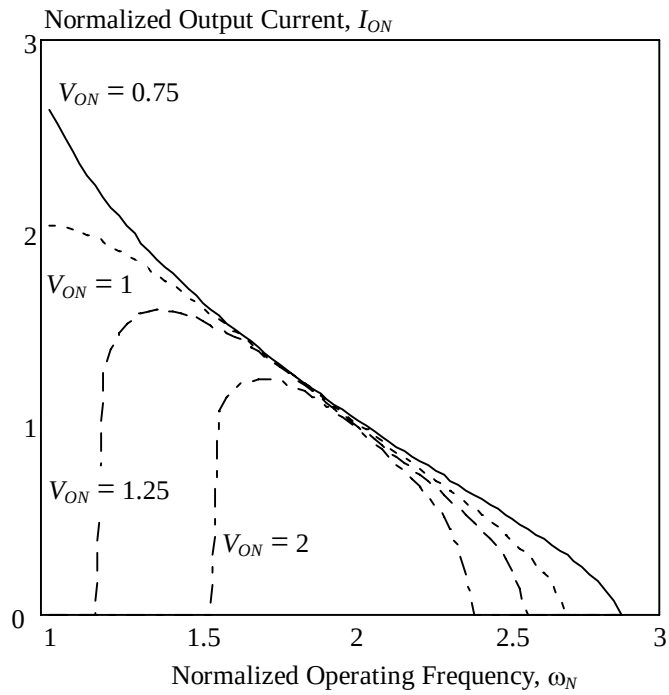

Fig. 3-14. Normalized output current, I_{ON}, as a function of normalized operating frequency, ω_N, for various values of V_{ON} for ω_{OSN} = 0.5 and ω_{CN} = 2.

These curves have similar characteristics to the FMA Analysis curves plotted in Fig. 3-5. As expected, the RCFMA Analysis output current curves have the same current-source characteristic at ω_N = 2 as the FMA Analysis curves. For both RCFMA and FMA Analyses the output current generally increases as frequency is decreased until a frequency is reached where the current gain is maximized. Below this frequency the output current decreases. The main differences between the curve sets are (1) the RCFMA Analysis plots have a more linear nature than the FMA Analysis curves over the load range, and (2) significantly larger currents are calculated at lower frequencies and higher voltages when RCFMA Analysis is used. For example, RCFMA Analysis predicts a normalized output current of 2.05 at ω_N = 1 compared to a value of zero predicted by the basic FMA Analysis. The error analysis in the next section will more fully illustrates the relative accuracies of the two methods of analysis.

The significant converter currents required for design purposes are shown in Fig. 3-15, as calculated using the RCFMA Analysis equations.

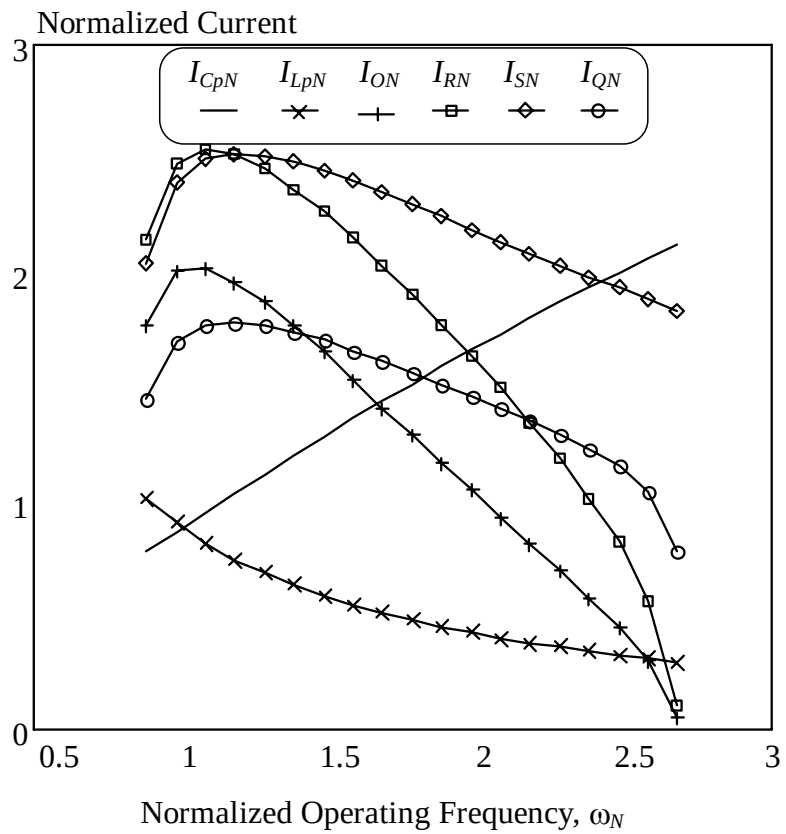

Fig. 3-15. Normalized currents, I_{CpN}, I_{LpN}, I_{ON}, I_{RN}, I_{SN} and I_{QN}, as a function of normalized operating frequency, ω_N, at V_{ON} = 1, ω_{OSN} = 0.5 and ω_{CN} = 2.

3.3.4 Error Analysis

A comparison of the dc output current predicted by the Modal and RCFMA Analyses are shown in Fig. 3-16 and Fig. 3-17, for dc output voltages of 150V and 250V, respectively, and for the same circuit parameters as previously used in the error analysis of the FMA Analysis. The relative error between the RCFMA Analysis and the Modal Analysis is also shown. The data for both sets of plots and the earlier FMA Analysis results are listed in Table 3-2. The input voltage is 200V and the output voltages of 150V and 250V therefore represent voltage gains of 0.75 and 1.25, respectively.

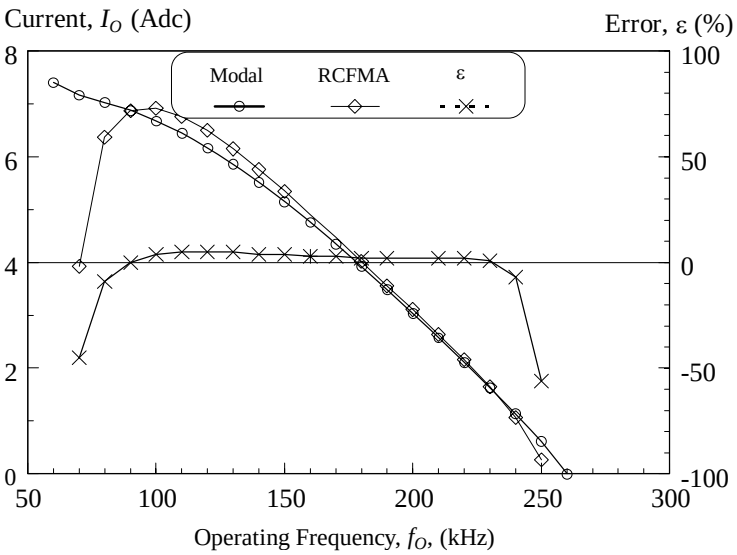

Fig. 3-16. Output current from RCFMA and Modal Analyses and relative error versus operating frequency for V_o = 150V.

The data and graphs show that the error has been reduced significantly over the full load range for both voltage levels using RCFMA Analysis rather than FMA Analysis. The output currents predicted by RCFMA Analysis closely track the ideal Modal Analysis currents predicted for a significant part of the load range. At 150V, the RCFMA Analysis error is less that 10% at 80kHz and typically has errors of less than 5% until it almost reaches zero load at 250 kHz. At 250 kHz the error seems high at 56% but the absolute error in terms of full-load current at 90 kHz is less than 2%. However, the RCFMA Analysis results deviate significantly from those generated by Modal Analysis below 80 kHz. The basic assumptions for RCFMA Analysis suggest that the analysis has greatest accuracy above the parallel resonant frequency when the tank is capacitive. However, the 150V results show that the

analysis remains valid at frequencies significantly below the parallel resonant frequency. The reason for this accuracy is that at low frequencies and output voltages, the parallel tank plays a smaller part in determining the magnitude of the output current than the series tank. Thus, the basic assumptions of RCFMA Analysis still maintain sufficient accuracy to generate useful results.

The RCFMA Analysis is based only on Trajectory 1 rms value and phase estimations. Trajectory 2 is neglected because of its significantly more complicated non-closed form solution. The data shown in italics at 230 kHz and 250 kHz in Table 3-2 are Trajectory 2 frequencies. The results indicate that the Trajectory 1 rms value and phase angle estimations are reasonable until the onset of no-load and that the more complex Trajectory 2 estimations are not really necessary from the point of view of accuracy.

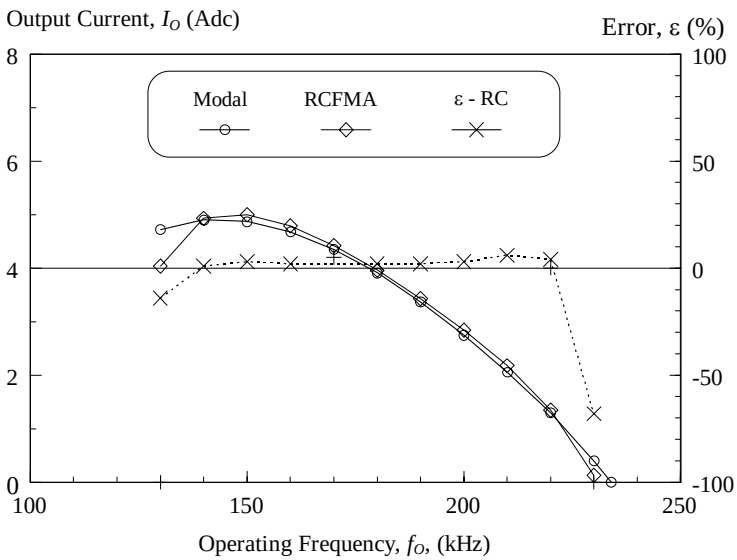

Fig. 3-17. Output current from RCFMA and Modal Analyses and relative error versus operating frequency for V_o = 250V.

Similar results are obtained at 250V as illustrated in Fig. 3-17. The error is typically under 5% from no-load to full-load. At 250V, the converter is always operating in a voltage boost mode. Thus, the frequency range for ZVS lies above the parallel tank resonant frequency. The minimum frequency for ZVS is 130 kHz and the RCFMA Analysis error is only 14%. As the frequency increases the error decreases significantly and is typically less than the error at 150V by a couple of percent for the same frequency range. This improvement occurs because the basic RCFMA Analysis assumptions are more valid at higher output voltages when the

parallel branch is playing a more significant role in determining the relative current levels due to the higher output voltage. Again, the error associated with the Trajectory 2 components is relatively minor.

Table 3-2

Output current from RCFMA and Modal Analyses and relative error versus operating frequency for V_o = 150V and V_o = 250V.

V_O = 150V						**V_O = 250V**					
	I_O			**Error**			**I_O**			**Error**	
f_O (kHz)	**Modal (A)**	**RCFMA (A)**	**FMA (A)**	**RCFMA (%)**	**FMA (%)**	**f_O (kHz)**	**Modal (A)**	**RCFMA (A)**	**FMA (A)**	**RCFMA (%)**	**FMA (%)**
30	81.3	0	0	-100	-100	130	4.72	4.04	0	-14	-100
50	8.25	0	0	-100	-100	140	4.9	4.93	2.39	1	-51
70	7.17	3.93	0	-45	-100	150	4.87	5	3.75	3	-23
90	6.88	6.87	2.73	0	-60	160	4.68	4.79	4.35	2	-7
110	6.17	6.77	4.41	5	-32	170	4.35	4.42	4.57	2	5
130	5.86	6.15	4.92	5	-16	180	3.91	3.96	4.54	1	16
150	5.15	5.35	4.97	4	-3	190	3.37	3.43	4.29	2	32
170	4.35	4.47	4.76	3	9	200	2.75	2.84	3.82	3	39
190	3.49	3.56	4.31	2	23	210	2.06	2.18	3.04	6	48
210	2.48	2.64	3.61	2	40	*220*	*1.3*	*1.35*	*1.64*	*4*	*0*
230	*1.63*	*1.65*	*2.5*	*1*	*53*	*230*	*0.4*	*0.13*	*0*	*-68*	*-100*
250	*0.61*	*0.27*	*0.14*	*-56*	*-71*						

Other important converter currents calculated by the Modal and RCFMA Analyses will now be compared and discussed in this section. These currents are the rms currents in the rectifier, I_R, the series tank, I_s, the transistor, I_Q, the parallel capacitor, I_{Cp}, and the parallel inductance, I_{Lp}. The currents are plotted for V_o = 250V in Fig. 3-18, Fig. 3-19 and Fig. 3-20, respectively. The data are summarized in Table 3-3 and Table 3-4.

As already discussed, RCFMA Analysis calculates I_o to a high degree of accuracy, with a typical error of less than 5% over the load range. However, the tables show that the error in the rectifier current, I_R, increases from nearly zero at full-load to around 10% at medium load with the error increasing as load current decreases. This anomaly provides an interesting insight into the RCFMA analysis which is further illustrated by the other currents to be examined. Current, I_R, has a significant harmonic content which is not fully considered by RCFMA Analysis due to its emphasis on the fundamental component. However, the power transfer takes place largely in the fundamental mode, allowing I_o to be calculated quite accurately.

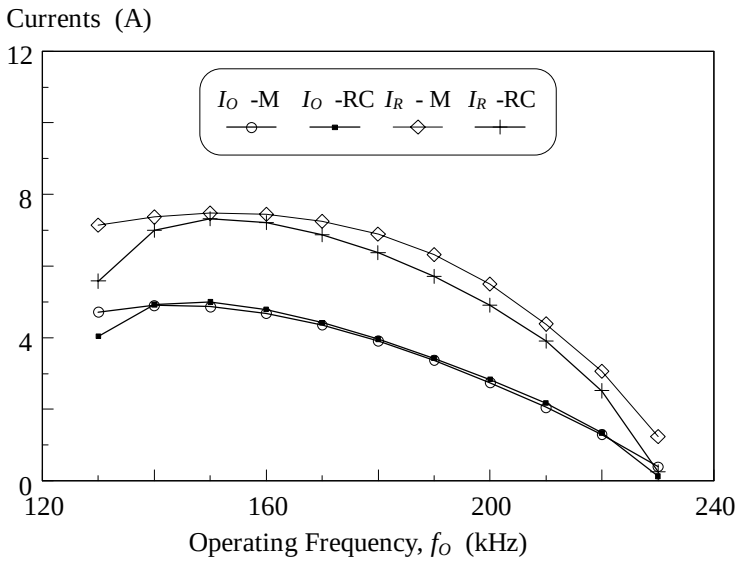

Fig. 3-18. Modal (M) and RCFMA (RC) Analyses output current, I_O, and rectifier current, I_R, versus operating frequency for V_O = 250V.

Similar results are obtained when I_s and I_Q are compared, as shown in Fig. 3-19. The error in I_s is very low over the load range, typically less than 5%, while I_Q typically has an error nearly twice that of I_s. The larger error in I_Q is due to its greater harmonic content, as in the case of I_R.

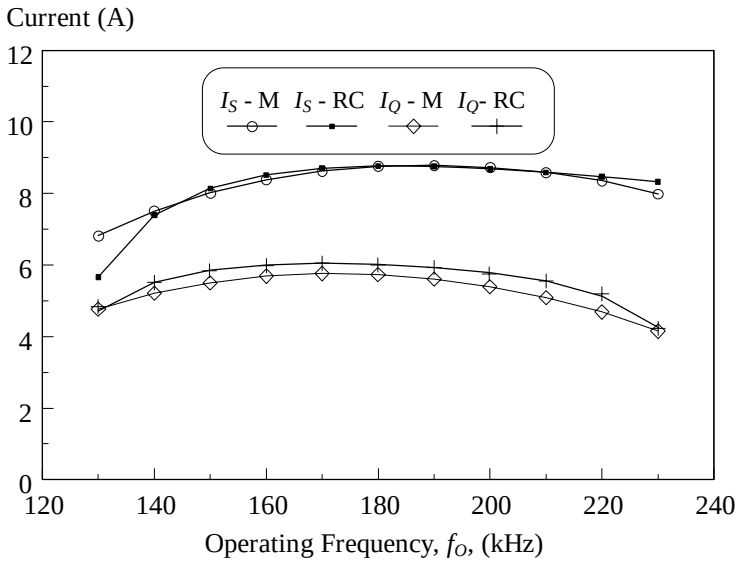

Fig. 3-19. Modal (M) and RCFMA (RC) Analyses series current, I_s, and transistor current, I_Q, versus operating frequency for V_O = 250V.

The plots for I_{Cp} and I_{Lp} are compared in Fig. 3-20. Clearly, RCFMA Analysis does not calculate I_{Cp} as accurately as I_{Lp}. Again, this is because of the phase-controlled sine wave nature of I_{Cp}, similar to that of I_R, with a high harmonic content.

The error in I_{Cp} reduces as the frequency increases because of the reduction in the harmonic content of I_{Cp}.

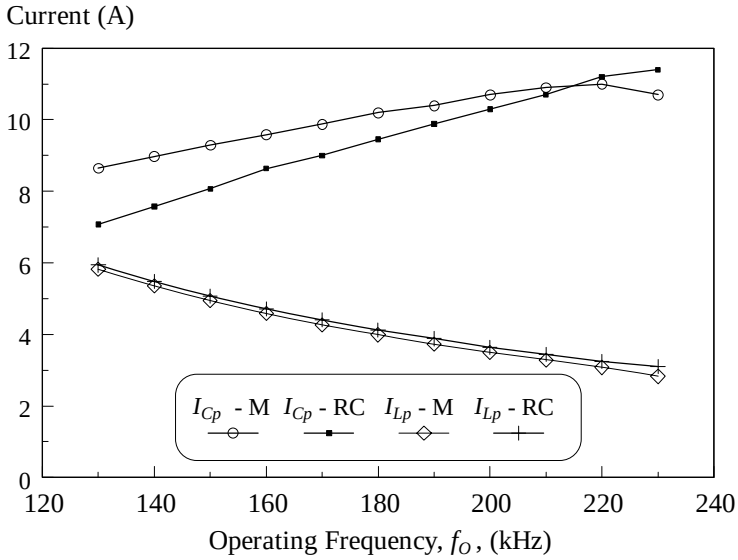

Fig. 3-20. Modal(M) and RCFMA(RC) Analyses parallel capacitor current, I_{Cp}, and parallel inductor current, I_{Lp}, versus operating frequency for V_O = 250V.

Table 3-3

Comparison of Modal and RCFMA Analyses currents and relative errors for V_O = 250V.

f_O (kHz)	I_O Modal (A)	I_O RCFMA (A)	I_O Error (%)	I_S Modal (A)	I_S RCFMA (A)	I_S Error (%)	I_{CP} Modal (A)	I_{CP} RCFMA (A)	I_{CP} Error (%)
130	4.72	4.04	-14	6.82	5.66	-17	8.65	7.08	-18
140	4.9	4.93	1	7.51	7.4	-1	8.98	7.58	-16
150	4.87	5	3	8.02	8.14	1	9.29	8.07	-13
160	4.68	4.79	2	8.39	8.52	2	9.59	8.64	-10
170	4.35	4.42	2	8.63	8.71	1	9.88	9	-9
180	3.91	3.96	1	8.76	8.77	0	10.2	9.45	-7
190	3.37	3.43	2	8.79	8.76	0	10.4	9.88	-5
200	2.75	2.84	3	8.73	8.69	0	10.7	10.3	-4
210	2.06	2.18	6	8.59	8.59	0	10.9	10.7	-2
220	*1.3*	*1.35*	*4*	8.36	8.47	1	11	11.2	2
230	*0.4*	*0.13*	*-68*	7.99	8.33	4	10.7	11.4	7

Table 3-4

Comparison of Modal and RCFMA Analyses currents and relative errors for V_O = 250V.

	I_R			I_Q			I_{LP}		
f_O (kHz)	**Modal (A)**	**RCFMA (A)**	**Error (%)**	**Modal (A)**	**RCFMA (A)**	**Error (%)**	**Modal (A)**	**RCFMA (A)**	**Error (%)**
130	7.15	5.58	-22	4.77	4	-16	5.82	5.94	2
140	7.37	7	-5	5.21	5.23	0	5.35	5.48	2
150	7.48	7.32	-2	5.51	5.75	4	4.95	5.08	3
160	7.45	7.22	-3	5.69	5.98	5	4.59	4.72	3
170	7.26	6.88	-5	5.76	6.05	5	4.27	4.41	3
180	6.89	6.37	-8	5.73	6	5	3.99	4.13	4
190	6.32	5.71	-10	5.61	5.87	5	3.73	3.88	4
200	5.5	4.91	-11	5.4	5.64	4	3.5	3.65	4
210	4.38	3.91	-11	5.09	5.28	4	3.29	3.44	5
220	*3.06*	*2.52*	*-18*	*4.69*	*4.64*	*-1*	*3.08*	*3.25*	*6*
230	*1.24*	*0.25*	*-80*	*4.15*	*3.28*	*-21*	*2.83*	*3.11*	*10*

3.4 DESIGN EXAMPLE

The RCFMA Analysis equation (3-99) is a closed-form equation that can be used to solve for the dc output current, I_o, for a given set of circuit inputs. This equation and the other closed-form expressions developed in the RCFMA Analysis are extremely useful in the design of a resonant converter. The practical value of the analysis can be illustrated by the following design example.

Design Assignment

The resonant converter for an inductive charger is to be designed to the following specifications. The SAE J-1773 compatible (defines f_{OP} and Y_{OP}) converter is powered from a 220V, 30A utility line which is power-factor-corrected to a dc link voltage of 385V. The converter must supply rated power to a Nickel Metal-Hydride battery pack with a peak dc voltage of 430V. Transformer core heating limits the minimum frequency of the converter to 175 kHz. The maximum frequency for no-load operation is 300 kHz. Maintain a unity transformer turns ratio.

Design Procedure

A Mathcad software design tool has been developed to design the converter. The closed-form equations from the RCFMA Analysis represented by equation (3-99) and its component expressions form the main body of the program, which can numerically solve for any unknown if sufficient conditions are input to the solver algorithm.

For the given design example, only two unknowns exist and two equations in terms of the two unknowns are easily constructed. The known inputs are V_I, V_O, f_{OP}, Y_{OP} and n. The unknowns are the series resonant and current-source frequencies, f_{OS} and f_C.

Two equations can easily be constructed in terms of f_{OS} and f_C using the output power conditions. Trivial solutions can be avoided by not requesting zero output power at the maximum frequency of 300 kHz. Instead, 10% of full power is requested at a slightly lower frequency.

Equation 1: P(175 kHz, f_{OS}, f_{OP}) = 6.6 kW

Equation 2: P(285 kHz, f_{OS}, f_{OP}) = 0.66 kW

The program successfully generates valid solutions for f_{OS} and f_C based on these power equations and the circuit inputs. The solutions are:

$$f_{OS} = 52 \text{ kHz}$$

and

$$f_C = 222 \text{ kHz},$$

from which L_S and C_S can be calculated.

The results can be verified by plotting output power as a function of frequency using the final converter parameter set for both the RCFMA and Modal Analyses. These plots, given in Fig. 3-21, show excellent correlation and illustrate the usefulness and accuracy of RCFMA Analysis for converter design.

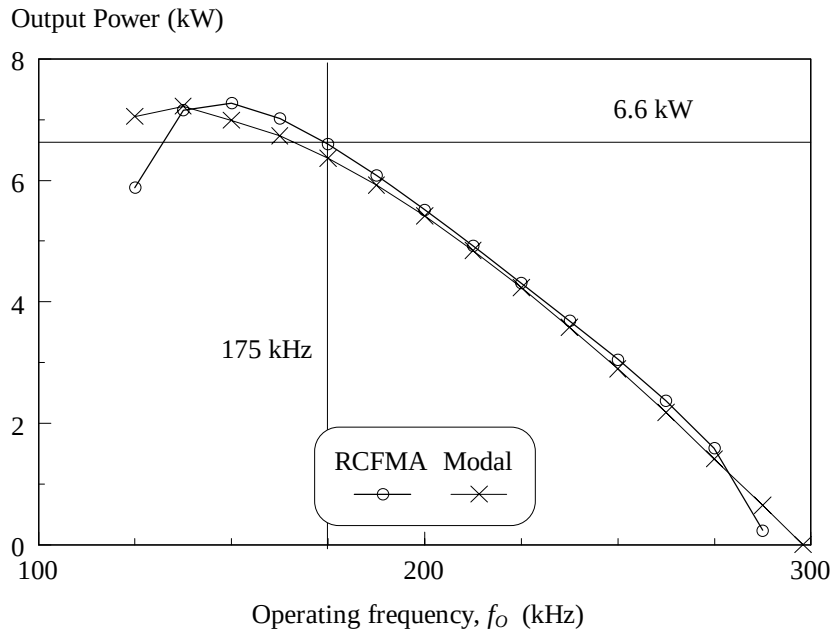

Fig. 3-21. Modal and RCFMA Analyses output power versus operating frequency for the design example.

3.5 CONCLUSIONS

In this chapter, the application of Fundamental Mode Approximation (FMA) Analysis to the four-element series-parallel LCLC resonant converter with capacitive output filter and voltage-source load was investigated. FMA Analysis equations were first derived for the topology. A comparison of the FMA and Modal Analyses showed that while the FMA Analysis provided a simple and intuitive design tool, the significant inaccuracies of the analysis limited its usefulness. A more in-depth understanding of the analytical technique and the specific application allows development of an extension to the basic FMA Analysis technique which is designated Rectifier-Compensated FMA (RCFMA) Analysis. It has been shown that the RCFMA Analysis is a relatively simple, but very accurate technique that provides a closed-form solution for the family of multi-element multi-resonant converters being studied. The key to the simplicity of RCFMA Analysis is the use of a simplified time-domain model to generate accurate approximations for the rms magnitudes and phase angles of the rectifier voltage and current. These approximations are then used to extend the accuracy of the basic FMA Analysis model. The RCFMA Analysis is discussed in detail and the results are compared with the more accurate but time intensive and mathematically complex Modal

Analysis, discussed in the previous chapter. Excellent correlation is demonstrated between the two analyses.

The successful development of the RCFMA Analysis can greatly simplify the inductive charger design procedure. The Modal Analysis does not provide a closed-form solution and requires an iterative approach to design optimization. However, it has been shown that the RCFMA Analysis can easily solve for any unknown circuit parameters when sufficient design information is provided.

REFERENCES

[1] J.G. Hayes, J.T. Hall, M.G. Egan, J.M.D. Murphy, "Full-Bridge, Series-Resonant Converter Supplying the SAE J-1773 Electric Vehicle Inductive Charging Interface," *IEEE Power Electronics Specialists Conf. Rec.*, 1996, pp. 1913- 1918.

[2] J.G. Hayes, S.E. Schulz, J.T. Hall, M.G. Egan, J.M.D. Murphy, "Wide Load Resonant Converter Supplying the SAE J-1773 Electric Vehicle Inductive Charging Interface," *IEEE Industrial Applications Society Conf. Rec.*, 1996, pp. 1065-1071.

[3] R.L. Steigerwald, "A Comparison of Half-Bridge Resonant Converter Topologies," *IEEE Trans. Power Electronics*, Vol. 3, No. 2, April 1988, pp. 174-182.

[4] R.L. Steigerwald, "Practical Design Methodologies for Load Resonant Converters Operating above Resonance," *IEEE Applied Power Electronics Conf. Rec.*, 1992, pp. 172-179.

[5] Y. Cheron, "Soft Commutation," Chapman and Hall, 1992.

[6] M. Kazamierczuk, M. Czarkowski, "Resonant Power Converters," John Wiley & Sons Inc., 1995.

[7] N. Kutkut, D.M. Divan, D.W. Novotny, R. Marion, "Design Considerations and Topology Selection for a 120kW IGBT Converter for EV Charging," *IEEE Power Electronics Specialists Conf. Rec.*, 1995, pp. 238-244.

[8] G. Ivensky, A. Kats, S. Ben-Yaakov, "A Novel RC Model of Capacitive-Loaded Parallel and Series-Parallel Resonant DC-DC Converters," *IEEE Power Electronics Specialists Conf. Rec.*, 1997, pp. 958-964.

4.

CHAPTER FOUR

APPLICATION OF PHASE CONTROL TO THE SERIES-PARALLEL LCLC RESONANT CONVERTER WITH CAPACITIVE OUTPUT FILTER AND VOLTAGE-SOURCE LOAD

Abstract: In earlier chapters, the study of the inductive coupling resonant converter application has focused on variable-frequency control. Phase control is an alternative approach for controlling the converter output power and in this chapter, the application of phase control to the series-parallel LCLC resonant converter with capacitive output filter is studied. The topology is investigated using Fundamental Mode Approximation (FMA) Analysis for initial characterization and Rectifier-Compensated FMA (RCFMA) Analysis for more detailed design information. The analyses identify areas of operation where it is advantageous to phase control the converter, leading to a novel hybrid control scheme which integrates variable frequency and phase control. This hybrid control technique reduces the required operating frequency range compared to that using frequency control alone. The reduced frequency range results in reduced passive component and gate-drive stresses and, in addition, achieves improved partial-load efficiency. The results of the analysis and the benefits of the new control scheme are validated by experimental results.

4.1. INTRODUCTION

Resonant power conversion has many advantages in the electric vehicle inductive coupling application. Use of a variable-frequency series-resonant inverter to drive the coupler and vehicle inlet has many desirable features, as discussed in Chapter Two.

The disadvantages of the frequency-controlled resonant converter are the relative inefficiency at light loads and the wide operating frequency range. The converter reduces output power by increasing the operating frequency, effectively shunting the load current to the parallel capacitor. Consequently, the resonant tank currents and associated power losses remain high over the load range resulting in

poor efficiency at light loads. This light-load efficiency is important as various battery technologies require long periods of charging at trickle current levels. In addition, the wide operating frequency range results in significant gate drive requirements and inefficient power component utilization, with high stresses at low loads and increased EMI source bandwidths.

To counter the disadvantages of frequency-controlled converters, various phase-controlled resonant converters have been proposed and studied [3-10]. Typical converters employing phase control utilize a series connected load and operate at a constant frequency, allowing optimization of power, gate drive and EMI suppression components [3-7]. Phase-controlled resonant converters can be designed to implement zero-voltage or zero-current switching. However, a major problem with phase-controlled resonant converters can be the loss of soft switching as the phase control angle is increased [3-7].

A family of phase-controlled resonant converters, soft-switched over the load range, has been presented, analyzed and discussed [8-10]. This family of converters utilizes a Class D or parallel-connected load and gives a high-efficiency phase-controlled converter compatible with SAE J-1773. This converter family is discussed and analyzed in detail in the next chapter.

In this chapter, the phase-controlled series-parallel resonant converter with capacitive output filter and voltage-source load will be analyzed in detail. Phase-controlled resonant converters have typically been analyzed in the time domain [3-5], or by using FMA Analysis [8-10], or by Fourier series methods [6]. The present study extends the application of FMA to the phase-controlled resonant converter family and, furthermore, employs the previously introduced RCFMA Analysis to give improved accuracy. The methodology will show that the phase control technique in general results in a loss of soft switching at low operating frequencies. However, above a certain critical frequency, the presence of the capacitive parallel branch allows the converter to be fully phase controlled to zero load over a limited frequency range while maintaining ZVS. Thus, a new control strategy which integrates frequency and phase control is proposed and is designated Hybrid Frequency and Phase Control (HFPC). In HFPC, the converter is frequency controlled at the high to medium power levels but for further reduction in power output, the frequency is clamped at a predefined maximum value and the converter

is subsequently phase controlled down to zero output power. This HFPC approach features all the benefits of frequency control but has a reduced operating frequency range, reduced gate drive requirements and improved light load efficiency compared to frequency control only.

The basic converter topology is discussed in Section 4.2. In Section 4.3, the converter is analyzed using FMA Analysis in order to predict the basic characteristics in a simple mathematical format. RCFMA Analysis is applied in Section 4.4 to generate more accurate analytical results. Section 4.5 compares the experimental and RCFMA data and validates the analysis and control approach.

4.2. Converter Description and Operation

The phase-controlled, full-bridge, series-parallel resonant dc-dc power converter with simplified inductive coupler, capacitive output filter and voltage-source load is shown in Fig. 4-1. The power stage of the converter is identical to that used in the basic frequency-controlled converter.

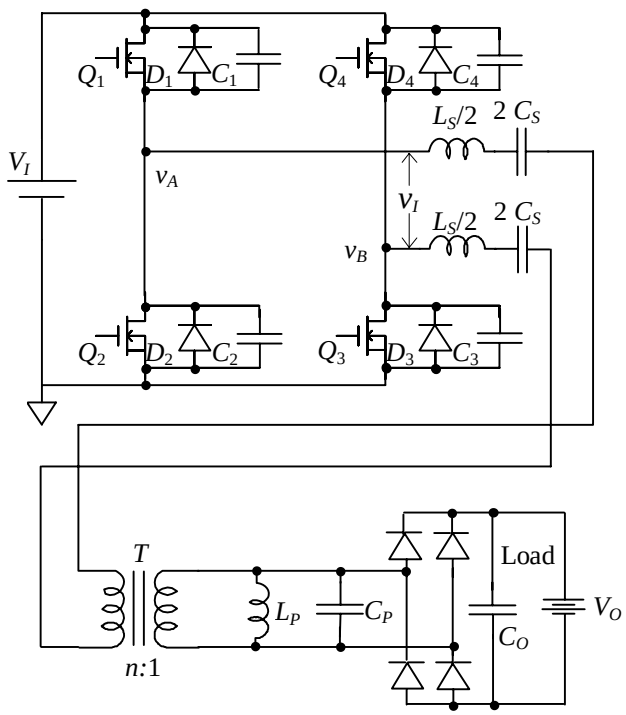

Fig. 4-1. Phase-controlled, full-bridge, isolated, series-parallel resonant converter with capacitive output filter and voltage-source load.

The full bridge consists of the controlled switches, Q_1, Q_2, Q_3 and Q_4, their intrinsic antiparallel diodes, D_1, D_2, D_3 and D_4, and the capacitances, C_1, C_2, C_3 and

C_4, to implement zero-voltage-switching. The resonant network consists of two separate resonant tank circuits: the L_S, C_S series tank and the L_P, C_P parallel tank. The parallel tank has component values as defined in the SAE J-1773 standard.

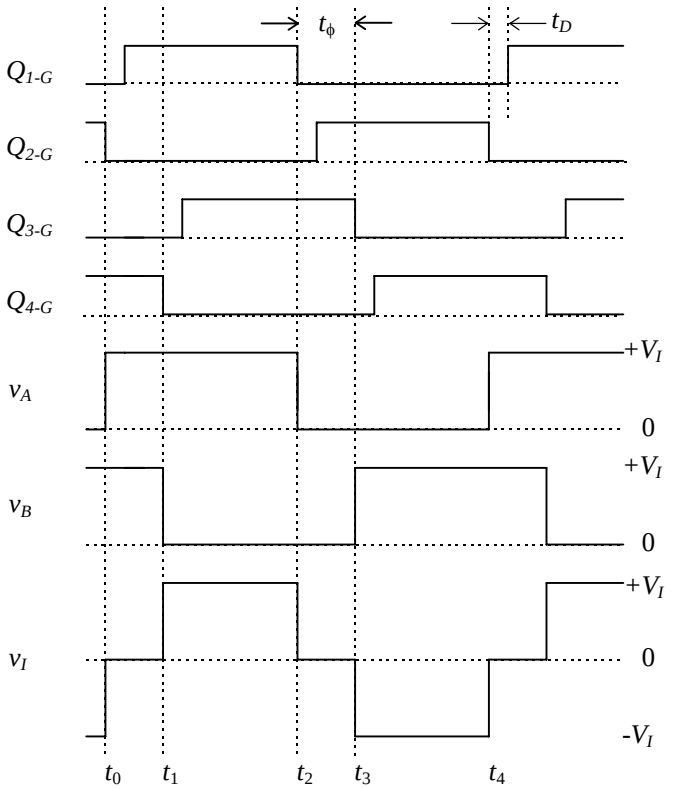

Fig. 4-2. Gate drive signals, $Q_{1\text{-}G}$, $Q_{2\text{-}G}$, $Q_{3\text{-}G}$ and $Q_{4\text{-}G}$, pole voltages, $v_A(t)$ and $v_B(t)$, and inverter output voltage, $v_I(t)$.

The gate drive, pole and inverter output voltages are shown in Fig. 4-2. For both frequency-controlled and phase-controlled modes, Q_1 through Q_4 are gated with 50% duty cycles, neglecting the dead-time, t_D. Additionally, Q_1 and Q_3 are gated in a complementary fashion to Q_2 and Q_4, respectively. In frequency-controlled mode, when $\phi = 0^O$, pair Q_1 and Q_3, and pair Q_3 and Q_4 are gated together. However, in phase-controlled mode the gatings of Q_3 and Q_4 are delayed by a radian angle, ϕ, corresponding to the time duration, t_ϕ, relative to the gatings of Q_1 and Q_2, respectively. The pole voltages, designated v_A and v_B, are subtracted to give the inverter output voltage, v_I, which is the ac voltage input to the series tank. Note that the transitions of v_A and v_B are synchronized with the negative transitions of their respective gate drives. Such a synchronization occurs when the converter is operating in ZVS mode, the desired condition for efficient operation.

4.3. FMA ANALYSIS OF CONVERTER

Three equivalent circuits for the full-bridge frequency and phase-controlled series-parallel resonant converter with capacitive output filter and battery load are shown in Fig. 4-3. The simplified time-domain circuit is shown in Fig. 4-3(a). The pole voltages are represented by square-wave voltage sources, $v_A(t)$ and $v_B(t)$, whose difference is equivalent to the net input voltage to the resonant tanks, $v_I(t)$. The input voltage is filtered by the four passive elements of the resonant tanks and the voltage across the parallel tank is rectified and fed to the dc battery load. The fundamental mode equivalent circuit is shown in Fig. 4-3(b). To simplify the analysis, the circuit can be reduced to the simple equivalent circuit of Fig. 4-3(c) in which $\mathbf{v_I} = \mathbf{v_A} - \mathbf{v_B}$.

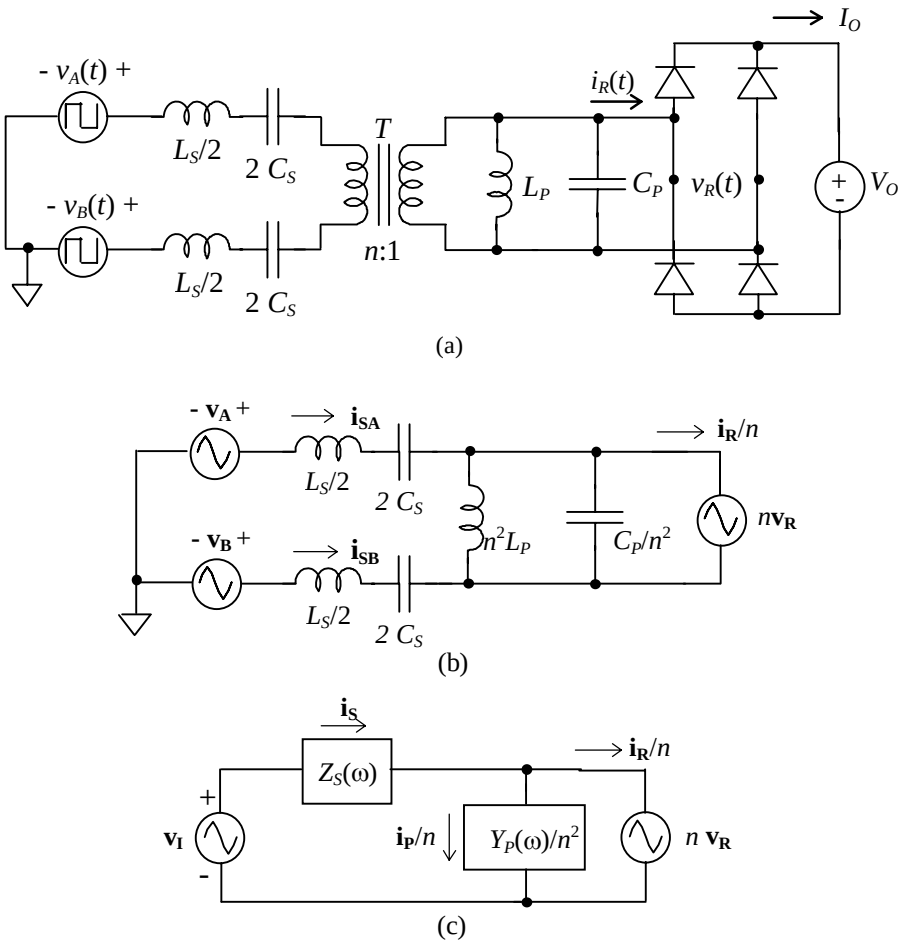

Fig. 4-3. FMA equivalent circuits.

As explained previously in Chapter Three, in basic FMA Analysis, the input voltage source, $v_I(t)$, the rectifier voltage, $v_R(t)$, and the rectifier current, $i_R(t)$, are represented by the sine wave phasors, $\mathbf{v_I}$, $\mathbf{v_R}$ and $\mathbf{i_R}$, respectively, whose magnitude and phase angles are those of their respective fundamental components. Similarly,

the square-wave pole voltage sources, $v_A(t)$ and $v_B(t)$, are represented by the sine wave voltage source phasors, $\mathbf{v_A}$ and $\mathbf{v_B}$, whose magnitudes and phase angles are those of the fundamental components of $v_A(t)$ and $v_B(t)$, respectively.

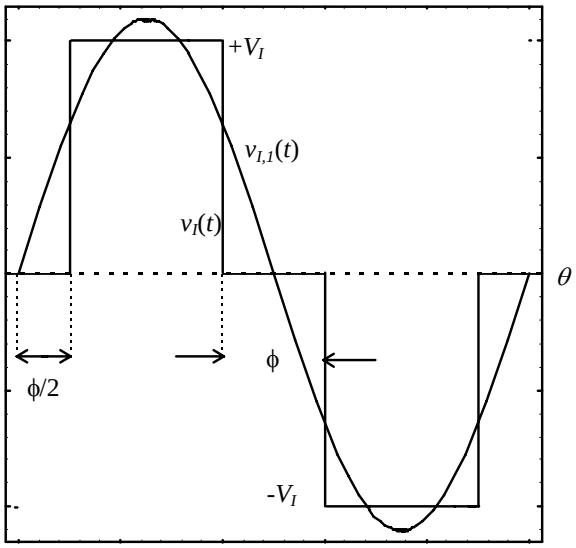

Fig. 4-4. Input voltage, $v_I(t)$ and fundamental component, $v_{I,1}(t)$.

4.3.1. RMS and Phase Relationships

In order to apply FMA Analysis, some basic relationships must first be derived.

(1) The inverter input voltage, $v_I(t)$ is a quasi-square wave, as shown in Fig. 4-4. The rms value of the fundamental component of $v_I(t)$ can be determined from its Fourier Series expression and is given by

$$V_{Irms} = \frac{2\sqrt{2}}{\pi} V_I \cos\frac{\phi}{2} \tag{4-1}$$

The input voltage phasor, $\mathbf{v_I}$, to the resonant tank circuits is then defined as:

$$\mathbf{v_I} = V_{Irms} \angle \delta_I \tag{4-2}$$

where δ_I is the phase angle of $\mathbf{v_I}$ relative to $\mathbf{v_R}$, the reference phasor.

It can easily be seen in the voltage phasor diagram of Fig. 4-5 that voltages $\mathbf{v_A}$ and $-\mathbf{v_B}$ lead and lag the inverter input voltage $\mathbf{v_I}$ by an angle $\phi/2$ and are given by:

$$\mathbf{v_A} = \frac{\sqrt{2}}{\pi} V_I \angle\left(\delta_I + \frac{\phi}{2}\right) \tag{4-3}$$

and $$\mathbf{v_B} = \frac{\sqrt{2}}{\pi} V_I \angle\left(\delta_I - \pi - \frac{\phi}{2}\right) \tag{4-4}$$

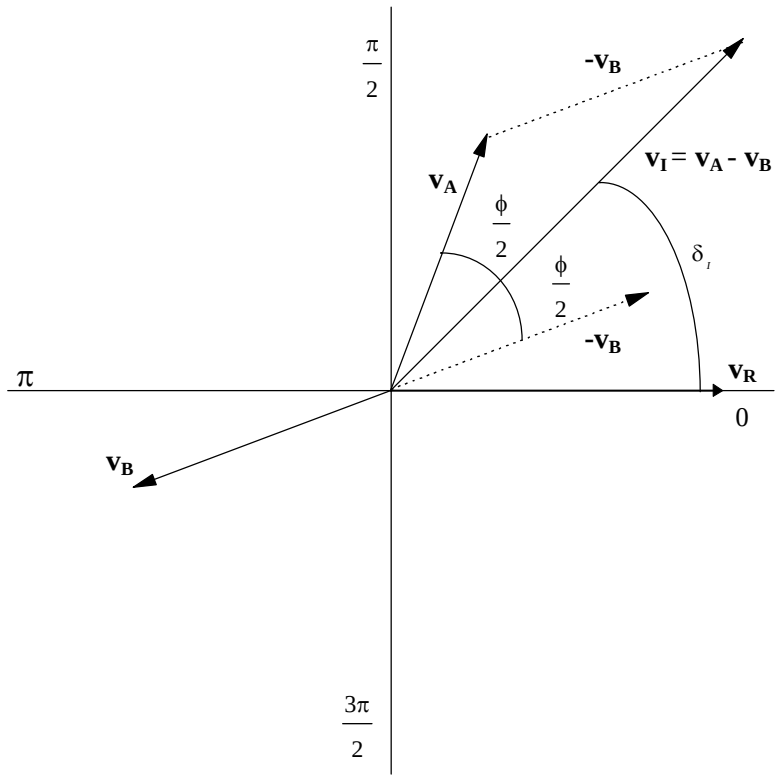

Fig. 4-5. Voltage phasor diagram.

(2) The output voltage, $v_R(t)$, is assumed to be a square wave of amplitude V_O so that V_{Rrms}, the rms value of the fundamental component, is given by

$$V_{Rrms} = \frac{2\sqrt{2}}{\pi} V_O \tag{4-5}$$

where V_O is the dc output voltage. The fundamental component is in phase with $v_R(t)$ and is assumed to be the reference phasor. Thus, the rectifier voltage phasor is

$$\mathbf{v_R} = \frac{2\sqrt{2}}{\pi} V_O \angle 0^{\circ} \tag{4-6}$$

(3) The current, $i_R(t)$, into the rectifier bridge is assumed to be a sine wave in phase with $v_R(t)$, and has a rectified average value equal to the dc output current I_O. Thus, the fundamental rms component, I_{RrmS}, is given by

$$I_{Rrms} = \frac{\pi}{2\sqrt{2}} I_O \tag{4-7}$$

The rectifier current phasor is given by:

$$\mathbf{i_R} = \frac{\pi}{2\sqrt{2}} I_O \angle 0^o \tag{4-8}$$

4.3.2. Basic Circuit Equations

From the fundamental mode equivalent circuit of Fig. 4-3(c), a relationship between the input voltage, the rectifier voltage, and the rectifier current, can be derived as

$$\mathbf{v_I} = \left\{1 - Z_S(\omega) Y_P(\omega) / n^2\right\} n \mathbf{v_R} + j Z_S(\omega) \frac{\mathbf{i_R}}{n} \tag{4-9}$$

The scalars $Z_s(\omega)$ and $Y_P(\omega)$ represent the magnitude of the impedance and admittance of the series and parallel branches, respectively, and are defined by:

$$Z_S(\omega) = \frac{\omega}{\omega_{OS}} \left(1 - \frac{\omega_{OS}^{\ 2}}{\omega^2}\right) Z_{OS} \tag{4-10}$$

and

$$Y_P(\omega) = \frac{\omega}{\omega_{OP}} \left(1 - \frac{\omega_{OP}^{\ 2}}{\omega^2}\right) Y_{OP} \tag{4-11}$$

where, as before, ω_{OS} and Z_{OS} are the natural resonant frequency and characteristic impedance of the series tank, respectively, and ω_{OP} and Y_{OP} are the natural resonant frequency and characteristic admittance of the parallel tank, respectively, and ω is the operating frequency of the converter.

Substituting the rms voltages and phase relationships (4-2), (4-6) and (4-8) into (4-9) gives

$$\frac{2\sqrt{2}}{\pi} V_I \cos\frac{\phi}{2} \left(\cos\delta_I + j \sin\delta_I\right) = \left\{1 - Z_S(\omega) Y_P(\omega) / n^2\right\} \frac{2\sqrt{2}}{\pi} n V_O + j Z_S(\omega) \frac{\pi}{2\sqrt{2}} \frac{I_O}{n} \tag{4-12}$$

Equate the real and imaginary components of (4-12).

$$V_I \cos\frac{\phi}{2} \cos\delta_I = \left\{1 - Z_S(\omega) Y_P(\omega) / n^2\right\} n V_O \tag{4-13}$$

$$V_I \cos\frac{\phi}{2} \sin\delta_I = Z_S(\omega) \frac{\pi^2}{8} \frac{I_O}{n} \tag{4-14}$$

Squaring and adding equations (4-13) and (4-14) gives:

$$\left(V_I \cos\frac{\phi}{2}\right)^2 = \left\{1 - Z_S(\omega) Y_P(\omega) / n^2\right\}^2 \left(n V_O\right)^2 + \left(Z_S(\omega) \frac{\pi^2}{8n}\right)^2 \left(\frac{I_O}{n}\right)^2 \tag{4-15}$$

Equation (4-15) is a very important equation, similar to equation (3-33) in the previous chapter, as it can be used to calculate or plot any single unknown for a

given set of circuit parameters or to develop design characteristics for the converter. For example, the dc output current I_O can be determined if the input and output voltages and circuit parameters are known.

$$I_O = n\frac{8}{\pi^2}\frac{1}{Z_S(\omega)}\sqrt{\left(V_I\cos\frac{\phi}{2}\right)^2 - \left(1 - Z_S(\omega)Y_P(\omega)/n^2\right)^2\left(nV_O\right)^2} \qquad (4\text{-}16)$$

Again, if I_O is known, other critical circuit currents can be easily derived. The circuit equations can be normalized in terms of the input voltage, V_I, and the parallel tank parameters, Y_{OP} and ω_{OP}. The normalized form of (4-16) is written as:

$$I_{ON} = n\frac{8}{\pi^2}\frac{1}{Z_{SN}(\omega_N)}\sqrt{\cos^2\frac{\phi}{2} - \left(1 - Z_{SN}(\omega_N)Y_{PN}(\omega_N)/n^2\right)^2\left(nV_{ON}\right)^2} \qquad (4\text{-}17)$$

where the subscript N designates that the variable is normalized.

Normalized output current, I_{ON}, is plotted against the normalized operating frequency, ω_N, for various output voltages and for a given parameter set in Fig. 4-6 above. As the phase control angle, ϕ, is increased, the current is reduced. Angle ϕ does not have to be increased over its full modulation range to reduce the current to zero. The maximum value of ϕ required to reduce the current to zero varies from approximately 80° at V_{ON} = 1.25 to 130° at V_{ON} = 0.75.

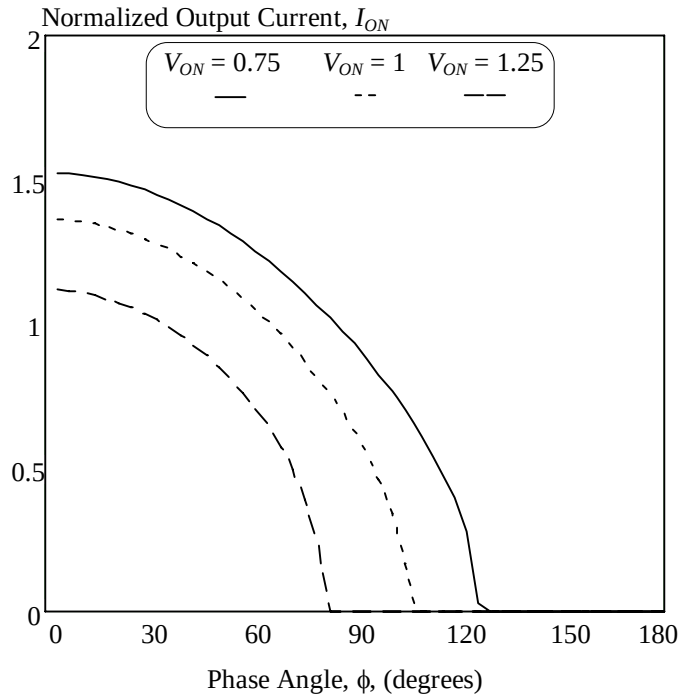

Fig. 4-6. Normalized output current, I_{ON}, calculated using FMA Analysis, as a function of phase control angle, ϕ, for various values of V_{ON}, at ω_N = 1.5, ω_{SN} = 0.5 and ω_{CN} = 2.

The current in the series tank, $\mathbf{i_S}$, is the sum of the rectifier current, $\mathbf{i_R}/n$, and the parallel tank current, $\mathbf{i_P}/n$:

$$\mathbf{i_S} = \frac{\mathbf{i_R}}{n} + \frac{\mathbf{i_P}}{n} \tag{4-18}$$

or

$$\mathbf{i_S} = \frac{\pi}{2\sqrt{2}} I_O + jY_P(\omega)\frac{2\sqrt{2}}{\pi} V_O \tag{4-19}$$

The phase angle δ_S of $\mathbf{i_S}$ is then easily determined:

$$\delta_S = \tan^{-1}\left(\frac{|\mathbf{i_P}|}{|\mathbf{i_R}|}\right) = \tan^{-1}\left(\frac{8}{\pi^2}\frac{V_O}{I_O}Y_P(\omega)\right) \tag{4-20}$$

The phase angle of the input voltage, δ_I, is given by (4-13) as

$$\delta_I = \cos^{-1}\left\{\left\{1 - Z_S(\omega)Y_P(\omega)/n^2\right\}\frac{nV_O}{V_I\cos\frac{\phi}{2}}\right\} \tag{4-21}$$

The power factor angle, δ_L, of the series current relative to the input voltage is given by

$$\delta_L = \delta_I - \delta_S \tag{4-22}$$

The power factor angles between the series current and the pole voltages are designated δ_{LA} and δ_{LB} for poles A and B, respectively, and are given by:

$$\delta_{LA} = \delta_I - \delta_S + \frac{\phi}{2} \tag{4-23}$$

and

$$\delta_{LB} = \delta_I - \delta_S - \frac{\phi}{2} \tag{4-24}$$

If either δ_{LA} or δ_{LB} is negative, the inverter loses ZVS. Clearly, from (4-24), Leg B is more likely to have a negative phase angle than Leg A due to the subtraction of $\phi/2$. To maintain a positive phase lag and zero-voltage switching, the conditions for maintaining δ_{LB} positive must be examined.

$$\delta_{LB} = \cos^{-1}\left\{\left(1 - Z_S(\omega)Y_P(\omega)/n^2\right)\frac{nV_O}{V_I\cos(\phi/2)}\right\} - \tan^{-1}\left\{\frac{8}{\pi^2}\frac{V_O}{I_O}Y_P(\omega)\right\} - \frac{\phi}{2} \tag{4-25}$$

The expanded equation (4-25) for δ_{LB} is complicated as it has three terms which affect whether a positive angle can be maintained over the load range. The third term in (4-25) will inevitably reduce the ZVS range due to the substraction of $\phi/2$. Thus, as ϕ increases from 0 to π, it pushes δ_{LB} in a negative direction towards a loss

of ZVS. The second term is significant at high frequency and light load. Its contribution to a negative trend in δ_{LB} decreases as frequency increases due to the parallel tank becoming more capacitive.

The first term in equation (4-25), written as

$$\cos^{-1}\left\{\left(1-Z_S(\omega)Y_P(\omega)/n^2\right)\frac{nV_O}{V_I\cos(\phi/2)}\right\} \tag{4-26}$$

always contributes positively towards δ_{LB}. If a positive δ_{LB} is to be achieved at a given operating point, the magnitude of (4-26) must be greater than the sum of the second and third terms in equation (4-25). A closer examination of the (4-26) emphasizes the critical role of the current-source frequency, ω_C, in the converter ZVS range. For frequencies below ω_C, the $\left(1-Z_S(\omega)Y_P(\omega)/n^2\right)$ component is always positive but as ϕ increases in this frequency range, the contribution of (4-26) to δ_{LB} decreases, reducing the likelihood of achieving ZVS. The converse is true for the frequency range above ω_C. In this case, the $\left(1-Z_S(\omega)Y_P(\omega)/n^2\right)$ component is always negative and as ϕ increases, the contribution of (4-26) to δ_{LB} also increases resulting in ZVS over the phase control range. Thus, the converter must operate above the current-source frequency in order to achieve ZVS over the complete phase control angle range. This key characteristic can easily be observed in Fig. 4-7 where power factor angle δ_{LB} is plotted as a function of ω_N. In general, below the current-source frequency, $\omega_C = 2$, as ϕ increases, δ_{LB} decreases and eventually goes negative. Above the current-source frequency, as ϕ increases, δ_{LB} also increases, remains positive and thereby maintains the critical condition for ZVS.

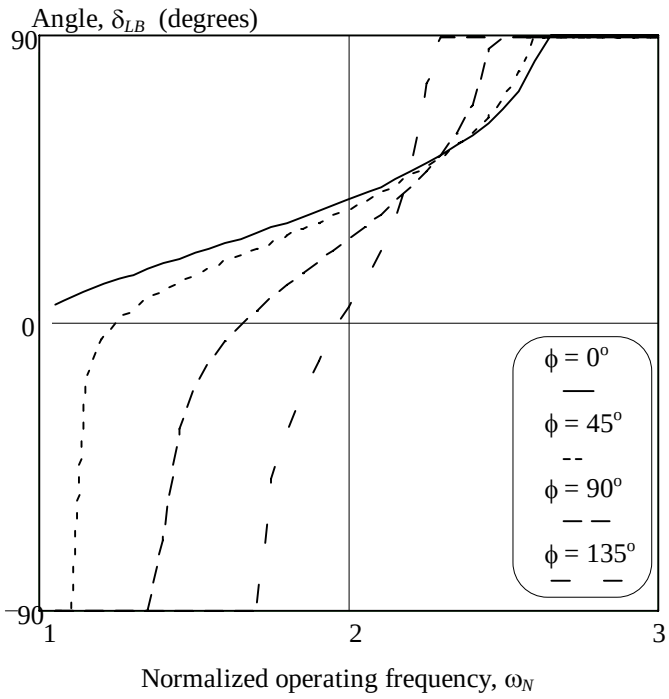

Fig. 4-7. FMA generated phase factor angle, δ_{LB}, as a function of normalized operating frequency, ω_N, for various values of phase control angle, ϕ, at $V_{ON} = 1$, $\omega_N = 1.5$, $\omega_{SN} = 0.5$ and $\omega_{CN} = 2$.

4.4. RCFMA ANALYSIS

RCFMA Analysis has already been shown in Chapter Three to provide a more accurate analysis than FMA Analysis. In this section, the application of RCFMA Analysis to the phase control converter is investigated.

4.4.1. RMS and Phase Relationships

The rectifier voltage and current rms factors, K_V and K_A, and their respective phase angles, δ_V and δ_A, derived in Chapter Three, are also used in the analysis of the phase-controlled converter. The phase angles in the RCFMA Analysis are measured with respect to the reference phasor defined in the two-element circuit analysis of Chapter Three. The rms value and phase angle of the input voltage derived for FMA Analysis obviously remains valid for the RCFMA Analysis.

Again, the usual RCFMA Analysis assumptions are made:

(1) The rectifier voltage, $v_R(t)$, is assumed to be a clamped quasi-square wave of amplitude V_O so that the rectifier voltage phasor is

$$\mathbf{v_R} = K_V V_O \angle \delta_V \tag{4-27}$$

(2) The current, $i_R(t)$, into the rectifier bridge is assumed to be a segmented sine wave, as shown in Fig. 3-12. The average value of the waveform is I_o so that the rectifier current phasor is

$$\mathbf{i_R} = K_A I_O \angle \delta_A \tag{4-28}$$

4.4.2. Circuit Equations

The basic RCFMA circuit equation in phasor form can be derived by substituting (4-27) and (4-28) into (4-9):

$$\frac{2\sqrt{2}}{\pi} V_I \cos\frac{\phi}{2} \angle \delta_I = \left\{1 - Z_S(\omega) Y_P(\omega)/n^2\right\} \sqrt{2} K_V n V_O \angle \delta_V + j Z_S(\omega) \sqrt{2} K_A \frac{I_O}{n} \angle \delta_A \tag{4-29}$$

Express (4-29) in trigonometric notation.

$$\begin{aligned} \frac{2\sqrt{2}}{\pi} V_I \cos\frac{\phi}{2} (\cos\delta_I + j\sin\delta_I) = \left\{1 - Z_S(\omega) Y_P(\omega)/n^2\right\} K_V n V_O (\cos\delta_V + j\sin\delta_V) \\ + j Z_S(\omega) K_A \frac{I_O}{n} (\cos\delta_A + j\sin\delta_A) \end{aligned} \tag{4-30}$$

Equate the real and imaginary components.

$$\begin{aligned} V_I \cos\frac{\phi}{2} \cos\delta_I = \left\{1 - Z_S(\omega) Y_P(\omega)/n^2\right\} \frac{\pi}{2\sqrt{2}} K_V n V_O \cos\delta_V - \\ Z_S(\omega) \frac{\pi}{2\sqrt{2}} K_A \frac{I_O}{n} \sin\delta_A \end{aligned} \tag{4-31}$$

$$\begin{aligned} V_I \cos\frac{\phi}{2} \sin\delta_I = \left\{1 - Z_S(\omega) Y_P(\omega)/n^2\right\} \frac{\pi}{2\sqrt{2}} K_V n V_O \sin\delta_V + \\ Z_S(\omega) \frac{\pi}{2\sqrt{2}} K_A \frac{I_O}{n} \cos\delta_A \end{aligned} \tag{4-32}$$

Squaring the above two equations and adding gives

$$\begin{aligned} \left(V_I \cos\frac{\phi}{2}\right)^2 = \left[1 - Z_S(\omega) Y_P(\omega)/n^2\right]^2 \left(\frac{\pi}{2\sqrt{2}} K_V\right)^2 (n V_O)^2 + \left(Z_S(\omega) \frac{\pi}{2\sqrt{2}} K_A\right)^2 \left(\frac{I_O}{n}\right)^2 \\ + 2\left[1 - Z_S(\omega) Y_P(\omega)/n^2\right] Z_S(\omega) \frac{\pi^2}{8} K_V K_A n V_O \sin(\delta_V - \delta_A) \frac{I_O}{n} \end{aligned} \tag{4-33}$$

Equation (4-33) is the basic circuit equation which can be used to develop design characteristics for the converter. For example, the dc output current, I_o, can be determined as follows by expressing (4-33) in terms of I_o and then solving for I_o.

$$0 = a(\omega) I_O^{\,2} + b(\omega) I_O + c(\omega) \tag{4-34}$$

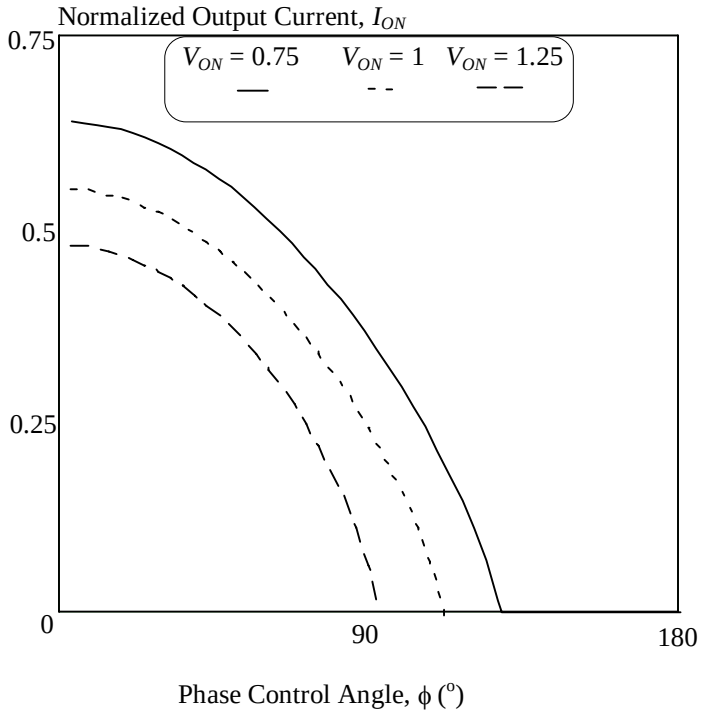

Fig. 4-8. Normalized output current, I_{ON}, calculated using RCFMA Analysis, as a function of phase control angle, ϕ, for various values of V_{ON}, at ω_N = 2.25, ω_{SN} = 0.5 and ω_{CN} = 2.

Using this more accurate analysis, the normalized output current, I_{ON}, is plotted as a function of ϕ in Fig. 4-8 for various output voltages and a given parameter set. The plots are calculated at ω_N = 2.25, a frequency just above the current-source frequency, where the FMA Analysis predicted that ZVS is achieved. At each output voltage, the current is reduced as the phase control angle, ϕ, is increased. As previously indicated by the FMA Analysis, ϕ does not have to be increased over its full modulation range to reduce the current to zero. The maximum value of ϕ required for zero current varies from approximately 92° at V_{ON} = 1.25 to 130° at V_{ON} = 0.75.

The power factor angle, δ_{LB}, derived using RCFMA Analysis is plotted as a function of ω_N in Fig. 4-9. The RCFMA plots have similar characteristics to the FMA plots, shown in Fig. 4-7. The main difference between the two sets of analyses is that the operating frequency to achieve a positive δ_{LB} is higher for RCFMA Analysis than that given by the FMA Analysis.

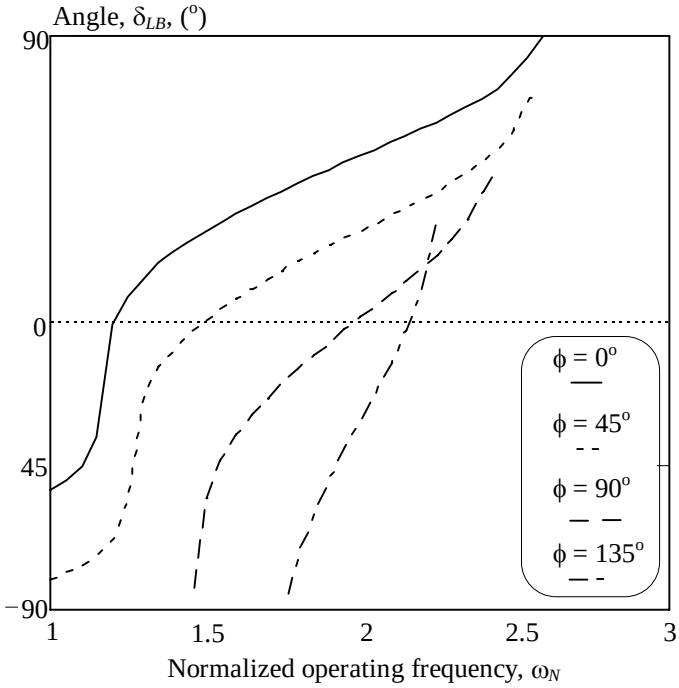

Fig. 4-9. RCFMA generated power factor angle, δ_{LB}, as a function of normalized operating frequency, ω_N, for various values of phase control angle, ϕ, at V_{ON} = 1, ω_{SN} = 0.5 and ω_{CN} = 2.

The principal converter design currents are plotted in Fig. 4-10. The plots show that the rms currents in the series tank, I_S, and rectifier, I_R, are significantly greater than the output current, I_O. This is to be expected due to the highly reactive nature of the converter at the operating frequency. The transistor rms and turn-off currents, I_{QA} and I_{QAO}, in pole A are significantly greater than the corresponding currents, I_{QB} and I_{QBO}, in pole B. Currents I_{QB} and I_{QBO} generally decrease as ϕ increases.

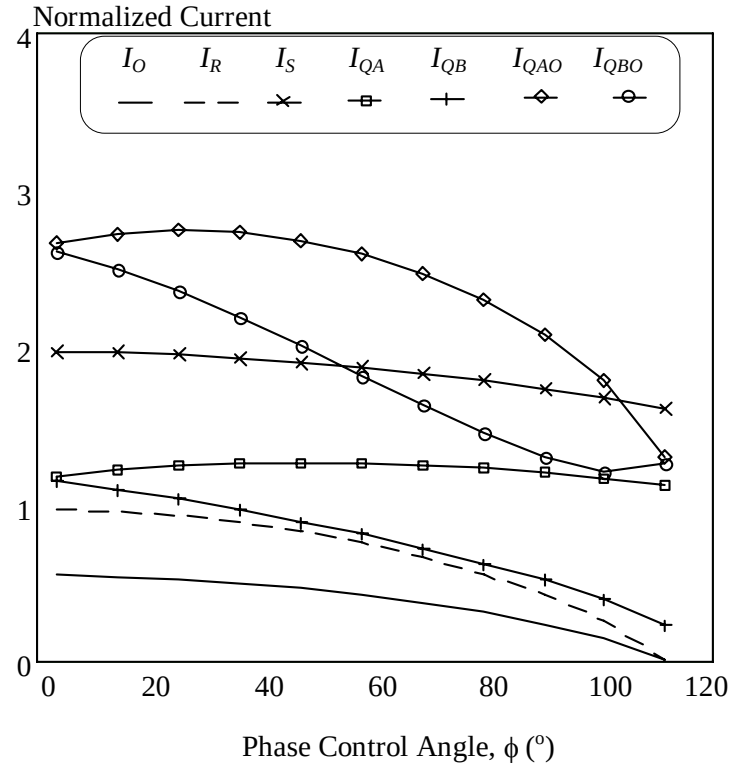

Fig. 4-10. Plot of normalized converter currents as a function of phase control angles, ϕ, for V_{ON} = 1, ω_N = 1.5, ω_{OSN} = 0.5, ω_{CN} = 2.

4.5. EXPERIMENTAL VALIDATION

A MOSFET-based prototype converter has been built and experimentally tested. The SAE J-1773 compatible converter is nominally designed to deliver 1 kW at 250V output and 150 kHz. The converter has the following parameters:

$$V_I = 200 \text{ V}$$
$$f_{OS} = 27 \text{ kHz}$$
$$f_{OP} = 119 \text{ kHz}$$
$$f_C = 185 \text{ kHz}$$
$$Y_{OP} = 0.03 \text{ S}$$
$$n_P = 4$$
$$n_S = 4$$

Initially, it is necessary to determine an optimum frequency of operation using RCFMA Analysis. The pole B power factor angle, δ_{LB}, is plotted against frequency in Fig. 4-11. The RCFMA Analysis predicts that the converter will operate with ZVS

for any operating frequency above 200 kHz. Thus, the theory of operation will be validated experimentally at 220 kHz.

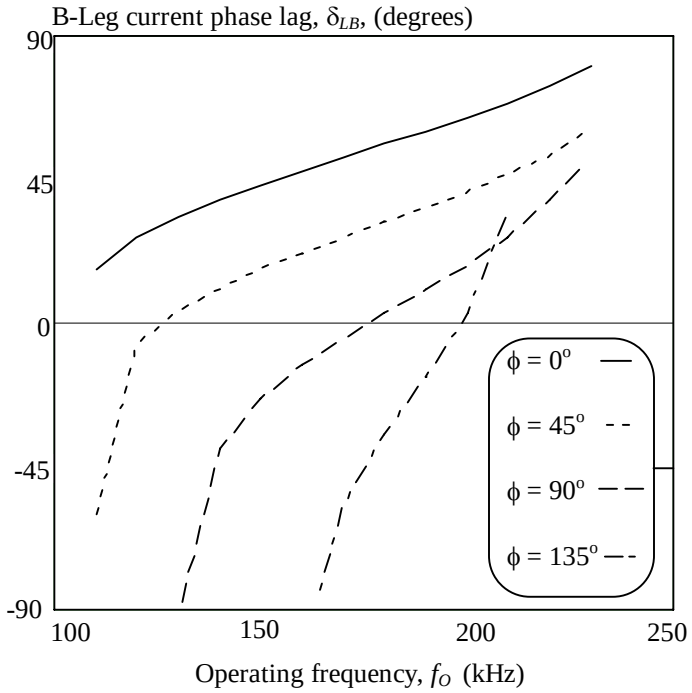

Fig. 4-11. RCFMA-based power factor angle, δ_{LB}, as a function of operating frequency, f_O, for different values of phase control angle, ϕ, at V_O = 200V.

Experimental waveforms for phase control angles of 0^0, 36^0, 72^0, 108^0 and 144° or modulation percentages of 0%, 20%, 40%, 60% and 80% are shown in Fig. 4-12(a)-(e), respectively. The waveforms show that as ϕ is increased, the converter maintains a positive δ_{LB} and consequently operates in ZVS mode for both turn-on and turn-off. The current i_s always lags v_I, ensuring ZVS MOSFET turn-on. Significant current is available at turn-off to allow zero-voltage turn-off of the MOSFETs. For ϕ = 144°, shown in Fig. 4-12(e), the rectifier no longer conducts during any part of the cycle as is clear from the purely sinusoidal nature of v_R. Current i_s has also been reduced significantly, resulting in insufficient current being available to soft transition the MOSFET switching. Thus, the MOSFETs experience a hard switch transition as shown.

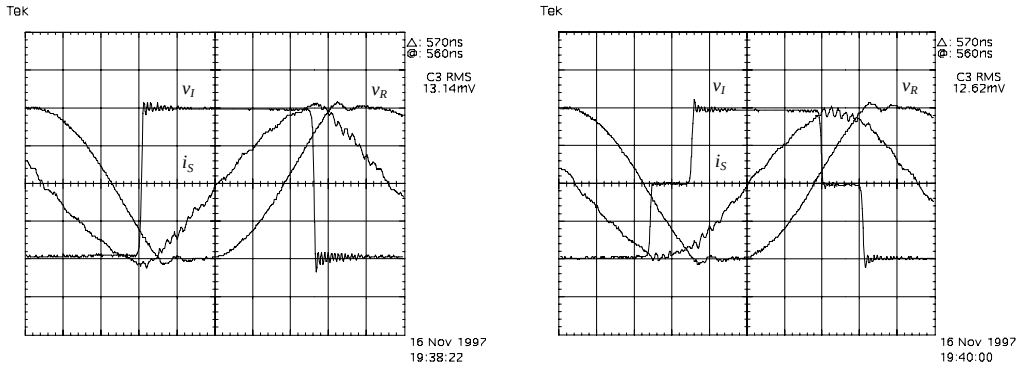

(a)

(b)

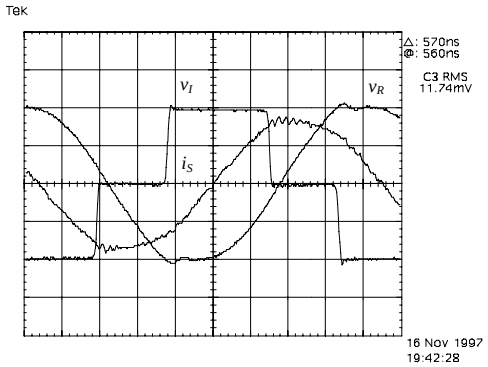

(c)

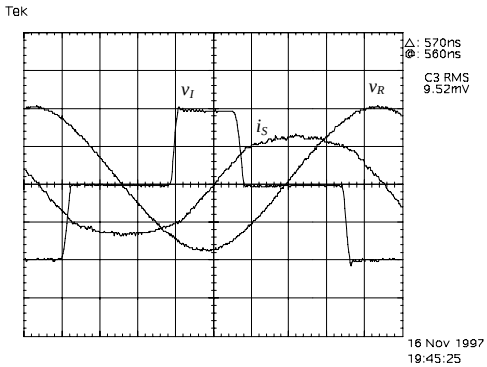

(d)

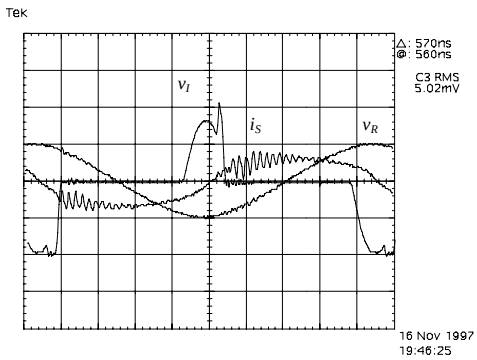

(e)

Fig. 4-12. Experimental waveforms for the inverter input voltage, v_I, series tank current, i_S, and rectifier voltage, v_R, at f_O = 220 kHz and V_O = 200 V, for ϕ equals (a) 0°, (b) 36°, (c) 72°, (d) 108°, and (e) 144°. (Scale: 100V/div., 5A/div.)

Comparisons of critical converter currents predicted by RCFMA Analysis and measured experimentally are shown in Fig. 4-13. The data sets plotted in Fig. 4-13 for unity voltage gain show that RCFMA predictions correlate well with the experimental results. At zero phase shift and V_o = 200 V, the error in I_s is less than 7%: RCFMA Analysis predicting 7.5 A while the actual measurement is 7 A. In the

case of I_o the error is 21% at the same load point: RCFMA Analysis predicting 1.58 A versus a measurement of 1.25 A. This result is consistent with the accuracy of RCFMA Analysis at high frequencies. The error in I_o is larger than the error in I_s because at high frequencies, I_o is relatively small compared to the resonant currents, such as I_s. The discrepancies between the experimental and analytical data sets can be explained by a number of factors, such as the relatively low efficiency of the converter in this operating load range, the inherent inaccuracies of the RCFMA Analysis, and the measurement error. RCFMA Analysis also predicts the B pole turn-off current, I_{QBO}, with reasonable accuracy but underestimates the measured value slightly, unlike the currents, I_s and I_o, which are overestimated. RCFMA Analysis calculates I_{QBO} from the fundamental components of the circuit voltages and currents. However, as shown by the experimental waveforms, I_{QBO} is significantly effected by the harmonics of the series current. This harmonic content is not obviously factored into RCFMA Analysis and results in the underestimation of I_{QBO}.

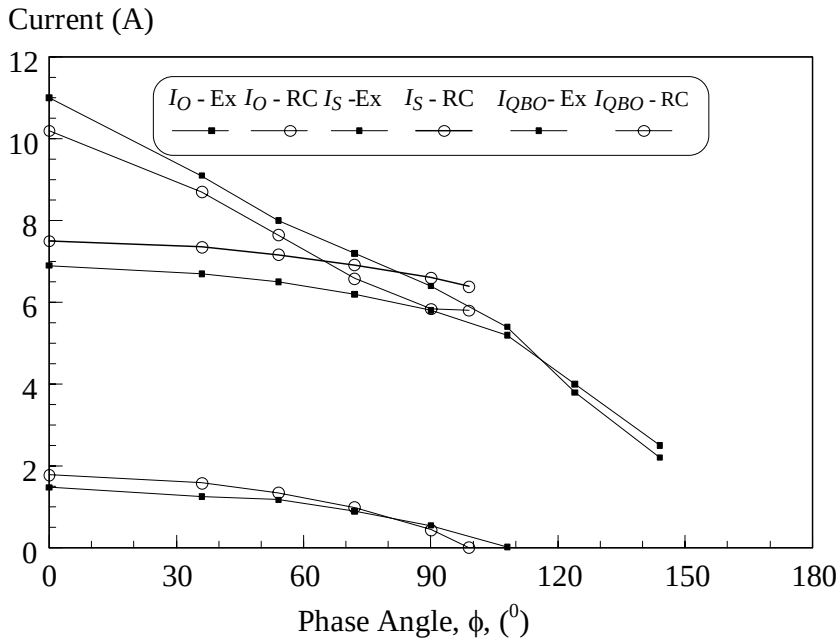

Fig. 4-13. RCFMA (RC) and experimental (Ex) converter currents, I_o, I_s, and I_{QBO} versus phase control angle, ϕ, at f_o = 220 kHz and V_o = 200 V.

A useful feature of the converter is illustrated in Fig. 4-13 which shows that the series current, I_s, can be further reduced by increasing the phase-control angle, ϕ, beyond the value required to reduce the dc output current, I_o, to zero. This feature can reduce the power losses of the converter in an idling condition, i.e. powered-up

with no demanded output power, and is an advantage of this converter compared to the frequency-controlled converter where no-load power losses remain high.

Maintaining ZVS over the load range is critical to minimize power losses. Converter power loss, P_L, is plotted against phase control angle, ϕ, for various values of output voltage in Fig. 4-14. As ϕ increases from zero, P_L is reduced, largely due to the reduction in series current, I_s, but when ϕ increases above approximately 130° the converter enters a hard switching region and converter losses increase. In a practical converter, the maximum operational value of ϕ would be clamped to avoid the loss of ZVS.

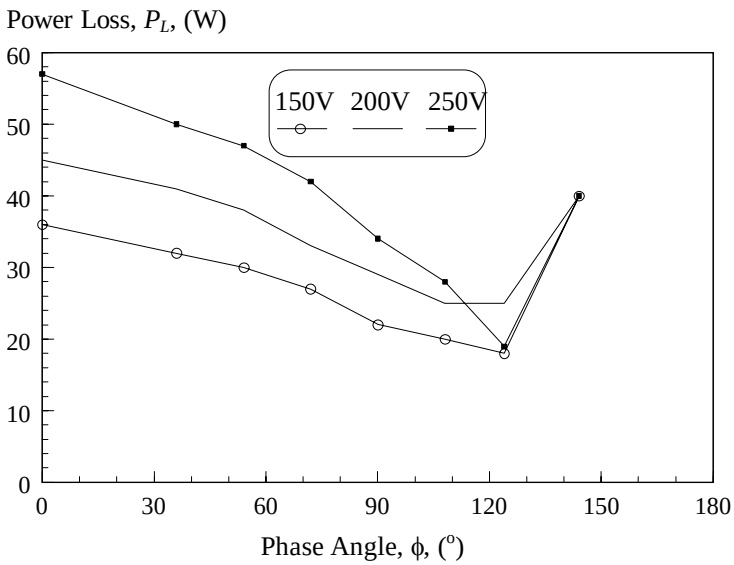

Fig. 4-14. Measured converter power loss, P_L, versus phase control angle, ϕ, for various V_O values.

A desirable feature of phase control is the reduction in the converter power loss at light load as compared with frequency control. Experimental power losses, measured for both frequency control and phase control techniques, are shown in Fig. 4-15, with the frequency-controlled losses being plotted using thin lines. Phase control is implemented at medium load at 220 kHz and the associated power losses are plotted using bold lines. The power loss for frequency-controlled operation varies from 65W at 0.97 kW, 250V output to 46 W at 0 kW output. As can be seen in Fig. 4-15, the losses can be reduced significantly using phase control when the load power decreases. At the 10% power point, or 100W, 250 V output, the losses can be reduced from 52 W using frequency control to 42 W using phase control,

resulting in an efficiency improvement from 66% to 70%. At 50W output, the efficiency improves from 51% to 57%. The no-load loss can be reduced significantly below that shown in Fig. 4-15 where the no-load loss at 250V output for frequency control is 46 W versus 34W for phase control.

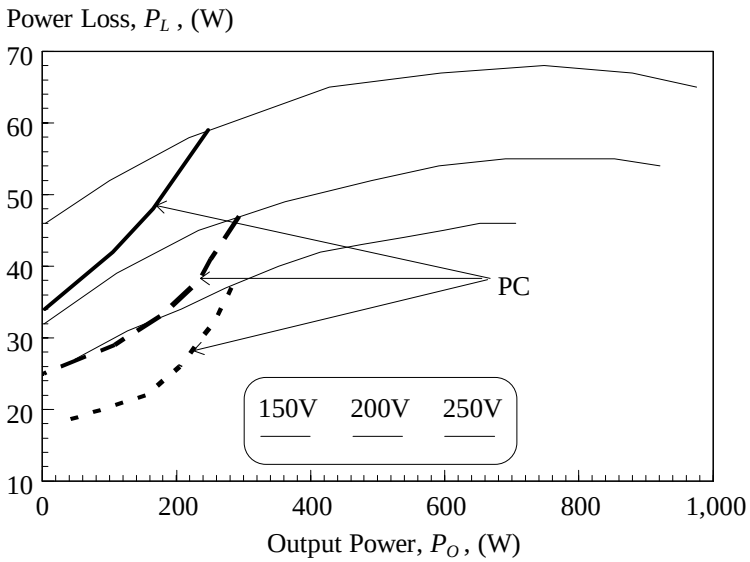

Fig. 4-15. Comparison of measured converter power loss, P_L, for frequency control and phase control as a function of output power, P_o, for various V_o values.

Finally, RCFMA Analysis predicts that the converter will lose ZVS when operated at lower frequencies, as shown in Fig. 4-11. In the expermental test, the converter is phase-controlled at 150 kHz. Power losses are measured and compared with the power losses of the frequency-controlled converter. The comparison is shown in Fig. 4-16. As predicted by RCFMA Analysis, the converter loses ZVS and the converter losses increase very significantly as the output power is reduced. The phase-controlled losses peak at 130W for an output power of about 380W, whereas at this output power the frequency-controlled losses are only 48 W. This large increase in phase-controlled losses is mainly due to the reverse recovery losses of the slow intrinsic diodes of the inverter MOSFETs. These losses can be reduced by using faster diodes but device costs are significantly increased.

Clearly, as expected, phase control over a wide modulation range necessitates that the operating frequency be increased above the current-source frequency. Since this is inherently an inefficient operating zone due to the highly reactive nature of the tank circuits, it is suggested that Hybrid Frequency and Phase Control (HFPC)

be employed with phase control being used to limit the frequency range required to reduce the output power to zero.

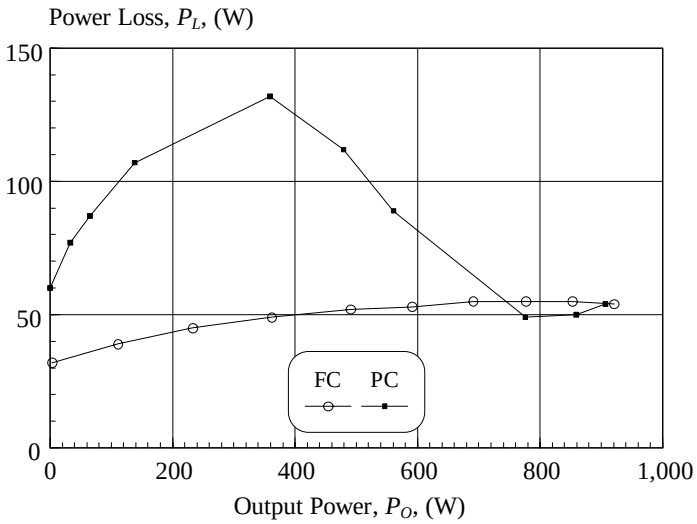

Fig. 4-16. Comparison of measured converter power loss, P_L, versus output power, P_O, for frequency control and constant frequency phase control at f_o = 150 kHz, V_o = 200 V.

4.6. CONCLUSIONS

In this chapter, the application of phase control to the series-parallel LCLC resonant converter with capacitive output filter was investigated. The characteristics were analyzed using basic FMA Analysis and the more accurate RCFMA Analysis. The analyses identified an operating frequency range above the converter's current-source frequency, where it is advantageous to phase control the converter, resulting in a novel hybrid control scheme integrating frequency and phase control. The theory and experimental results show that combining the two control modes results in the following advantages.

1. Reduced control frequency range of 60-70% of the range required for frequency control alone.
2. Reduced low-load losses in power components, gate drives and improved charge cycle efficiency.
3. Significantly reduced converter idling power losses.

The theory was validated using an experimental prototype and the analytical and measured data showed excellent correlation.

It can thus be concluded that true full-load phase control cannot be achieved using the constant-frequency phase-controlled series resonant converter driving the

SAE J-1773 vehicle inlet, although a hybrid variable frequency and phase control scheme can result in reduced light load losses and a smaller frequency control range. In the next chapter, an alternative J-1773 compatible phase-controlled resonant power topology is investigated.

REFERENCES

[1] J.G. Hayes, J.T. Hall, M.G. Egan, J.M.D. Murphy, "Full-Bridge, Series-Resonant Converter Supplying the SAE J-1773 Electric Vehicle Inductive Charging Interface," *IEEE Power Electronics Specialists Conf. Rec*., 1996, pp. 1913-1918.

[2] J.G. Hayes, S.E. Schulz, J.T. Hall, M.G. Egan, J.M.D. Murphy, "Wide Load Resonant Converter Supplying the SAE J-1773 Electric Vehicle Inductive Charging Interface," *IEEE Industrial Applications Society Conf. Rec*., 1996.

[3] I.J. Pitel, "Phase-Modulated Resonant Power Conversion Techniques," *IEEE Trans. Industrial Applications*, Vol. IA-22, Nov./Dec. 1986, pp. 1044-1051.

[4] F. Tsai, P. Materu, F.C. Lee, "Constant Frequency, Clamped-Mode Resonant Converters," *IEEE Power Electronics Specialists Conf. Rec*., 1987, pp. 557-566.

[5] J. Hayes, C. Henze, N. Mohan, "Zero-Voltage Switching in a Constant Frequency Digitally Controlled Resonant DC-DC Power Supply," *IEEE Applied Power Electronics Conf. Rec*., 1988, pp. 360-367.

[6] P. Jain, H. Soin, "A Constant Frequency Parallel Tuned Resonant Dc/dc Converter for High Voltage Applications," *IEEE Power Electronics Specialists Conf. Rec*., 1992, pp. 71-76.

[7] C. Loef, "Analysis of a Full-Bridge LCC-type Parallel Resonant Converter with Capacitive Output Filter," *IEEE Power Electronics Specialists Conf. Rec*., 1997, pp. 1402-1407.

[8] M.K. Kazimierczuk, D. Czarkowski, "Phase Control of Series Resonant Converter," *IEEE Power Electronics Specialists Conf. Rec*., 1993, pp. 1002-1008.

[9] D. Czarkowski, M.K. Kazimierczuk, "Phase-Controlled Series-Parallel Resonant Converter," *IEEE Trans. Power Electronics*, Vol. 8, No. 3, July 1993, pp. 309-319.

[10] D. Czarkowski, M.K. Kazimierczuk, "Phase-Controlled CLL Resonant Converter," *IEEE Power Electronics Specialists Conf. Rec*., 1992, pp. 432-438.

5.

CHAPTER FIVE

PHASE CONTROL OF THE PARALLEL-LOAD SERIES-PARALLEL RESONANT CONVERTER WITH CAPACITIVE FILTER AND VOLTAGE- SOURCE LOAD

Abstract: In this chapter, the application of phase control to the four-element LCLC parallel-load, series-parallel resonant converter, with capacitive output filter and voltage source load, is introduced, analyzed, and validated experimentally. The converter is analyzed, and the steady-state operating characteristics are obtained using Rectifier-Compensated Fundamental Mode Approximation (RCFMA) Analysis. Both analysis and experimental results show that the converter has many of the characteristics of the closely related frequency-controlled, series-load converter. In addition, the converter implements soft-switching over the entire load range, resulting in high full-load and partial-load efficiencies. This feature, combined with the constant-frequency phase control operation, makes the converter an excellent option for the inductive coupling application. Experimental results are obtained using a 1 kW, 250 V, SAE J-1773 compatible prototype. Very good correlation is shown between the analytical and experimental results.

5.1. INTRODUCTION

It has been shown in Chapter Two that the frequency-controlled (FC) series-parallel resonant converter offers many significant advantages in the electric vehicle inductive charging application. However, the principal disadvantage of this resonant converter is the wide operating frequency range which results in poor power transfer efficiency at partial loads. The wide operating frequency range also results in bulky gate drives, inefficient power component utilization, especially in the costly high-frequency magnetics, and high passive and active component voltage and current stresses at light loads. Finally, the wide frequency range makes it difficult to optimize filter design to limit the electromagnetic interference due to the power converter.

Phase-controlled resonant converters have been proposed and studied [3-10] as options to address some of the problems associated with frequency-controlled converters, as mentioned above. The application of phase control to the series-parallel resonant converter was investigated in Chapter 4. The limited load range was shown to be a major limitation, significantly reducing the advantages that phase control can offer.

A new family of soft-switched phase-controlled resonant converters using a Class D or parallel load configuration has been presented, analyzed and validated [8-10]. Combining the basic resonant converter topology and the parallel load results in a high-efficiency PC converter, soft-switched over the full load range. The authors of [8-10] have analyzed various two-element and three-element converters with inductive output filters.

In this chapter, the Phase-Controlled Parallel-Load series-parallel LCLC (PCPL) resonant converter with capacitive output filter and voltage-source load is studied to determine whether it can offer a high efficiency, constant frequency solution for inductive charging.

Many different analytical approaches can be used to derive the steady-state operating characteristics of the converter. Modal Analysis has frequently been used to provide accurate analyses of resonant converters utilizing phase control [4,5] and frequency control[1,2]. However, Modal Analysis is mathematically complex and requires detailed knowledge of the steady-state characteristic waveforms of the converter. Thus, Modal Analysis is not a very useful tool for initial study and investigation of converter operation. As previously demonstrated, Rectifier Compensated FMA (RCFMA) Analysis, provides an accurate analysis of the frequency- and phase-controlled versions of the multi-element, multi-resonant converter. Thus, the operating characteristics of the phase-controlled converter are generated here using RCFMA Analysis.

The basic PCPL converter description and operation are presented in Section 5.2. In Section 5.3, the converter is analyzed mathematically using RCFMA Analysis. Practical results from an experimental prototype are compared with the analytical results in Section 5.4. The three different series-parallel resonant converters investigated in the thesis are compared in Section 5.5.

5.2. CONVERTER DESCRIPTION AND OPERATION

The isolated full-bridge parallel-load series-parallel resonant dc-dc power converter with simplified inductive coupler, capacitive output filter and battery load is shown in Fig. 5-1. The inverter stage of the converter is identical to the frequency-controlled series-load converter previously studied. However, in the parallel load converter, the parallel resonant tank, rectifier and load are connected in parallel with the common outputs of the inverter and series resonant tanks, as shown.

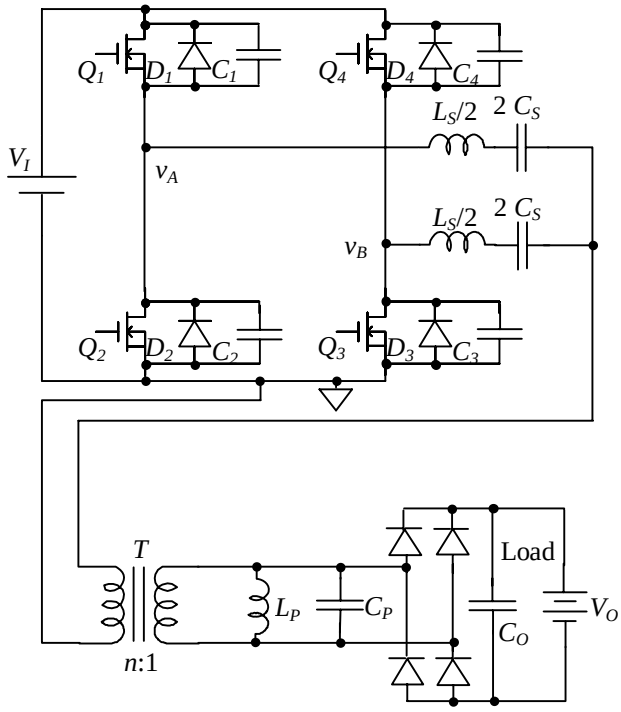

Fig. 5-1. Isolated full-bridge parallel-load series-parallel resonant converter with capacitive output filter and battery load.

As usual, the inverter bridge consists of the controlled switches, Q_1, Q_2, Q_3 and Q_4, their intrinsic antiparallel diodes, D_1, D_2, D_3 and D_4, and the capacitors, C_1, C_2, C_3 and C_4. The resonant network consists of three separate resonant tank circuits: the two L_S /2, 2C_S series tanks and the L_P, C_P parallel tank. The dc input voltage is supplied by the voltage source V_I and the battery load is represented by the voltage source, V_O.

The gate drive, inverter leg and inverter output voltages are shown in Fig. 5-2. In the PCPL converter, Q_1 through Q_4 are gated with 50% duty cycles, neglecting the dead-time, t_D. The gatings of Q_3 and Q_4 are delayed by an angle, ϕ, corresponding to

time interval t_ϕ, relative to the gatings of Q_2 and Q_1, respectively, resulting in the square-wave pole voltages v_A and v_B relative to the negative dc link rail, as shown in Fig. 5-2. The transitions of v_A and v_B are synchronized with the negative transitions of their respective gate drives, as occurs in zero-voltage switching (ZVS) operation. The input voltage, v_I, shown in Fig. 5-2, is the Thevenin equivalent voltage source of the inverter and can be shown to be the average of v_A and v_B. This is a key distinction between the series- and parallel-load converters. In the series-load converter, the input voltage, v_I, is the difference between v_A and v_B.

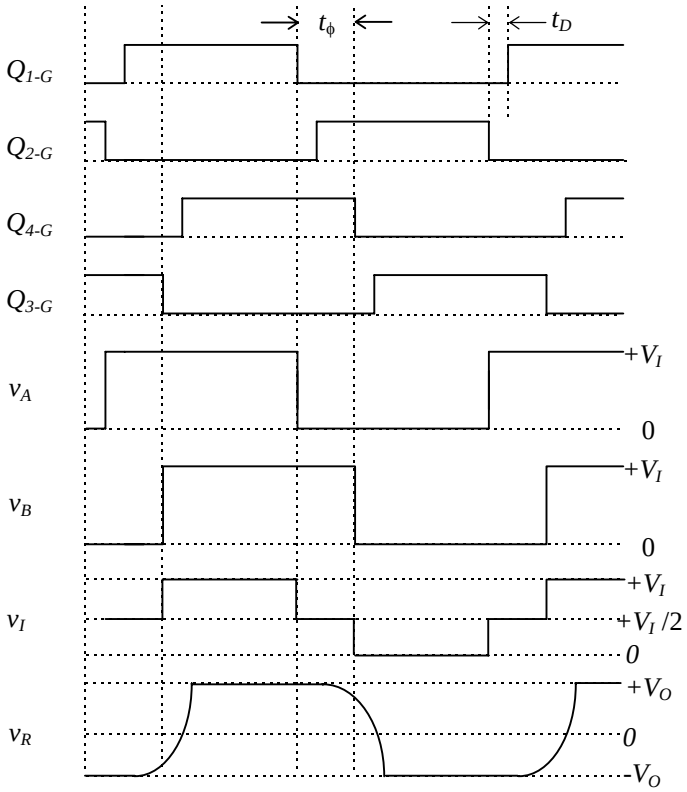

Fig. 5-2. Gate drive signals, $Q_{1\text{-}G}$, $Q_{2\text{-}G}$, $Q_{3\text{-}G}$ and $Q_{4\text{-}G}$, inverter leg output voltages, $v_A(t)$ and $v_B(t)$, inverter output voltage, $v_I(t)$, and rectifier voltage, $v_R(t)$.

The basic operation of the converter can be summarized as follows. At full load, v_A and v_B are equal in magnitude and phase, resulting in a square wave voltage v_I and the same power is transferred from each pole to the rectifier. The load power is regulated by delaying v_B relative to v_A. This has two effects on the basic circuit operation. As the phase control angle ϕ is increased, v_A moves further out of phase with the rectifier voltage v_R, and v_B moves further into phase with v_R. Thus, the voltage difference between v_B and v_R will decrease, reducing the series current and

the output power transferred from v_B to the load. Eventually, the phase difference between v_B and v_R will be such that there is no power transfer from v_B to the load. Thus, ϕ is increased, v_B starts to sink resonant current from v_A. Increasing ϕ further results in v_B sinking so much current that the current to the load and the parallel tank is reduced to zero. At this point, v_A and v_B are 180° out of phase.

Thus, the converter can regulate power to the load by increasing the phase control angle ϕ, while maintaining soft-switching over the complete load range.

5.3. RCFMA ANALYSIS

RCFMA Analysis has already been demonstrated in Chapters Three and Four to provide an accurate analysis of both the frequency- and phase-controlled series-load converters. In this section, the application of RCFMA Analysis to the PCPL converter is investigated.

5.3.1. Equivalent Circuit

Three equivalent circuits for the PCPL converter are shown in Fig. 5-3. The simplified time-domain circuit is shown in Fig. 5-3(a) and the pole voltages are represented by square-wave voltage sources, $v_A(t)$ and $v_B(t)$, where the negative dc link rail is the reference point. The input voltages are filtered by the passive elements of the resonant tanks and the resulting voltage across the parallel tank is rectified and fed to the dc battery load. The fundamental mode equivalent circuit is shown in Fig. 5-3(b). The circuit can be simplified further to the Thevenin equivalent circuit of Fig. 5-3(c) in which

$$\mathbf{v_I} = \frac{\mathbf{v_A} + \mathbf{v_B}}{2} \tag{5-1}$$

and

$$\frac{Z_S(\omega)}{4} = j\left(\frac{\omega L_S}{4} - \frac{1}{4\omega C_S}\right) \tag{5-2}$$

As shown previously in Chapter Four, the input voltage, $v_I(t)$, the rectifier voltage, $v_R(t)$, and the rectifier current, $i_R(t)$, are approximated by the phasors, $\mathbf{v_I}$, $\mathbf{v_R}$ and $\mathbf{i_R}$, respectively, whose magnitude and phase are those of their respective fundamental components. Similarly, the pole square-wave voltage sources, $v_A(t)$ and $v_B(t)$, are represented by the sine wave voltage source phasors, $\mathbf{v_A}$ and $\mathbf{v_B}$, whose

magnitude and phase are equal to the fundamental components of $v_A(t)$ and $v_B(t)$, respectively.

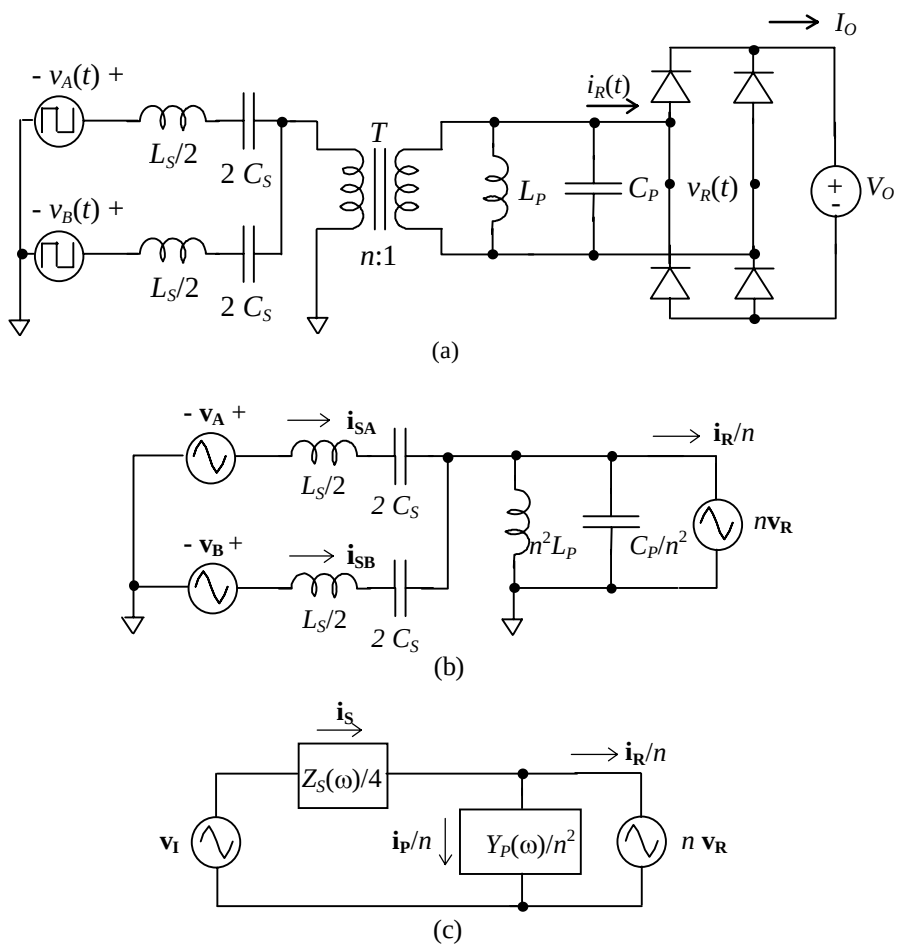

Fig. 5-3. Simplified time-domain and RCFMA equivalent circuits.

5.3.2. RMS and Phase Relationships

The rectifier voltage and current factors, K_V and K_A, and their respective phase angles, δ_V and δ_A, were derived in Chapter Three, and are used here in the analysis of the PCPL converter. The phase angles are calculated with respect to the inductor current, the reference phasor defined in the two-element circuit of Chapter Three.

The following assumptions are made:

(1) The instantaneous Thevenin input voltage, $v_I(t)$, can be represented by a phase-controlled quasi-square wave, as shown in Fig. 5-4.

The rms value of the fundamental component of $v_I(t)$, is therefore

$$V_{Irms} = \frac{\sqrt{2}}{\pi} V_I \cos\frac{\phi}{2} \tag{5-3}$$

The input voltage phasor, $\mathbf{v_I}$, to the resonant tank circuits is then defined as:

$$\mathbf{v_I} = V_{Irms}\angle\delta_I \tag{5-4}$$

where δ_I is the phase angle of $\mathbf{v_I}$.

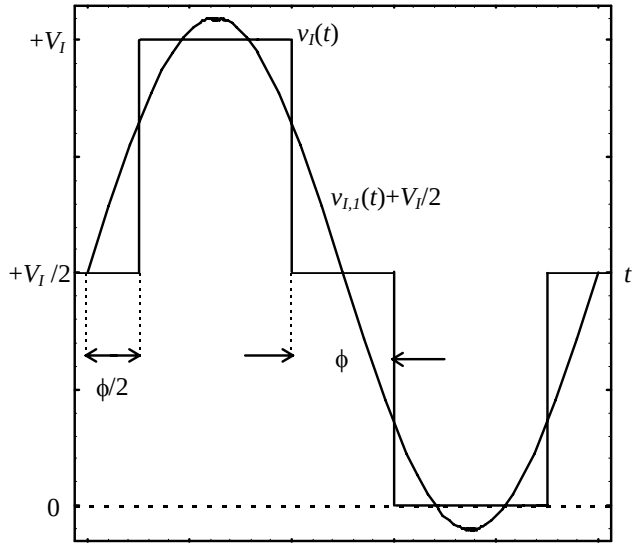

Fig. 5-4. Input voltage, $v_I(t)$ and fundamental component, $v_{I,1}(t)$.

It can easily be seen in the voltage phasor diagram of Fig. 5-5 that voltages $\mathbf{v_A}$ and $\mathbf{v_B}$ lead and lag the inverter input voltage $\mathbf{v_I}$ by an angle $\phi/2$ and are given by:

$$\mathbf{v_A} = \frac{\sqrt{2}}{\pi}V_I\angle\left(\delta_I + \frac{\phi}{2}\right) \tag{5-5}$$

and

$$\mathbf{v_B} = \frac{\sqrt{2}}{\pi}V_I\angle\left(\delta_I - \frac{\phi}{2}\right) \tag{5-6}$$

(2) The rectifier voltage, $v_R(t)$, is assumed to be a clamped quasi-square wave of amplitude V_o so that the rectifier voltage phasor is

$$\mathbf{v_R} = K_V V_O\angle\delta_V \tag{5-7}$$

(3) The current, $i_R(t)$, into the rectifier bridge is assumed to be a segment of a sine wave with an average value equal to I_o so that the rectifier current phasor is

$$\mathbf{i_R} = K_A I_O\angle\delta_A \tag{5-8}$$

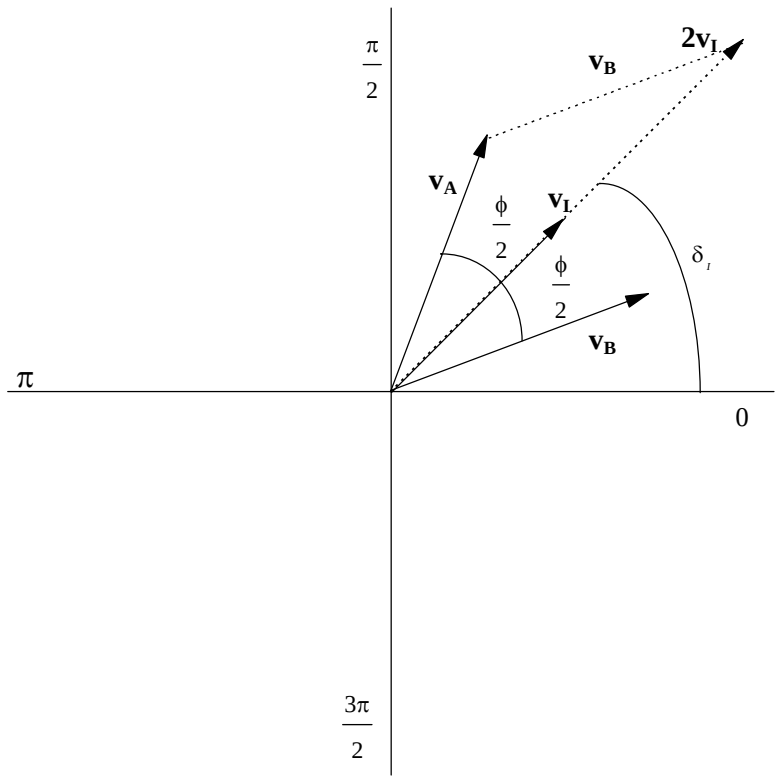

Fig. 5-5. Voltage phasor diagram.

5.3.3. Circuit Equations

From the fundamental mode equivalent circuit of Fig. 5-3(c), a relationship between the input voltage, $\mathbf{v_I}$, the rectifier voltage, $\mathbf{v_R}$, and the rectifier current, $\mathbf{i_R}$, can be derived:

$$\mathbf{v_I} = \left\{1 - \frac{1}{4n^2} Z_S(\omega) Y_P(\omega)\right\} n\mathbf{v_R} + j\frac{1}{4n} Z_S(\omega) \frac{\mathbf{i_R}}{n} \tag{5-9}$$

The basic converter equation (5-9) can easily be related to the corresponding equations for the series-load converter. In fact, the above equation is actually the same as equation (4-9) for the series load converter equation if the input voltage and turns ratio of the series-load converter are halved. This relationship is understandable because at full load with zero phase shift, the Thevenin input voltage for the parallel load converter is half of the actual input voltage for the series-load converter, making it necessary to use a 1:2 step-up ratio in the coupling transformer to output the same power for a given output voltage. Thus, the converter equations illustrate that the parallel-load and series-load converters are part of the same generic series-parallel resonant converter family.

As usual, the scalars $Z_S(\omega)$ and $Y_P(\omega)$ represent the characteristic impedance and characteristic admittance of the series and parallel branches, respectively, and are defined by:

$$Z_S(\omega) = \frac{\omega}{\omega_{OS}}\left(1 - \frac{\omega_{OS}^{\ 2}}{\omega^2}\right)Z_{OS} \tag{5-10}$$

and

$$Y_P(\omega) = \frac{\omega}{\omega_{OP}}\left(1 - \frac{\omega_{OP}^{\ 2}}{\omega^2}\right)Y_{OP} \tag{5-11}$$

where ω_{OS} and Z_{OS} are the resonant frequency and characteristic impedance of the series tank, and ω_{OP} and Y_{OP} are the resonant frequency and characteristic admittance of the parallel tank and ω is the operating frequency of the converter.

The currents in the series tanks, as indicated in Fig. 5-3(b), are given by

$$\mathbf{i_{SA}} = \frac{\mathbf{v_A} - n\mathbf{v_R}}{jZ_S(\omega)/2} \tag{5-12}$$

and

$$\mathbf{i_{SB}} = \frac{\mathbf{v_B} - n\mathbf{v_R}}{jZ_S(\omega)/2} \tag{5-13}$$

The basic RCFMA circuit equation in phasor form can be derived by substituting (5-4), (5-7) and (5-8) into (5-9):

$$\frac{\sqrt{2}}{\pi}V_I \cos\frac{\phi}{2}\angle\delta_I = \left[1 - \frac{1}{4n^2}Z_S(\omega)Y_P(\omega)\right]K_V n V_O \angle\delta_V + j\frac{Z_S(\omega)}{4}K_A\frac{I_O}{n}\angle\delta_A \tag{5-14}$$

Expressing (5-14) in trigonometric notation gives

$$\begin{aligned}\frac{\sqrt{2}}{\pi}V_I \cos\frac{\phi}{2}(\cos\delta_I + j\sin\delta_I) = &\left[1 - \frac{1}{4n^2}Z_S(\omega)Y_P(\omega)\right]K_V n V_O(\cos\delta_V + j\sin\delta_V) \\ &+ j\frac{Z_S(\omega)}{4}K_A\frac{I_O}{n}(\cos\delta_A + j\sin\delta_A)\end{aligned} \tag{5-15}$$

Equating the real and imaginary components gives

$$\begin{aligned}V_I \cos\frac{\phi}{2}\cos\delta_I = &\frac{\pi}{\sqrt{2}}K_V\left[1 - \frac{1}{4n^2}Z_S(\omega)Y_P(\omega)\right]nV_O\cos\delta_V \\ &- \frac{\pi}{4\sqrt{2}}K_A Z_S(\omega)\frac{I_O}{n}\sin\delta_A\end{aligned} \tag{5-16}$$

$$\begin{aligned}V_I \cos\frac{\phi}{2}\sin\delta_I = &\frac{\pi}{\sqrt{2}}K_V\left\{1 - \frac{1}{4n^2}Z_S(\omega)Y_P(\omega)\right\}nV_O\sin\delta_V \\ &+ \frac{\pi}{4\sqrt{2}}K_A Z_S(\omega)\frac{I_O}{n}\cos\delta_A\end{aligned} \tag{5-17}$$

Squaring the above two equations and adding gives

$$\left(V_I \cos\frac{\phi}{2}\right)^2 = \left(\frac{\pi}{\sqrt{2}}K_V\right)^2 \left\{1-\frac{1}{4n^2}Z_S(\omega)Y_P(\omega)\right\}^2 (nV_O)^2 + \left\{\frac{\pi}{4\sqrt{2}}K_A Z_S(\omega)\right\}^2 \left(\frac{I_O}{n}\right)^2 + \frac{\pi^2}{4}K_V K_A Z_S(\omega)\left\{1-\frac{1}{4n^2}Z_S(\omega)Y_P(\omega)\right\}\sin(\delta_V-\delta_A)V_O I_O \quad (5\text{-}18)$$

Equation (5-18) is the basic circuit equation and can be used to develop design characteristics for the converter.

5.3.4. Converter Characterization

Normalized output current, I_{ON}, is plotted against normalized operating frequency, ω_N, in Fig. 5-6 for different values of normalized output voltage. As shown in Fig. 5-6, increasing the phase control angle, ϕ, reduces I_{ON} but ϕ does not have to be increased over its full modulation range to reduce the current to zero. Clearly, the maximum ϕ required for zero load current increases as V_{ON} decreases and varies from approximately 92° at V_{ON} = 1.25 to 130° at V_{ON} = 0.75.

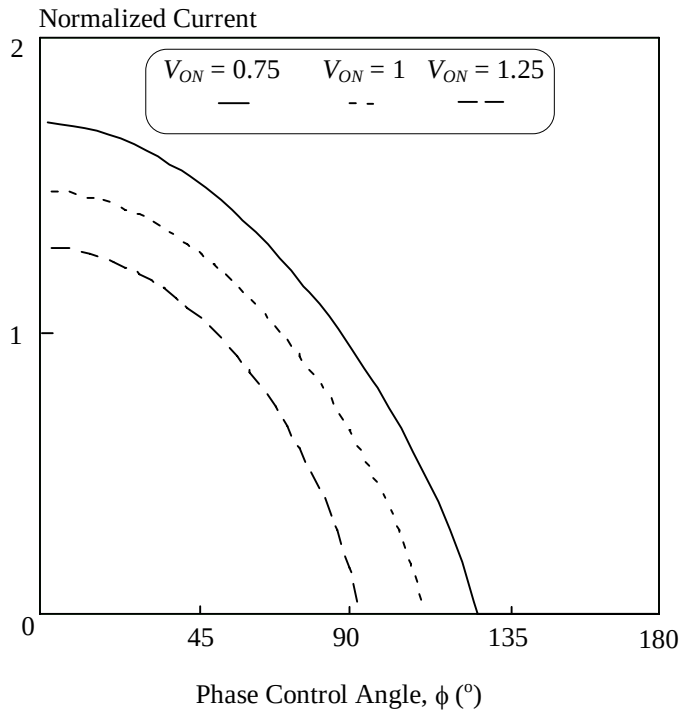

Fig. 5-6. RCFMA plots of normalized output current, I_{ON}, as a function of ϕ for various V_{ON}, at ω_N = 1.5, ω_{SN} = 0.5, ω_{CN} = 2 and n = 0.5.

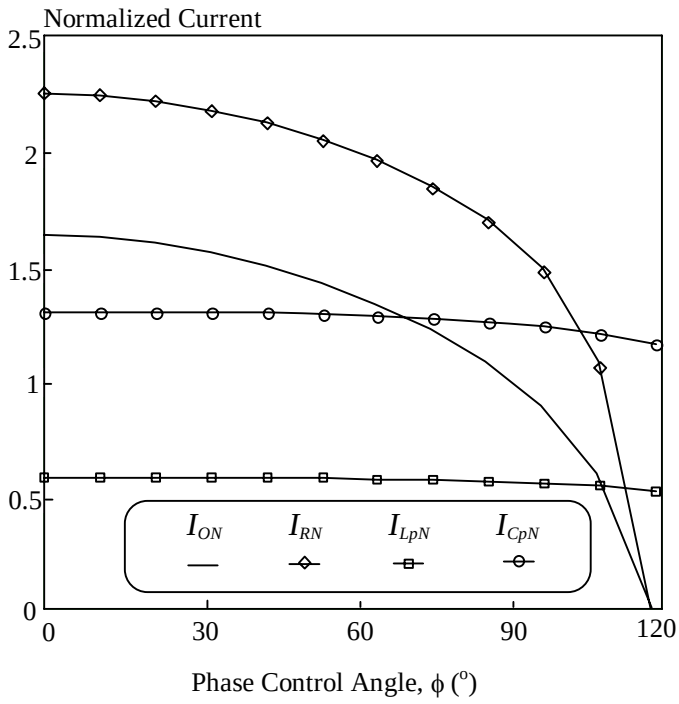

Fig. 5-7. RCFMA plots of normalized currents, I_{ON}, I_{RN}, I_{LpN}, and I_{CpN} as a function of ϕ at V_{ON} = 1, ω_N = 1.5, ω_{SN} = 0.5, ω_{CN} = 2 and n = 0.5.

The normalized output current, I_{ON}, the rms rectifier current, I_{RN}, the rms parallel capacitor current, I_{CpN} and the rms parallel inductor current, I_{LpN} are plotted in Fig. 5-7 as a function of phase control angle, ϕ. As ϕ is increased, I_{ON}, and, consequently, I_{RN}, are reduced to zero. The parallel tank currents I_{CpN} and I_{LpN} are nearly constant due to the relatively minor variation of rectifier voltage during power transfer.

The series current is the sum of the rectifier and parallel currents:

$$\mathbf{i_S} = \frac{\mathbf{i_R} + \mathbf{i_P}}{n} \tag{5-19}$$

When $\mathbf{i_S}$ is known, $\mathbf{v_I}$ can easily be determined. The phase angle, δ_I, of the input voltage, $\mathbf{v_I}$, is given by

$$\mathbf{v_I} = V_{Irms} \angle \delta_I \tag{5-20}$$

Knowing δ_I, the pole voltages and currents and their respective phase angles can be constructed from (5-5), (5-6), (5-12) and (5-13). The power factor angles, δ_{LA} and δ_{LB}, of the series currents in each leg relative to their respective poles voltages are given by

$$\delta_{LA} = \delta_I + \frac{\phi}{2} - \delta_{SA} \tag{5-21}$$

$$\delta_{LB} = \delta_I - \frac{\phi}{2} - \delta_{SB} \tag{5-22}$$

The power factor angle in leg B, δ_{LB}, is plotted against frequency in Fig. 5-8 for various values of phase control angle, ϕ. Angle δ_{LB} must be maintained positive in order to achieve zero-voltage switching of the MOSFETs in leg B. Clearly, for the values shown, δ_{LB} is positive over the operating frequency range illustrated for $1 \le \omega_N \le 3$. In these plots, δ_{LB} has significant margin at the full-power frequency of ω_N =1.5. This is very different from the PCSL converter analyzed in Chapter Four which develops a negative δ_{LB} and loses ZVS as ϕ increases for $\omega_N < \omega_{CN}$. From these results, it appears that the PCPL converter can be operated over a wide frequency range and yet maintain ZVS over the full range.

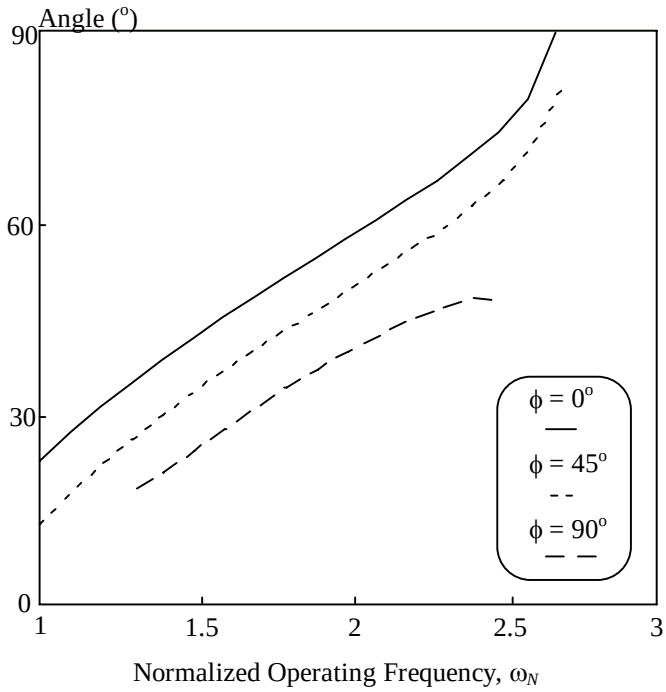

Fig. 5-8. RCFMA plots of power factor angle δ_{LB} as a function of ω_N for various ϕ at V_{ON} = 1, ω_{SN} = 0.5, ω_{CN} = 2 and n = 0.5.

The normalized series tank current and transistor currents are shown in Fig. 5-9. As ϕ increases, the rms series current, I_{SBN}, rms transistor current, I_{QBN}, and turn-off current, I_{QBON}, in pole B all initially decrease, bottom out and then increase as the converter becomes lightly loaded. On the other hand, the rms series current, I_{SAN}, rms transistor current, I_{QAN}, and turn-off current, I_{QAON}, in pole A all initially increase to a peak and then decrease as the converter becomes lightly loaded. Clearly both legs

will maintain ZVS provided that the turn-off currents are sufficient to charge and discharge the drain-source capacitances during the gate drive dead time.

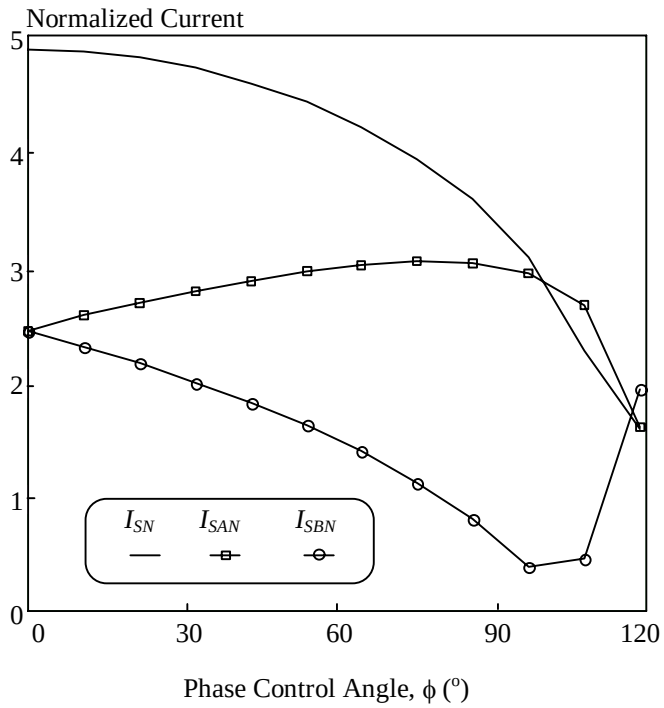

(a)

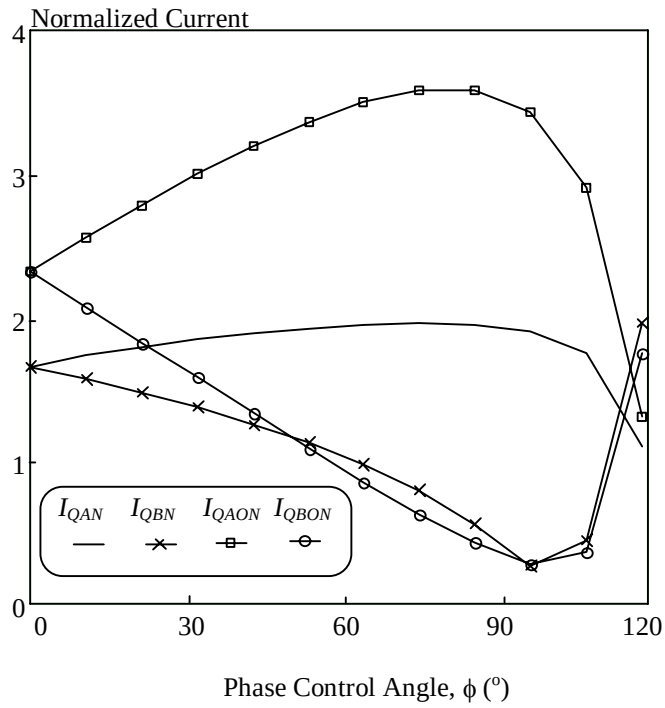

(b)

Fig. 5-9. RCFMA plots of normalized currents for (a) I_{SN}, I_{SAN}, and I_{SBN} and (b) I_{QAN}, I_{QBN}, I_{QAON}, and I_{QBON} as a function of ω_N at $V_{ON} = 1$, $\omega_N = 1.5$, $\omega_{SN} = 0.5$, $\omega_{CN} = 2$ and $n = 0.5$.

5.4. EXPERIMENTAL VALIDATION

A MOSFET-based prototype converter has been built and experimentally tested. The converter is designed to be SAE J-1773 compatible. The basic design requirements of the converter are to output 1 kW at 250V and at a minimum frequency of 150 kHz. The converter has the following parameters:

V_I = 200 V

f_{OS} = 27 kHz

f_{OP} = 119 kHz

f_C = 185 kHz

Y_{OP} = 0.03 S

n_P = 2

n_S = 4

These parameters are exactly the same as those for the FCSL and PCSL converters except for n_P which was 4 for the series-load converters. All three converter types output the same power for the given voltage and frequency.

Experimental waveforms for phase control angles of 0° and 72° are shown in Fig. 5-10(a-d). Initially, the converter is operating at full power with $\phi = 0^o$, as shown in Fig. 5-10(a, b). These waveforms are almost identical to those for the FCSL converter. The only significant differences are that v_I has half the magnitude compared to the FCSL converter, and has a dc offset equal to $V_I/2$. The pole voltages and currents, shown in Fig. 5-10(b), are identical due to the zero phase shift angle. Note that the current waveforms exhibit some slight differences due to asymmetries in the current probes. The actual leg currents i_{SA} and i_{SB} should ideally be identical waveforms with exactly half the amplitude of i_S.

Increasing the phase control angle to 40% of the modulation range, or $\phi = 72^o$, gives the waveforms shown in Fig. 5-10(c) and (d). The increased ϕ causes v_A and v_B to move out of phase with each other, resulting in the phase-shifted v_I, which is the instantaneous average of v_A and v_B. As v_B moves into phase with v_R, the current i_{SB} is reduced while i_{SA} increases.

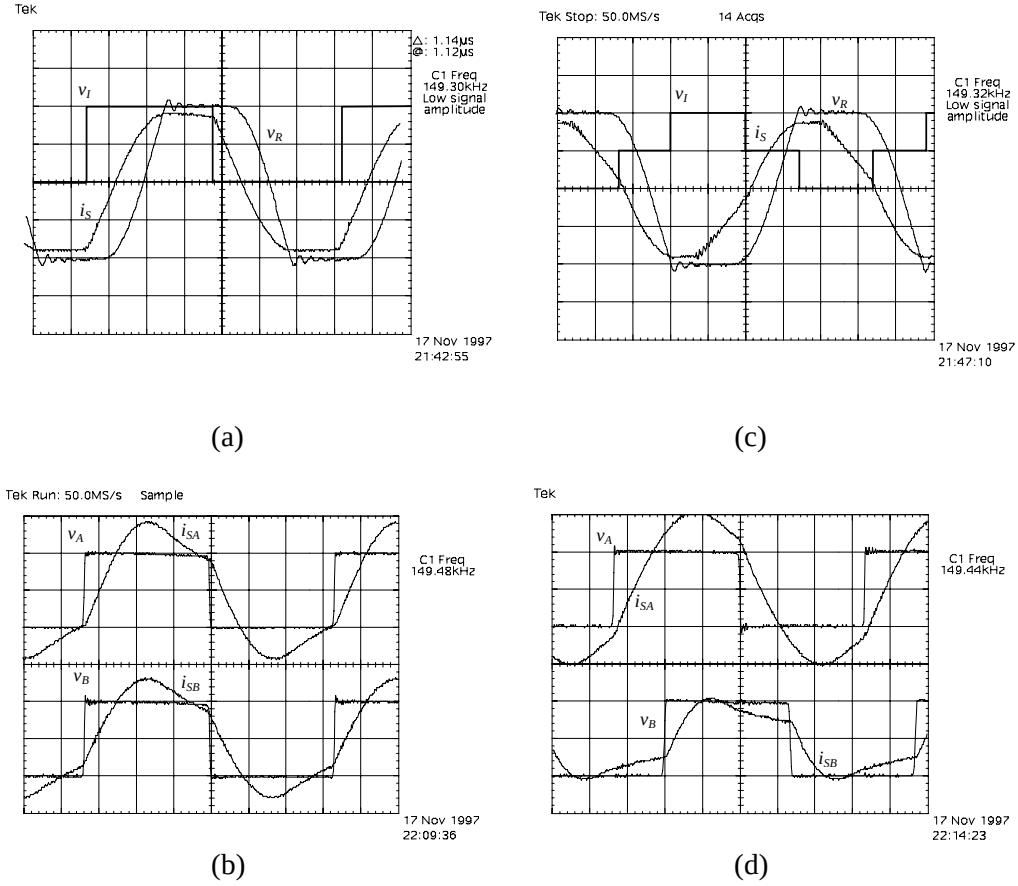

Fig. 5-10. Experimental waveforms, v_I, v_R and i_S, for (a) $\phi = 0^o$ and (c) $\phi = 72^o$ and their respective pole voltages and currents, v_A, v_B, i_{SA}, and i_{SB} for (b) $\phi = 0^o$ and (d) $\phi = 72^o$ at V_O = 200 V. (Scale: 100V/div., (a,c) 10A/div., (b,d) 5A/div.)

Increasing ϕ to 108° results in i_{SB} almost going to zero as shown in Fig. 5-11(a). However, the inductive nature of the series tank results in a lagging current with a significant magnitude at turn off, thereby allowing zero-voltage transitions at switch turn-on and turn-off, As ϕ increases further, i_{SB} actually begins to increase. Finally, at $\phi = 180^o$, as shown in Fig. 5-11(b), there is no net current flowing into the parallel tank and load, and the currents, i_{SA} and i_{SB}, are equal and opposite.

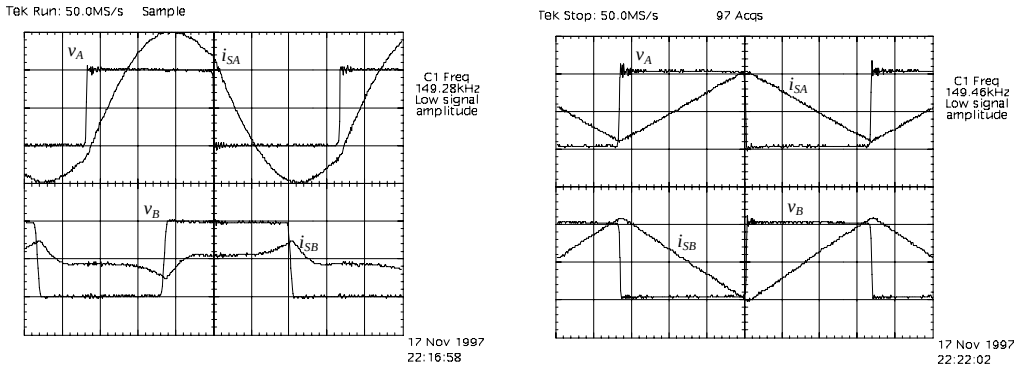

(a) (b)

Fig. 5-11. Experimental waveforms, v_A, v_B, i_{SA} and i_{SB}, for (a) $\phi = 108^o$ and (b) $\phi = 180^o$ at $V_O = 200$ V. (Scale: 100V/div. (a) 5A/div., (b) 10A/div.)

The principal converter currents are experimentally measured and compared with analytical results predicted by the RCFMA Analysis in Fig. 5-12(a-c). The data plots show good correlation. Initially, at low values of ϕ, the RCFMA data are greater than the measured results. The error is easily accounted for by the converter inefficiency, measurement error and the basic limitations of the RCFMA Analysis. As ϕ is increased to 90°, the errors are typically reduced to zero because the RCFMA currents decrease faster than the experimental currents. The more rapid reduction in the RCFMA currents is due to the fact that its estimation of the rectifier voltage factor K_V is too large. This overestimation of K_V results in an increased v_R with a consequent reduction in the currents flowing between the inverter and the rectifier. The advantages of using the simplified K_V calculation, as derived in Chapter 3, are that the estimation is simple, closed-form and is reasonably accurate in generating converter characteristics. In contrast to the reasonable accurate RCFMA calculations of the output and series currents, RCFMA Analysis generally underestimates the turn-off currents over the load range because these currents are significantly affected by the harmonic nature of the waveforms, which is obviously not factored into the RCFMA Analysis. Thus, RCFMA Analysis predicts a slightly negative I_{QBO}, while the experimental data is always positive.

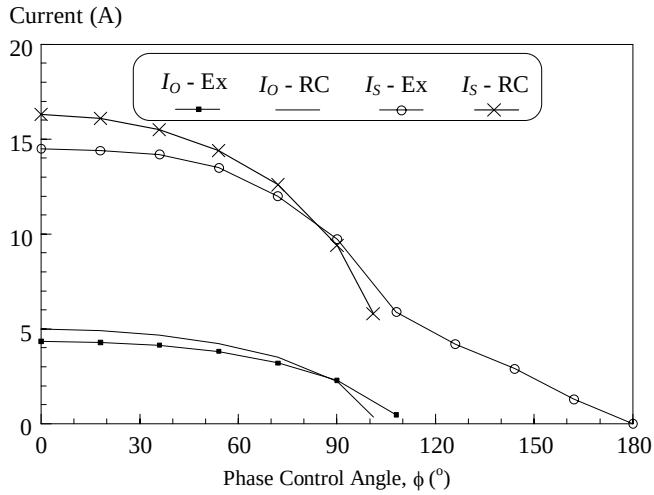

(a)

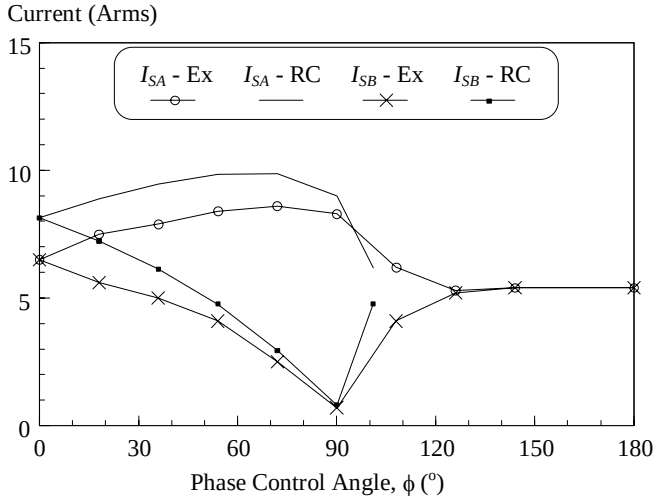

(b)

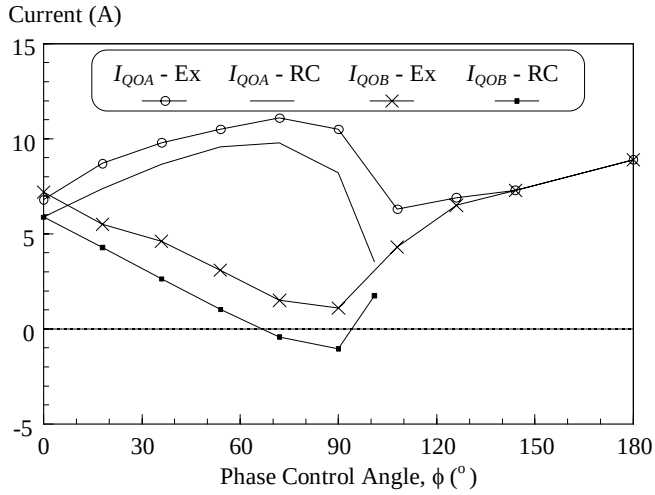

(c)

Fig. 5-12. Comparison of RCFMA (RC) and experimental (Ex) for (a) output and rms series currents, I_O and I_s, (b) rms series pole currents, I_{SA} and I_{SB}, and (c) transistor turn-off pole currents, I_{QOA} and I_{QOB}, as a function of ϕ, at V_O = 250 V.

The converter currents generated by RCFMA Analysis can be used to calculate the converter power losses if the power dissipation parameters of the components are known. Fig. 5-13 shows a comparison of measured and calculated power loss over the output power range and good correlation is evident at high power levels. At about the half-power point, RCFMA Analysis predicts greater losses than the measured losses. Again, this divergence can be explained by the overestimation in RCFMA Analysis of the rectifier voltage, and the resulting overestimation of the inductive coupling transformer core loss. As the output power decreases and the inverter losses fall significantly, this core loss is by far the largest loss component.

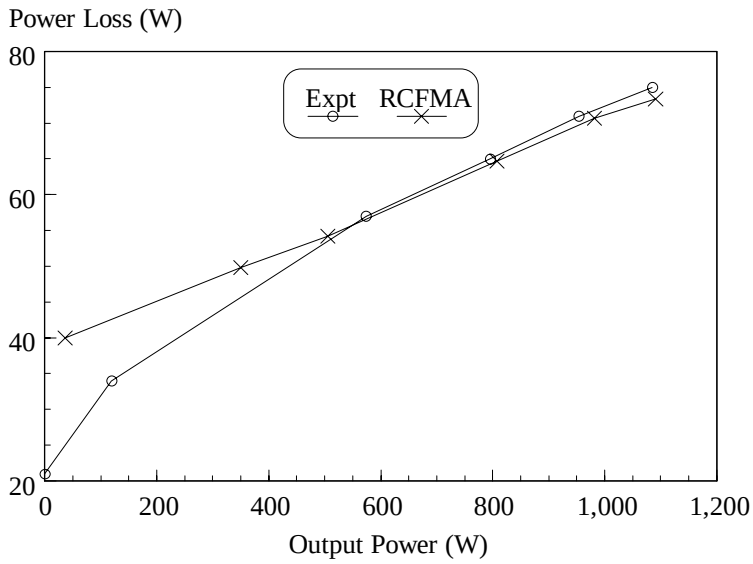

Fig. 5-13. Comparison of experimental and RCFMA converter power loss versus output power for V_o = 250 V.

5.5. COMPARISON OF THE FREQUENCY- AND PHASE-CONTROLLED SERIES-PARALLEL RESONANT CONVERTERS

Three different series-parallel resonant converters have been investigated in this thesis. The frequency-controlled series-load (FCSL) converter was analyzed in Chapters Two and Three. The hybrid frequency and phase-controlled series-load (HCSL) converter was proposed in Chapter Four. The phase-controlled parallel-load (PCPL) converter has now been studied in this chapter. The three converters have many positive characteristics in common, most notably:

1. Utilization of leakage inductance.
2. Zero-voltage switching,
3. High-frequency operation.
4. Buck-boost voltage gain.
5. Current-source capability.
6. Monotonic power transfer over a wide load range.
7. Throttling capability down to no-load.
8. High efficiency
9. Inherent short-circuit protection.
10. Soft recovery of output rectifiers.
11. Secondary dv/dt control.

However, significant differences do exist between the converters in the areas of power loss, number of transformer primary turns, frequency range, pole current asymmetry and vehicle inlet stress, as discussed below.

1. Power Loss

A plot of converter power losses for the FCSL, HCSL and PCPL converters is shown in Fig. 5-14. The experimental results show that the PCPL converter is significantly more efficient than the series-load converters over much of the load range. However, the PCPL is lossier at full-load due to the higher power dissipations in the cable and primary. These experimental results indicate that an optimized PCPL converter could be the most efficient stage for the battery charging of an EV over the charge cycle if the cable and primary dissipations are reduced (at increased cost, of course).

The FCSL and HCSL converters have the same losses over much of the load range, as shown in Fig. 5-14, but the HCSL has lower power losses under light load conditions, which is important for long term low power trickle charging of the battery.

2. Vehicle Inlet Stress

The low-frequency operation of the PCPL converter results in reduced vehicle inlet stresses with reduced load and this is reflected in the low light-load power losses in Fig. 5-14. This is not the case in the FCSL and HCSL converters where partial load operation occurs at high frequencies resulting in large resonant currents in the passive components of the vehicle inlet. These currents stress the vehicle inlet, resulting in increased vehicle inlet power dissipation and reduced vehicle inlet efficiency over the load range.

3. Frequency Range

This is the key distinction between the series and parallel-load converters. The PCPL converter can operate at a constant frequency whilst the FCSL and HCSL converters both have wide frequency ranges, resulting in bulky gate drives, more costly high-frequency magnetics, high component stress and increased costs for electro-magnetic compliance. The HCSL converter achieves a frequency range reduction of about 30-40% compared to the FCSL converter.

4. Primary Turns

The PCPL converter has increased cable and primary currents, compared to the HCSL and FCSL converters, because of the effective doubling of current in the primary due to the reduced primary turns necessary to achieve voltage gain. However, the increased stresses on the cable and primary are not proportionally greater because of the low-frequency operation of the PCPL converter.

5. Pole Current Asymmetry

This is a major negative characteristic of the PCPL converter compared to the series-load converters. As power is reduced in the PCPL converter, the

pole currents diverge significantly and lose symmetry. This asymmetry complicates the design of the inverter bridge and may result in increased electro-magnetic problems due to the loss of balanced switching between the poles. The FCSL converter is completely symmetric, while the HCSL converter also loses symmetry, but not to the same extent as the PCPL converter.

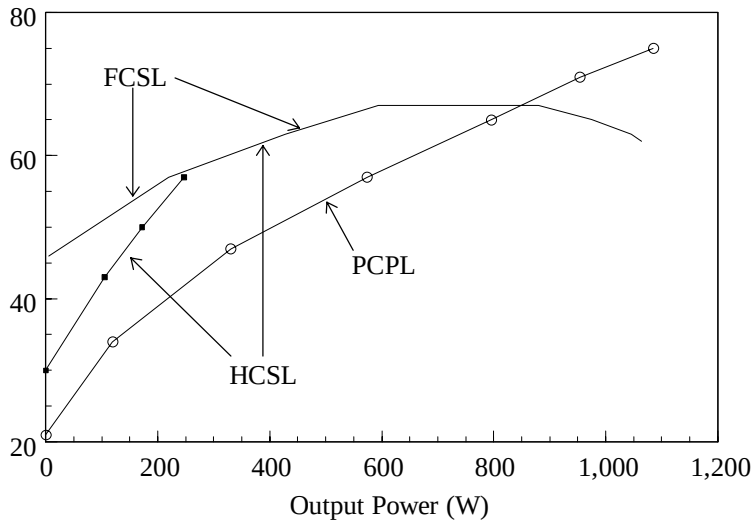

Fig. 5-14. Comparison of measured converter power loss versus output power for PCPL, FCSL, and HCSL converters.

5.6. CONCLUSIONS

In this chapter, the application of phase control to the parallel-load series-parallel resonant converter, with capacitive output filter and battery load, was investigated. The converter was analyzed and its steady-state operating characteristics obtained using RCFMA Analysis. Experimental and analytical results show that the converter has many of the important characteristics of the closely related frequency-controlled, series-load converter. In addition, the converter implements soft-switching over the entire load range, resulting in high full-load and partial-load efficiencies. This feature, combined with the constant-frequency phase control operation, make the converter an excellent option for the inductive coupling application. Experimental results are obtained using a 1 kW, 250 V, SAE J-1773 compatible prototype. Good correlation is achieved between the analytical and experimental results.

In summary, the both theory and experiment show that the converter has the following advantages.

1. Constant-frequency operation.
2. ZVS over the full-load range.
3. Fixed EMI spectrum.
4. Minimum losses over the modulation range.
5. Zero vehicle inlet losses at no-load.

The principal disadvantages are the large asymmetry in pole currents and the large cable and primary current stresses.

REFERENCES

See Chapter Four references.

6.

CHAPTER SIX

OPERATION AND ANALYSIS OF NOVEL SINGLE-STAGE SERIES-PARALLEL RESONANT INDUCTIVE CHARGER

Abstract: A novel single-stage power-factor-corrected ac-dc converter is now introduced. The Single-stage Series-Parallel Resonant (SSPR) Converter uses the current-source characteristic of the series-parallel topology to provide power factor correction over a wide output power range from zero to full load. The new converter topology is derived from the frequency-controlled series-parallel resonant converter, discussed in Chapter Two, and has all the advantageous characteristics of its dc-dc counterpart. Simulation and experimental results verify the operation of the new converter.

6.1. INTRODUCTION

The proliferation of utility-connected power electronic converters has spurred the demand for products which limit the total harmonic distortion (THD) and maximize the power factor of the currents sourced from the utility. Power factor corrected utility interfaces are of prime importance in the electric vehicle industry. The complete energy conversion cycle of the electric vehicle (EV) must convert electrical power from the utility to mechanical power at the drive axle as efficiently and as economically as possible. The EV battery charger must ensure that the utility current is drawn at unity power factor in order to minimize line distortion and maximize the real power available from the utility outlet.

The industry standard approach to power factor correction is to use a two-stage ac-dc power converter. The first stage is typically a boost preregulator which simultaneously regulates the dc link voltage level and the line current waveshape. The second stage can be any one of a number of different types of resonant or PWM dc-dc converters. The General Motors EV1 inductive battery charger is a two stage converter featuring a boost preregulator and the full-bridge resonant converter described in Chapter Two.

While two-stage approaches to power factor correction and power regulation have proliferated, the power supply industry has shown interest in developing single-stage solutions with the desire to reduce the parts count and cost of the conversion stages [1-4].

As the inductive coupling technology matures, it is critical that new approaches be examined which may result in reduced cost of the power converter. Market acceptance of electronic products has always been dependent on reducing the cost to the customer. Among the avenues explored for cost reductions in inductive charging is the use of single-stage converters. The use of an active-clamp phase-shifted boost converter was investigated in [4]. The converter has a low parts count but has been shown to have a number of significant problems. The converter is not compatible with SAE J-1773 and loses soft switching if used to drive the vehicle inlet. Additionally, even if the inlet did not have the parallel capacitor and were configured as a “PWM-friendly” transformer, the converter would still have some major problems. The poorly distributed IGBT switching losses increase significantly with battery voltage and the increased leakage inductance, resulting in high mechanical and electrical costs. Also, although the EMI characteristics of the PWM topology have not been examined in detail, it is likely that the cost of achieving compliance could be far more significant than those associated with resonant converters, due to the hard-switched nature of the waveforms.

The resonant characteristics of the parallel and series-parallel resonant converters make these types of converter ideal candidates for single-phase power factor correction [1]. As explained in [1], the series-parallel converter can function as a parallel resonant converter at the valley of the line voltage where high voltage gain and low output current are required. At the peak of the line voltage, the series resonant nature of the converter is ideal as it outputs high current at low voltage gain. Steigerwald shows in [1] that the power factor can be increased to varying levels by using either passive or active control. In this chapter, it is shown that the series-parallel resonant converter draws a square-wave line current if passive constant-frequency control is used, and active variable-frequency control results in a purely sinusoidal line current being drawn from the utility. A single-stage converter, which outputs a pulsating $\sin^2$ current into the battery, may be a very logical choice for battery charging because the absence of converter energy storage components

reduces the size, weight and cost of the converter compared to its two-stage counterpart.

The series-parallel topology has been demonstrated to be ideally suited to inductive coupling applications in Chapter Two. Configuring the series-parallel resonant dc-dc converter into its single-stage counterpart results in the Single-stage Series-Parallel Resonant (SSPR) converter, which has the same advantageous characteristics as its dc-dc counterpart, but additionally provides power factor correction over a wide load range. The SSPR Converter is different from the converter studied in [1] because of its capacitive rather than inductive output filter.

The converter is described and its operation is discussed in Section 6.2. A 6.6kW design example is used to illustrate the converter operation. The basic theory is validated using a PSPICE simulation in Section 6.3. Results from an experimental prototype are presented and discussed in Section 6.4.

6.2. Converter Description and Operation

The SSPR converter power and control stages are shown in Fig. 6-1. The off-vehicle part of the SSPR converter consists of a line rectifier block, D_L, a small high-frequency non-electrolytic bus filter capacitor, C_B, a MOSFET-based full-bridge inverter, a lumped two-element series resonant tank composed of an inductance, L_S, and a capacitance, C_S, and a cable and paddle. The transformer, parallel capacitor, C_P, high-frequency rectifier, capacitive filter and battery load, are all located on the vehicle.

As usual, the full bridge consists of the controlled switches, Q_1, Q_2, Q_3 and Q_4, their intrinsic antiparallel diodes, D_1, D_2, D_3 and D_4, and the snubber capacitors, C_1, C_2, C_3 and C_4, to facilitate zero-voltage-switching.

The control of the converter is relatively simple and is outlined as follows. The ac line voltage is rectified and attenuated to provide the rectified sinusoidal reference current waveshape. This signal is then multiplied by the dc power command and the product is the desired current reference. The feedback signal is the dc link current which is fed back through the current amplifier. The current feedback is compared with the reference and the error is fed into a compensator network. The compensated error is the input to a voltage to frequency converter which provides

the basic gating signal for the switches, Q_1 to Q_4, of the full-bridge inverter. The converter regulates the output power by modulating the operating frequency.

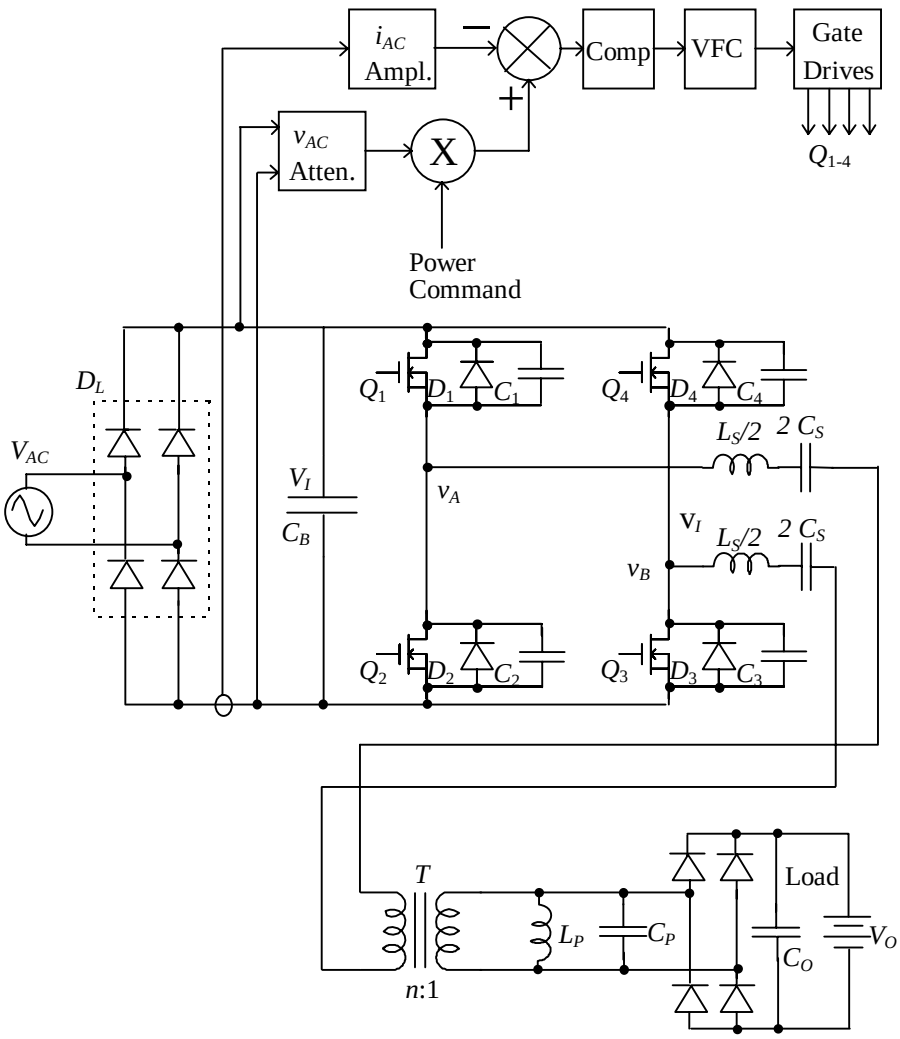

Fig. 6-1. Single-stage series-parallel resonant converter power and control stages.

6.2.1.Theory of Operation

In the SSPR converter, the bus capacitance is very small and the dc link voltage is effectively the rectified line voltage. There is no large-scale energy storage in the converter and the instantaneous value of input power must be equal to the instantaneous output power over the utility line cycle. Thus,

$$v_{AC} i_{AC} = V_O i_O \tag{6-1}$$

where v_{AC} and i_{AC} are the instantaneous input line voltage and current, respectively, and V_o and i_o are the output voltage and current, respectively.

The theory governing the operation of the frequency-controlled series-parallel converter has been established in Chapters Two and Three, where the concept of the current-source frequency was developed. Using the basic Fundamental Mode Approximation analysis, it was shown that the converter has the following charging characteristic at the current source frequency, f_C.

$$i_O(f_C) = n\frac{8}{\pi^2}\frac{|v_{AC}|}{Z_S(f_C)} \tag{6-2}$$

where i_O is the dc output current, $|v_{AC}|$ is the dc link voltage and Z_S is the series impedance. At f_C, i_O is dependent upon the series tank parameters and v_{AC} only, and is independent of the output voltage, V_O.

Combining equations (6-1) and (6-2) gives a new equation for the line current when the converter is operated at the current-source frequency.

$$|i_{AC}(f_C)| = \frac{8}{\pi^2}\frac{nV_O}{Z_S(f_C)} \tag{6-3}$$

Thus, theoretically, if no frequency modulation is introduced and the converter is operated at the current-source frequency only, the converter will ideally source a square-wave current from the utility which is dependent only on the reflected output voltage and the series tank impedance at the current-source frequency. Clearly this current is independent of the input voltage and, hence, can be drawn from the utility even at the zero-crossing of the line voltage. The ideal relationship between the averaged input and output voltage and current waveforms is illustrated in Fig. 6-2 for operation at the current-source frequency. It is obvious from these waveforms that the topology is capable of implementing displacement factor correction as the input voltage and input current are in phase. However, the input current is ideally a square wave and consequently has a relatively high THD, which reduces the power factor. Hence, instantaneous frequency variation about the current-source frequency as a function of the sinusoidal input voltage, must be employed to shape the current in a sinusoidal manner so as to reduce the THD and achieve a power factor close to unity.

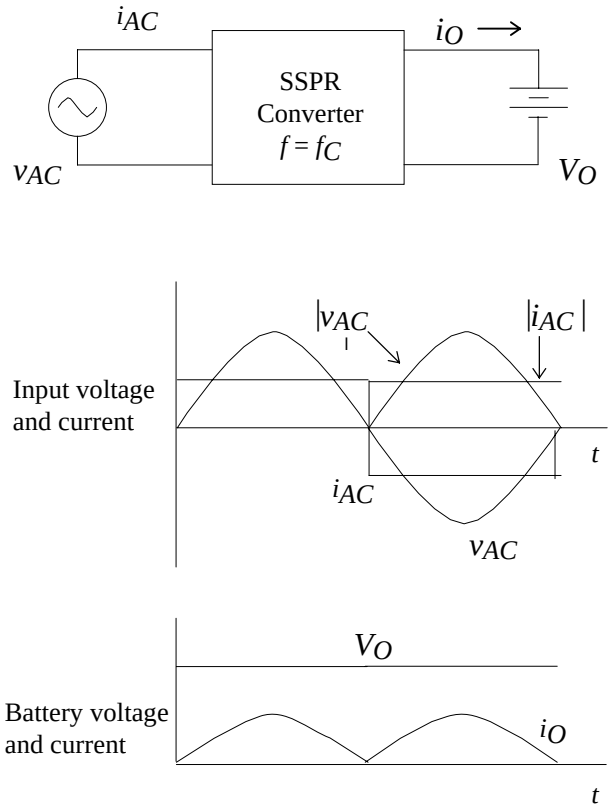

Fig. 6-2. Converter block diagram and basic waveforms operating at the current-source frequency.

Decreasing the frequency below f_c results in increased output current at a lower converter voltage gain. This condition is required at the peak of the line voltage when the converter functions largely as a series converter. Increasing the frequency above f_c will result in reduced output current while maintaining high converter voltage gain. This is the desired converter operation at the valley of the line voltage when the converter largely functions as a parallel converter.

The waveshaping potential of the SSPR converter under sinusoidal steady-state operation can be illustrated and explored by a more detailed analysis of the converter. Firstly, the maximum line current as a function of line voltage is determined for a given battery voltage. A typical plot of such normalized line currents and voltages, generated using the Modal Analysis of Chapter Two, is plotted in Fig. 6-3. When the line voltage is close to the zero crossing, the converter can source a maximum line current equal to the current source level as determined by (6-3). As the line voltage increases along its sinusoidal trajectory, the maximum possible line current with variable-frequency control also increases from the current-source level. As seen in Fig. 6-3 the current increases to a maximum value at the

peak of the line voltage. Thus, the curved line in Fig. 6-3 represents the maximum line current that the converter can source as the instantaneous line voltage increases. The frequency can be modulated to regulate for any current level below the maximum. The two straight lines to the origin are loci for a power-factor-corrected current. The converter achieves PFC by regulating the line current directly proportional to the line voltage. Clearly, because the zero voltage offset for the maximum available current is always greater than zero, the locus for a PFC current is always within the controlled area for the converter as long as the peak commanded current is equal to or less than the maximum design current.

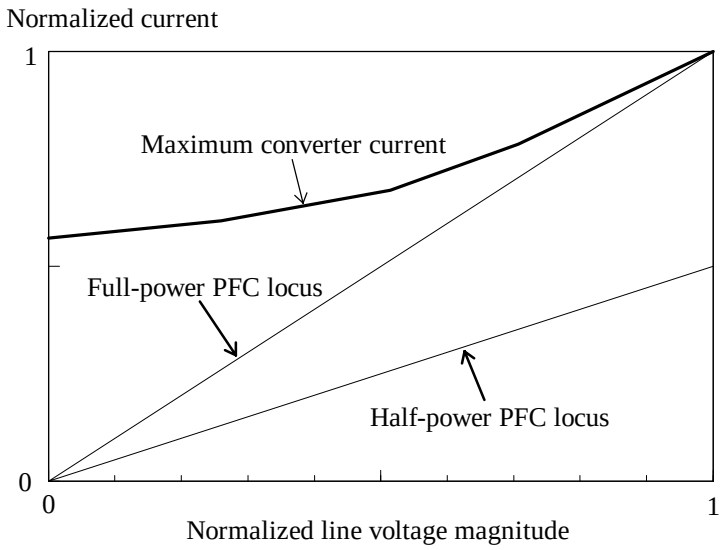

Fig. 6-3 Typical maximum converter current and PFC current loci as a function of instantaneous normalized line voltage for a given battery voltage.

The waveshaping nature of the SSPR converter will be further explored and illustrated by using the design example in the next section.

6.2.2. Design Example

Mathematical software design tools have been developed in the previous chapters for the frequency-controlled series-parallel converter. These tools will now be used to facilitate the design of a single-stage converter. Firstly, the design requirements for the sample converter must be stated. The requirements are based on a single-phase 220V, 30 A utility line feed supplying rated power to a Nickel Metal-Hydride battery pack, which has a maximum power requirement at 430V. The frequency range of the converter is limited to 150 kHz to 300 kHz to minimize

component stress and to place limits on the electromagnetic noise sources within the converter. The converter must be SAE J-1773 compatible and have 4 primary turns to minimize current stresses. The specification can be summarized as follows:

line voltage	=	220 Vrms
line current	=	30 A rms
input power	=	6.6 kW
output voltage	=	430 Vdc
frequency range	=	150 - 300 kHz
primary turns	=	4
secondary turns	=	4

The peak input power for a PFC converter is twice the average input power and is thus 2 x 6.6 kW = 13.2 kW in this case. The peak power occurs at the peak of the line voltage which is √2 x 220 V = 311 V. Thus, the goal is to use the design tools derived in the previous chapters to determine the converter component values which will give the required power over the specified frequency range. Various analyses were run using both the time-based Modal approach and the frequency-based RCFMA technique. The results of these analyses are summarized in Fig. 6-4.

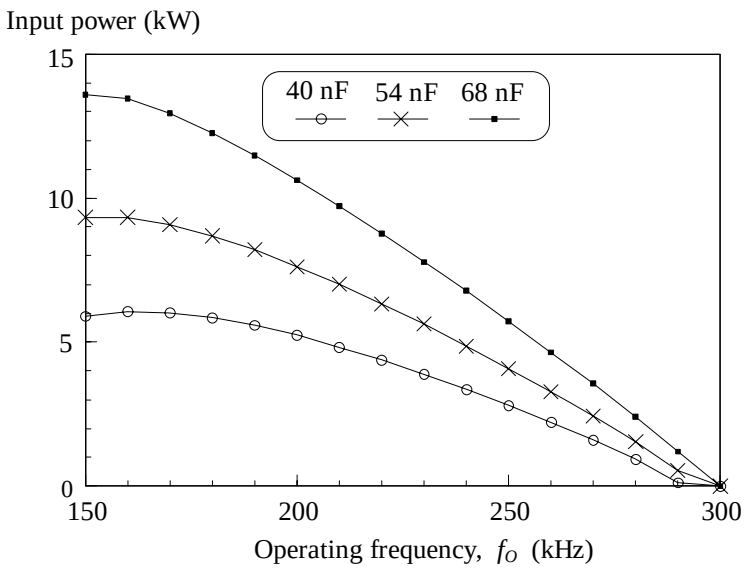

Fig. 6-4. Input power, P_I, as a function of f_O for V_{ACPK} = 311 V and V_O = 430 V.

Maintaining the parallel capacitance, C_P, at 40 nF a specified in the J-1773 specification results in a limited output power of about 6 kW maximum. The maximum output power can be increased by reducing the primary turns from 4 to 3 but this results in significantly increased primary conduction losses. The power can also be increased by increasing the value of C_P. Ideally, the additional capacitance would be placed in the vehicle inlet but this would violate the SAE J-1773 standard. Thus, the capacitance must be placed in the paddle or at the output cable connection. This additional capacitance is maintained at a minimum because it will cause secondary resonances with the leakage inductances of the port and the cable, possibly introducing instabilities.

Increasing the capacitance to a value of 68 nF, an increase of 70%, enables the power to be regulated from almost 14 kW to zero within the specified frequency range. The following are the component values for the optimized converter.

$$f_{OS} = 100 \text{ kHz}$$
$$f_{OP} = 91 \text{ kHz}$$
$$f_C = 230 \text{ kHz}$$
$$Y_{OP} = 0.039 \text{ S}$$

or

$$L_S = 10\ \mu\text{H}$$
$$C_S = 0.25\ \mu\text{F}$$
$$L_P = 45\ \mu\text{H}$$
$$C_P = 68 \text{ nF}$$

The maximum converter line current and the full-power PFC locus are plotted in Fig. 6-5. In this case, the current source level is about 24 A while the maximum input current is 43 A at the peak line voltage of 311 V. The converter should function as a PFC stage for any power level less than 6.6 kW average.

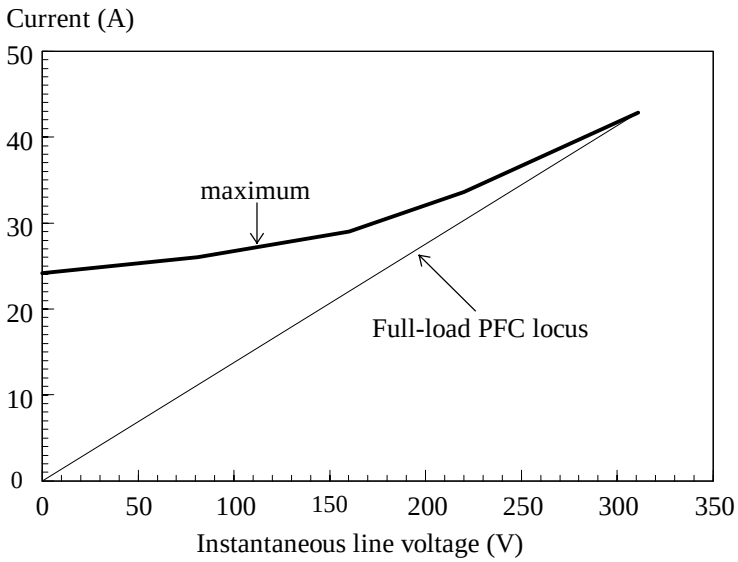

Fig. 6-5. Maximum converter current and full-load PFC current locus as a function of instantaneous line voltage for the design example.

Converter input power as a function of operating frequency is plotted in Fig. 6-6 for various values of the instantaneous ac input voltage. As before, the rms input voltage is 220V and at $\theta = 90^o$ has a peak value of 311V. As expected, at the zero-crossing of the line voltage, approximated here by $\theta = 3^o$ or $v_{AC}(\theta) = 17$ V, the converter operates close to the current-source frequency of 230 kHz while the actual power level is low. Intermediate angles of $\theta = 15^o$ and $\theta = 45^o$ are also plotted. The thick line shows the trajectory of the input power versus frequency as the frequency is controlled to generate a sine-wave current at the input to the converter.

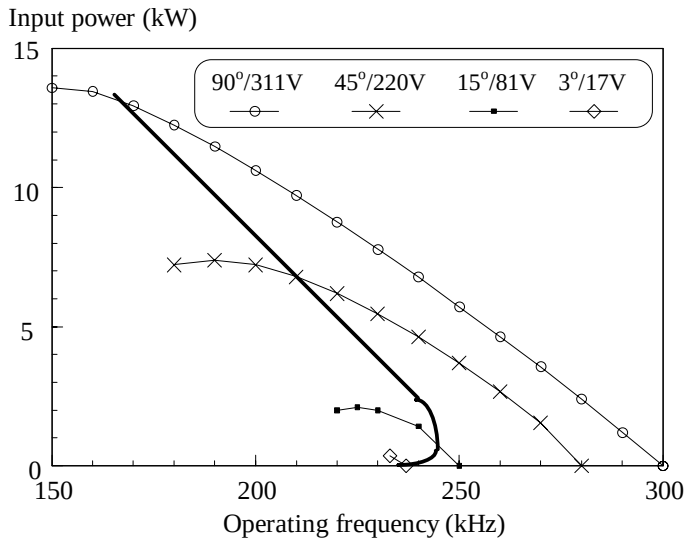

Fig. 6-6. Converter input power as a function of operating frequency for various values of instantaneous line voltage.

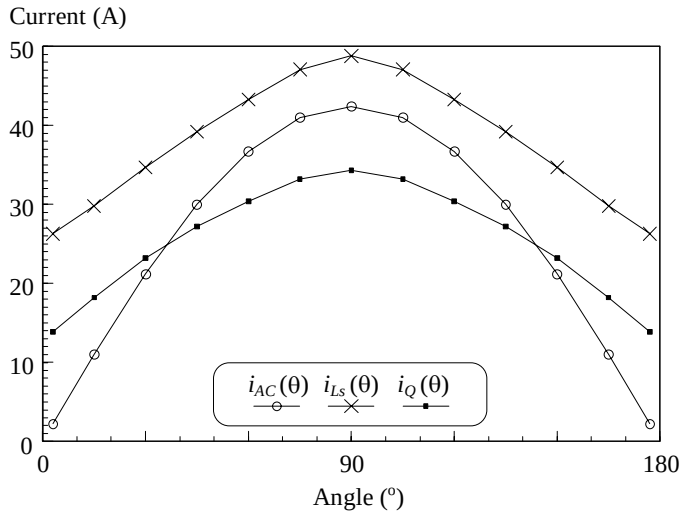

(a)

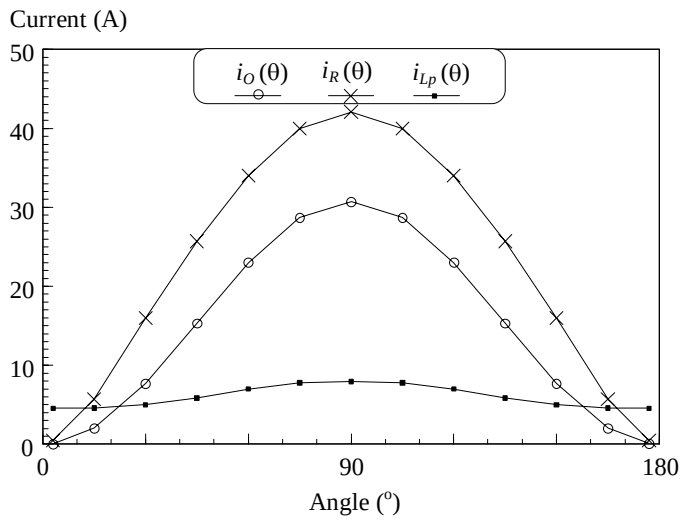

(b)

Fig. 6-7. Instantaneous converter currents (a) $i_{AC}(\theta)$, $i_{Ls}(\theta)$, and $i_Q(\theta)$, and (b) $i_O(\theta)$, $i_R(\theta)$, and $i_{Lp}(\theta)$, for unity power factor operation.

A more in-depth investigation of the principal converter currents results in the curves plotted in Fig. 6-7(a) and (b). These currents are calculated using Modal Analysis when the line current is varied sinusoidally for the sample converter design. The instantaneous rms currents in the series tank, $i_{LS}(\theta)$ and in the transistors, $i_Q(\theta)$, are plotted with the line current $i_{AC}(\theta)$ in Fig. 6-7(a). Current i_{LS} approximates to the current-source value at the valley and has a maximum value about 15% greater than that of $i_{AC}(\theta)$. Current $i_Q(\theta)$ varies from approximately half of $i_{LS}(\theta)$ at the valley to about 0.707 times $i_{LS}(\theta)$ at the peak.

The instantaneous rms currents in the output rectifier, $i_R(\theta)$, and in the magnetizing inductance, $i_{Lp}(\theta)$, are plotted with the dc output current $i_O(\theta)$ in Fig. 6-7(b). As expected, a sinusoidal control of the input current results in a $\sin^2$ waveform for $i_O(\theta)$. Current $i_R(\theta)$ varies in similar fashion to $i_O(\theta)$, while $i_{Lp}(\theta)$ varies from a minimum at the zero crossings of the input voltage to a maximum at the peak.

6.3. PSPICE VALIDATION

The controllability of the SSPR converter is demonstrated using PSPICE. The simulation schematic is shown in Fig. 6-8. To minimize component count, the circuit is simplified using Analog Behavioral Modeling blocks as shown. Consequently, the ac input current is not available and so the dc output current is regulated to generate a $\sin^2$ trajectory. The output current is fed into a 3 kHz RC filter after which it is compared with a $\sin^2$ waveform generated from the ac input voltage. The error is calculated and fed into an error clamp stage which limits the error amplitude and, consequently, the maximum possible frequency variation. The error is then fed into a voltage-controlled oscillator which acts as the proportional gain for the error amplification. The output frequency is used to gate the inverter stage which supplies high-voltage square waves to the resonant tanks.

Simulation waveforms are shown in Fig. 6-9. It is clear that the converter output current to the battery is a $\sin^2$ waveform, which closely follows the commanded $\sin^2$ reference. The peak current is shown to be about 29 A, resulting in an average output power of 0.5 x 29A x 430V = 6.24 kW. Thus, the simulation verifies to a reasonable approximation the theoretical prediction of output power.

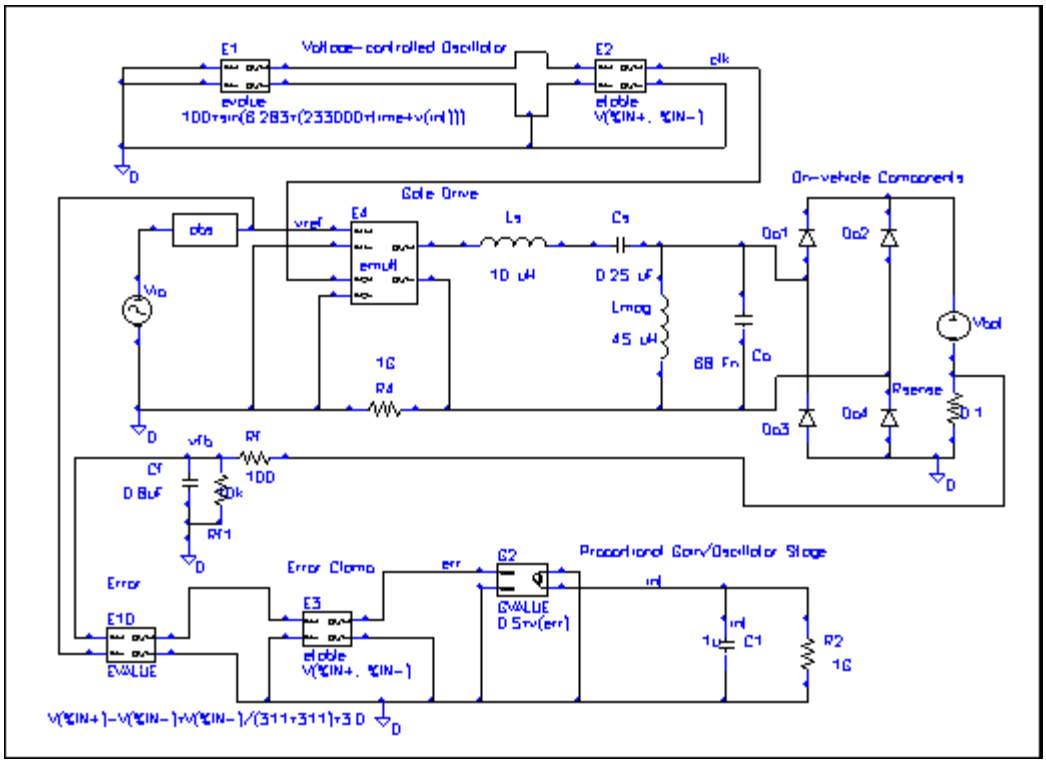

Fig. 6-8. PSPICE Schematic for validation of converter PFC operation.

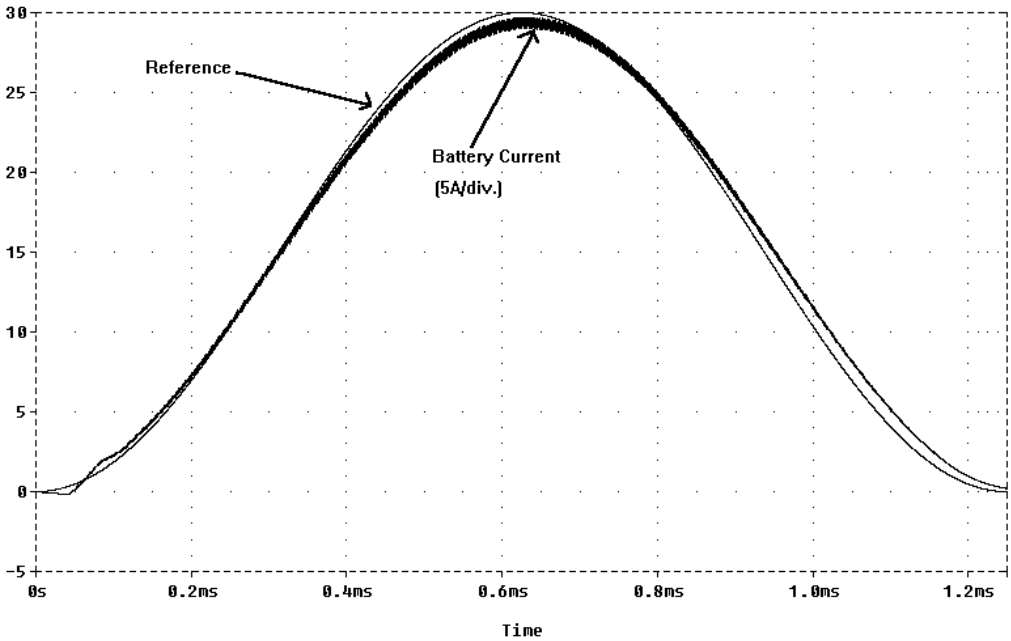

Fig. 6-9. PSPICE waveforms for Design Example.

6.4. EXPERIMENTAL RESULTS

A MOSFET-based prototype off-line converter with power factor correction has been built and experimentally tested. The converter is nominally designed to output 1 kW peak or 500W average for an input voltage of 150 Vac and a dc battery voltage of 200V. The converter has the following parameters:

f_{OS} = 27 kHz

f_{OP} = 119 kHz

f_C = 185 kHz

Y_{OP} = 0.03 S

and

L_S = 32 μH

C_S = 1.08 μF

L_P = 45 μH

C_P = 40 nF

n_P = 4

n_S = 4

Experimental waveforms for the converter are shown in Fig. 6-10 and Fig. 6-11. The first set of waveforms in Fig. 6-10 are for the restricted case in which the converter is operated at the current-source frequency. The input current, effectively a square wave, is as predicted by theory, with some distortion due to the inherent distortion in the input line voltage in the experiment.

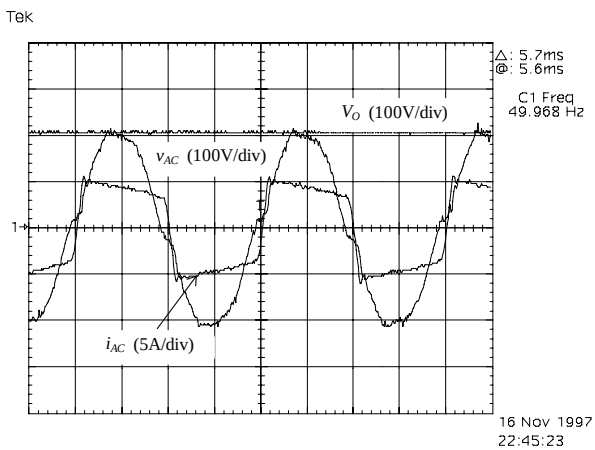

Fig. 6-10. Experimental waveforms for v_{AC}, i_{AC} and V_O operating at the constant-source frequency, f_C. (5 ms/div.)

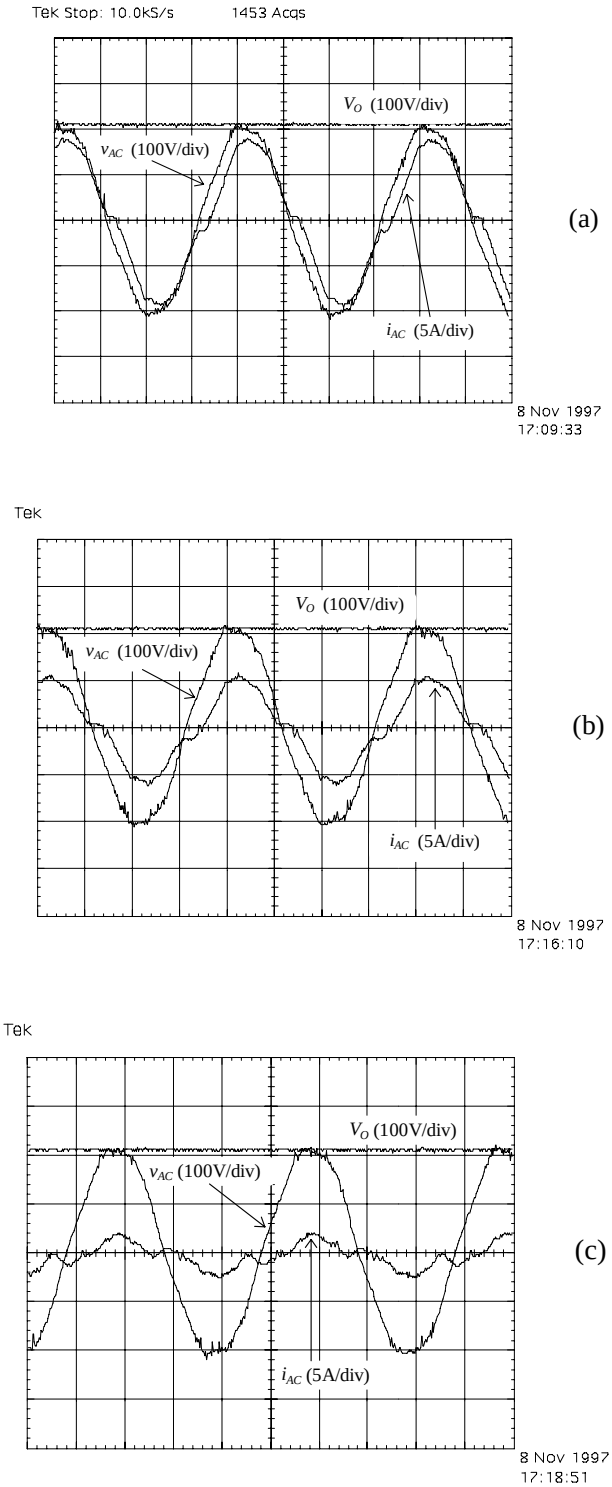

Fig. 6-11. Experimental waveforms for v_{AC}, i_{AC} and V_O using closed-loop control for I_{AC} equals (a) 2.5 Arms, (b) 1.5 Arms and (c) 0.5 Arms. (Scale: 5 ms/div.)

The experimental waveforms shown in Fig. 6-11(a)-(c) illustrate closed-loop operation based on the simple feedback circuitry outlined earlier. The input

currents are relatively clean sine waves with some cross-over distortion. Power factor correction by wave shaping of the line current is clearly being implemented at all power levels although distortion clearly increases at the lower input powers. This is due primarily to the impact of non-linearities in the control loop which should be considered in further work

Plots of analytical and experimental values for the operating frequency over the first quarter-cycle of the input voltage sine wave are shown in Fig. 6-12. The frequencies predicted by Modal Analysis show good correlation with those measured experimentally. The difference between the two can easily be accounted for by converter losses, measurement error and feedback loop steady-state error.

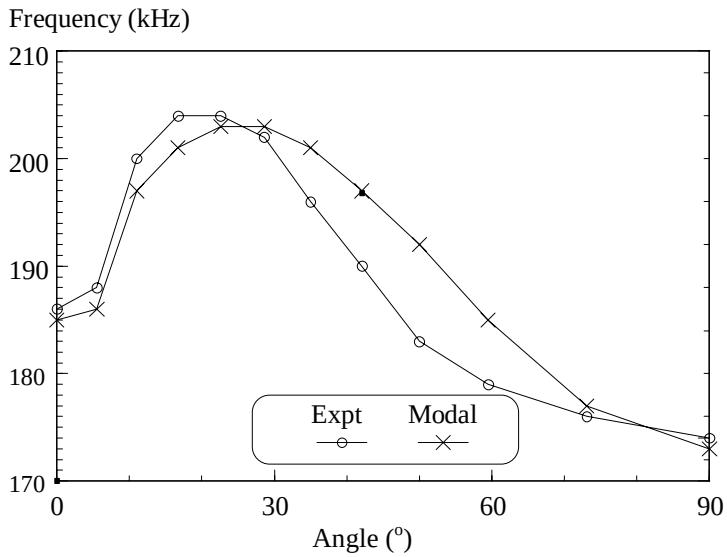

Fig. 6-12. Analytical and experimental values for operating frequency over 90° of the line cycle.

Measured power factor and efficiency are plotted for two output voltage levels in Fig. 6-13 and Fig. 6-14, respectively. At full power, the power factor approaches 0.995 and decreases as the power decreases. The power factor remains above 0.96 as the power approaches 100 W or about 20 % of rated power.

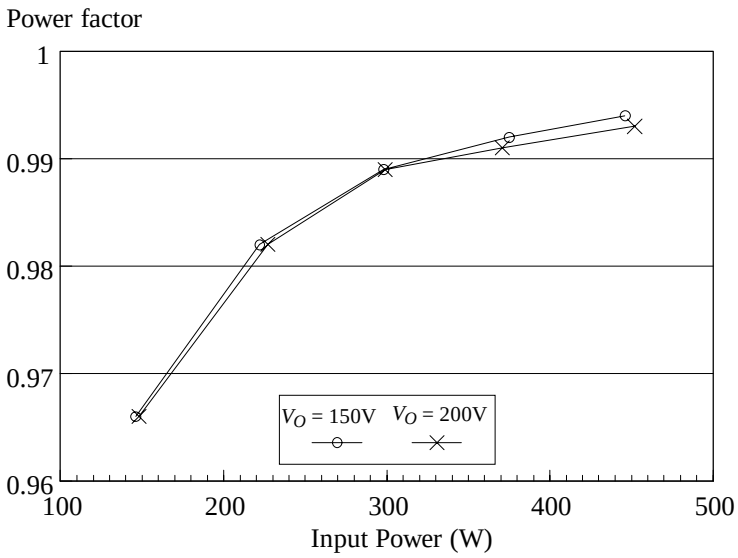

Fig. 6-13. Measured power factor as a function of input power.

The converter efficiency is measured as approximately 93% at 150V and 91.5% at 200V. Partial load efficiency remains high and is in the low to mid 70's at 100 W. As noted previously, maintaining high efficiency at light load is important for the EV charging application.

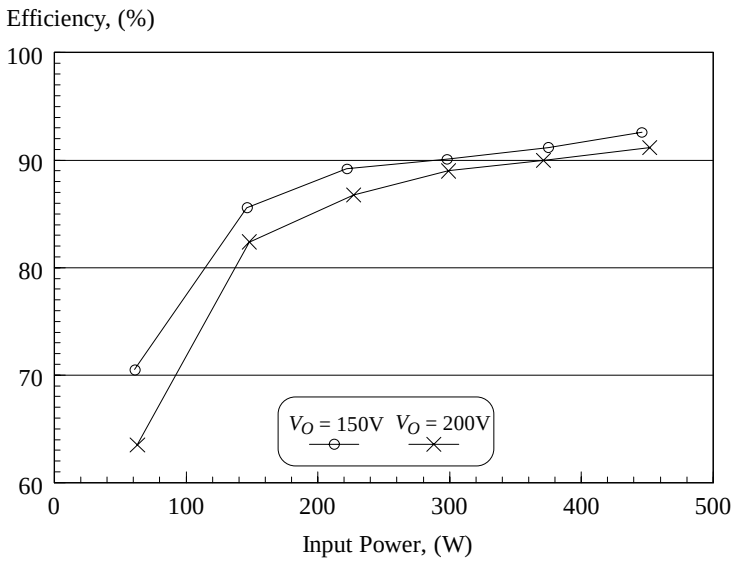

Fig. 6-14. Measured efficiency for the prototype converter as a function of input power.

A comparison of measured and calculated efficiencies for the prototype are shown in Fig. 6-15. Efficiency calculations are based on component data sheets and current values generated by the Modal Analysis program. The calculated and measured efficiencies show an excellent correlation over most of the load range. The error between the two curves at full load represents about 7W in a measured power

loss of 37W. Therefore the analysis is underestimating losses by about 20%. This discrepancy can easily be accounted for by many factors in both the analysis and experiment, e.g. measurement error. The error is reduced to about 2W at 150W input and increases below that power level.

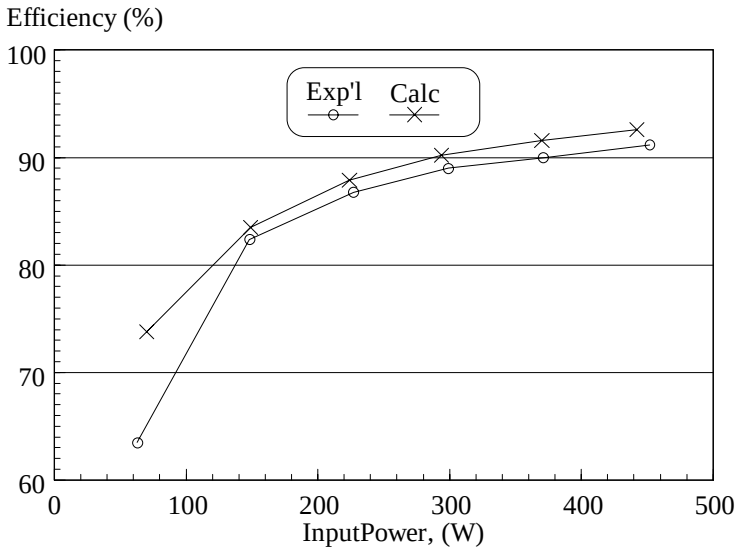

Fig. 6-15. Measure and calculated efficiencies as a function of input power for the prototype converter.

6.5. CONCLUSIONS

In this chapter, a novel single-stage power-factor-corrected ac-dc converter was introduced. The Single-stage Series-Parallel Resonant (SSPR) Converter uses the current-source characteristic of the series-parallel resonant topology to provide power factor correction over a wide output power range from zero to full load. The new converter topology is derived from the frequency-controlled series-parallel resonant converter, discussed in Chapter Two, and has all the advantageous characteristics of its dc-dc counterpart. The additional advantages of the single-stage converter can be summarized as follows.

1. Inherent power factor correction and output power regulation.
2. Soft-switched over the load range.
3. Increased converter reliability due to the elimination of the large electrolytic capacitors.

4. Inherent variation of the operating frequency over the line cycle, resulting in reduced EMI spectral amplitudes.

5. Reduced cost, parts count, complexity, weight and volume of the converter compared to the two-stage option.

The major disadvantage of a single-stage converter with its pulsating $\sin^2$ output current is that increased power handling is required with higher resonant currents and greater inverter and rectifier component losses than in the two-stage resonant converter.

On balance, the single-stage series-parallel resonant converter offers much promise as a competitive option to its two-stage counterpart, as indicated by the analytical, simulation and experimental results presented in this chapter.

REFERENCES

[1] M. Schutten, R. Steigerwald, M. Kheraluwala, "Characteristics of Load Resonant Converters Operated in a High Power Factor Mode", *IEEE Applied Power Electronics Conf.*, 1991, pp. 5-16.

[2] V. Belaguli, A. Bhat, "A Hybrid Resonant Converter Operated as a Low Harmonic Rectifier With and Without Active Control," *IEEE Power Electronics Specialists Conf.*, 1996, pp. 720-726.

[3] M. van der Berg, J. Ferreira, "A Family of low EMI, Unity Power Factor Converters," *IEEE Power Electronics Specialists Conf.*, 1996, pp. 1120-1127.

[4] R. Watson, F. Lee, "A Soft-Switched Full-Bridge Boost Converter Employing an Active-Clamp Circuit," *IEEE Power Electronics Specialists Conf.*, 1996, pp. 1948-1954.

CHAPTER SEVEN

CONCLUSIONS

In the Introduction to this thesis, the objectives were outlined as follows:

1. to analyze the frequency-controlled series-parallel converter,
2. to investigate phase control of the converter, and
3. to develop a lower cost single-stage topology.

These objectives have been achieved and the supporting studies are documented in detail in preceding chapters. In this final chapter, the work of the previous chapters will be summarized, the conclusions presented, and suggestions made for future work.

The first objective of the thesis was to analyze the frequency-controlled series-resonant converter driving the SAE J-1773 vehicle inlet. The combination of the two passive elements of the series-tank impedance with the two significant parallel elements of the inductive coupling vehicle inlet results in a four-element Series-Parallel LCLC (SP-LCLC) converter with a capacitive output filter. This fourth-order, multi-resonant topology has not previously been analyzed in the literature. The thesis develops two novel analytical approaches. The first approach is the time-domain Modal Analysis, discussed in Chapter Two, and the second is the frequency-domain Fundamental Mode Approximation (FMA) Analysis approach, discussed in Chapter Three.

The time-domain Modal Analysis of the multi-element converter is complex because of the converter's multi-resonant nature. The analysis requires the derivation of the swing equations describing each mode of operation. These equations are then transformed to two decoupled second-order equation sets which describe the behavior of the converter. A *Mathematica* program numerically solves the transcendental equation set, and can be used to characterize, design and optimize the inductive charger. Experimental results from a hardware prototype show excellent correlation with the analytical predictions.

Modal Analysis provides a very accurate characterization of the converter. However, it is mathematically complex, requiring a numerical solution to transcendental equations and does not yield a closed-form solution for the converter characteristics. Future work in this area could focus on the development of a unified Modal Analysis solution for the two, three and four-element series-parallel converter family. The computer-based methodology presented here should lend itself to the development of a generic program for the study of such converters.

In Chapter Three, the application of FMA Analysis to the converter is investigated. This frequency-domain analysis, employing a voltage source model of the load, provides a much simpler and more intuitive approach for the study of resonant converters. The FMA Analysis demonstrates key converter characteristics, but its accuracy is shown to be poor compared to Modal Analysis. A novel extension of the FMA Analysis, termed Rectifier-Compensated FMA Analysis, is developed with enhanced accuracy. It also provides a closed-form solution for the family of multi-element, multi-resonant converters used in the present application, and greatly simplifies the design procedure for the inductive charger.

The RCFMA Analysis has proven extremely useful as a design tool. Future work in this area could involve the development of new approximations for other circuit topologies with complex behavior. The RCFMA Analysis presented in Chapter Three is readily extended into the analysis of higher-order capacitively-filtered series-parallel resonant converters. The frequency-domain analysis also has potential for use in small-signal analysis of converters.

The second objective of this thesis is to investigate phase control concepts. In Chapter Four, the application of phase control to the standard inductive charging converter configuration is examined. The relatively simple RCFMA Analysis is extended to the phase-controlled converter and yields an insightful and relatively accurate characterization of the converter. The analysis demonstrates that while constant-frequency phase control is not feasible, a novel Hybrid Frequency and Phase Control strategy can be implemented, which features all the positive characteristics of frequency control but has reduced frequency range and improved light-load efficiency compared to frequency control only. The hybrid control scheme can advantageously be applied across the power spectrum in the inductive charging application. Further study should include the design of an integrated controller and

the investigation of the large and small-signal behavior of the converter when operated with this control strategy.

A literature survey of phase control options uncovered the phase-controlled converter presented in Chapter Five. This constant-frequency converter is configured with a parallel load and implements soft switching over the entire load range, resulting in high full-load and partial-load efficiencies. RCFMA Analysis and experimental results confirm the converter's potential to replace the frequency-controlled converter. However, the parallel-load converter has some negative characteristics, such as pole current asymmetry and high primary current stress, but is the only viable solution for a constant-frequency application. Future work in this area could involve further investigation of the applicability of the topology across the power spectrum. A very useful study would be an investigation of the electromagnetic interference of the converter compared to the frequency-controlled option.

The third objective of the thesis was to develop a single-stage inductive charger as a competitive option to the present EV1 two-stage converter. The earlier analysis of the frequency-controlled series-parallel resonant converter demonstrated that a key characteristic of the topology is its current-source nature. Thus, the converter is ideally suited for operation as a single-stage converter, providing both output power regulation and input current waveshaping. Chapter Six investigates and demonstrates the feasibility of this concept by analysis, simulation and experimental prototype. The single-stage converter provides a cheaper option to the two-stage converter. Further investigation is required in the control aspect to ensure stable converter operation and a maximized power factor over the voltage and power range. Additionally, the converter has a very different noise spectrum for both conducted and radiated electromagnetic interference compared to the two-stage charger and significant investigation is required to explore this aspect of the single-stage approach.